This is to certify that the

dissertation entitled

"Finite Size Effects and Coupling
in
Metallic Spin-Glasses"

presented by

Lilian M. Hoines

has been accepted towards fulfillment
of the requirements for

Ph.D. degree in Physics

Major professor

Date December 5, 1994

FINITE SIZE EFFECTS AND COUPLING IN METALLIC SPIN-GLASSES

By

Lilian M. Hoines

A DISSERTATION

Submitted to
Michigan State University
in partial fulfillment of the requirements
for the degree of

DOCTOR OF PHILOSOPHY

Department of Physics and Astronomy

1994

ABSTRACT

FINITE SIZE EFFECTS AND COUPLING IN METALLIC SPIN-GLASSES

By

Lilian M. Hoines

The quasi-static spin freezing temperature (T_f) has been measured as a function of thickness for magnetically isolated layers of the spin-glasses (SGs) $Cu_{1-X}Mn_X$ where X=0.10, 0.11, 0.12, $CuMn_{0.04}Au_{0.01}$, $Ag_{0.91}Mn_{0.09}$, $Au_{0.97}Fe_{0.03}$, and $Ni_{1-X}Mn_X$ where X=0.29 and 0.31, in SG/non-SG multilayered systems. For CuMn/IL where IL = Cu, Ag, or Au, T_f remains non-zero at spin-glass layer thickness (W_{SG}) of 1 monolayer. For W_{SG} ≥ 2 nm, the observed decreases in T_f with decreasing W_{SG} can be fit to the generalized scaling law $\left[T_f(W_{SG}) - T_f^{\,b}\right] / T_f^{\,b} \sim W_{SG}^{-1/\nu}$ with ν = 1.6. This expression is, however, incapable of describing data below W_{SG} = 2 nm. The data in the range 2 > W_{SG} > 0.21 nm show power law behavior that can be fit to the Fisher-Huse Droplet Excitation model $T_f / T_f^{\,b} \sim W^a$, with a = 0.8±0.1. AgMn is found to give similar finite size effects to those in CuMn, to within experimental uncertainties.

CuMnAu and AuFe, SGs with higher anisotropies, and NiMn, a SG with different magnetic interactions than CuMn, were studied to address theoretical predictions that the lower critical dimension is affected by anisotropy and interaction type. Within experimental uncertainty, the finite size effect behavior of T_f for all three was similar to that observed for CuMn, suggesting that neither anisotropy nor this change in interactions play major roles in depressing T_f. The NiMn system, however, did contain additional uncertainties as discussed in the text.

Systems of CuMn/IL where IL is not a noble metal, ILs = Al, Mo, V, and Si, and AgMn and AuFe with Si, all showed faster decreases in T_f with decreasing W_{SG} than those found for the noble metal ILs. This behavior could be attributed largely to mixing at the interfaces.

The unusually long range coupling of CuMn through Cu and Ag ILs (out to $W_{IL} \sim$ 20-30 nm) seen in previous studies was also approximately found for Au and CuGe ILs. Since Au is a strong spin-orbit scatterer, and CuGe has high resistivity, it is concluded that these two effects do not strongly affect the coupling length. All other materials tested- Al, Mo, V, Nb, and Si gave much shorter coupling lengths of ~ 2-5 nm, indicating that the long coupling length is dictated by the electronic structure of the IL.

ACKNOWLEDGMENTS

I would like to thank Dr. Jack Bass for his support and guidance during my time at Michigan State University.

I would also like to thank Dr. Jerry Cowen for helpful discussions and lending me some of his intuitive understanding.

There were many others at MSU who provided me with experimental assistance, helpful discussions, or moral support. Special thanks go to Reza Loloee, Mike Wilson, Vivion Shull, Dave Howell, Dr. Carl Foiles, Dr. Tom Kaplan, and all my friends and family.

Finally I would like to thank the Center for Fundamental Materials Research and the National Science Foundation for their financial support of this project.

TABLE OF CONTENTS

LIST OF TABLES

LIST OF ILLUSTRATIONS

CHAPTER 1

INTRODUCTION

1.1 Historical Perspective

The study of spin-glasses formally begins in 1971, when Cannella and Mydosh[1] discovered a cusp in the low field, a.c. susceptibility versus temperature of the random metal alloy AuFe. Although this alloy had been studied for decades before the cusp discovery, the previous measurements were done in large magnetic field, and a field on the order of few hundred G transforms the cusp into a broad rounded maximum. The discovery of such a sharp feature, normally the result of collective phenomena in ordinary phase transitions, raised the question of a potentially new type of phase transition in these materials. Above the cusp, the material behaves as a paramagnet. Below the cusp, a new state lacking the kind of long range order found in ferromagnets and antiferromagnets, the spin-glass (SG) state, occurs. The spin-glass (SG) state has its own distinct properties of remanence[2], relaxation[3], and hysteresis.[4,5] The SG spins are randomly spaced, appear to be "frozen" in disordered directions, and exhibit slow relaxations characteristic of "glassy" systems.[3] The term spin-glass (SG) results from the similarities between SG and glass properties, based upon disorder in both.

The nature of the transition to the SG state has since been the subject of much study and debate. If there is a phase transition, a transition temperature (T_f, for spin freezing temperature) would naturally be located at the susceptibility cusp. The peak is less dramatic than its ferromagnetic transition signature counterpart (the rise to demagnetization cut-off in ferromagnets is several orders of magnitude larger than the SG cusp), but the SG cusp height is comparable to those found for antiferromagnetic material.

Other experimental evidence suggested that the transition was not a true cooperative phase transition. SGs lack anomalies at T_f in the specific heat and resistivity[6] that are normally expected for a phase transition. The specific heat displays only a broad peak located ~20% higher than T_f. In time, a detailed investigation of the cusp itself was possible. Through very fine susceptibility measurement, the cusp proved to be progressively more rounded as the measuring frequency increased.[1,7] More importantly, the location of this rounded peak increased slightly in temperature as the frequency increased, about 1% for 2.5 decades (see Figure 1.1). The rounding and shifting of the peak is a result of the relaxations in the SG state, and supported an increasingly popular idea that susceptibility peak could be simply a nonequilibrium dynamic phenomenon rather than a phase transition.

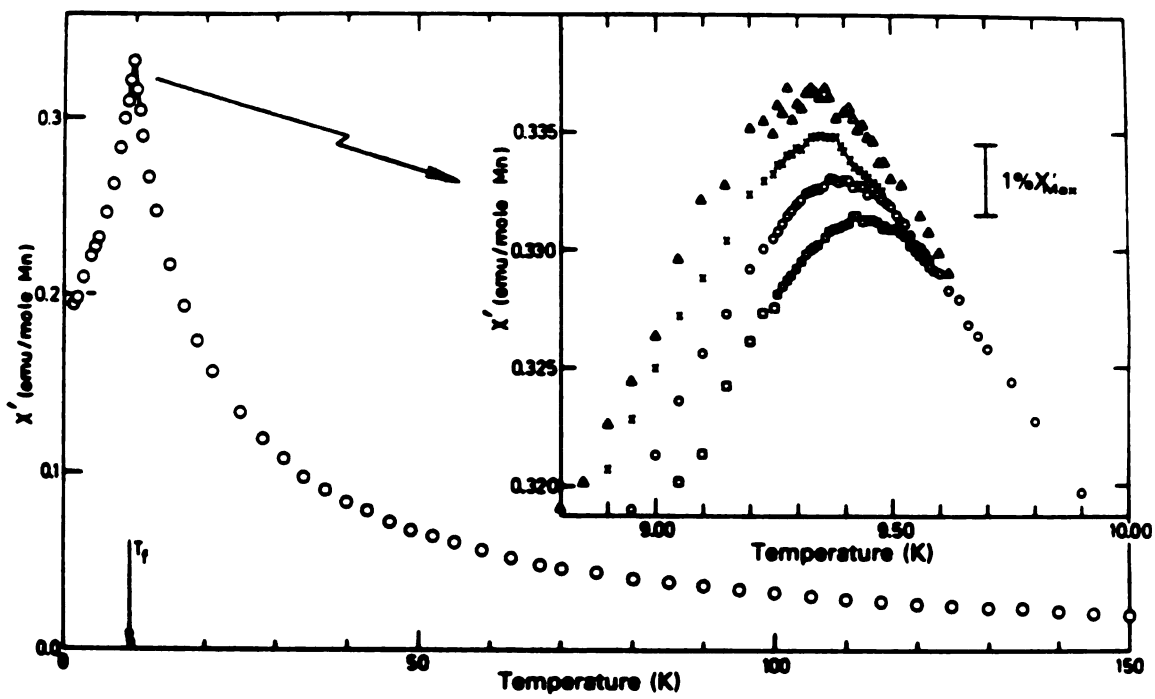

Figure 1.1 Frequency dependent a.c. susceptibility for CuMn, from Mulder et. al..[7]

Theoretical approaches likewise could not give concrete answers to the phase transition controversy. Much of the theoretical work has been aimed at finding a mean field theory for SGs similar to that which was so successful in explaining ferromagnetism. Mean field theory in ferromagnetism, when the interactions are infinite ranged, leads to good agreement with experiments, so Sherrington and Kirkpatrick considered a similar case for SGs.[8] The SG mean field calculations gave a paradoxical result of negative entropy due to unstable solutions for $T < T_f$. After years of theoretical effort, what is now believed to be the correct solution to the Sherrington-Kirkpatrick model was found by Parisi.[9] The complexity of this result however left its physical meaning obscure. Direct approaches such as Monte Carlo methods suffered from problems due to the long relaxation times, yielding theoretical results that were ambiguous on the phase transition question.

General consensus at the present time is in favor of a phase transition, motivated by, among other things, the experimental discovery of an apparent divergence in the nonlinear part of the susceptibility vs. temperature.[10,11]

Up until the mid 1970's, most of the effort in condensed matter research focused on ordered systems, many properties of which are now reasonably well understood. The fact that real systems in nature, and common materials such as glass and polymers, contain disorder, eventually led to an increase in the study of frustrated and disordered systems, including SGs. In spite of their theoretical complexity,[3] SGs may still be considered simple for random systems, and so the study of them can contribute greatly to the understanding of the physics of disorder. Attempts to solve the SG riddle theoretically, have thus far produced valuable statistical mechanical insights, as well as statistical mechanical methods that are usefully applied to other complex problems. For example, similarities between the SG and combinatorial optimization problems[12] led to *simulated annealing*[13], an analysis method proven useful in several applications in large scale

electronic circuit design. In addition, neural network modeling has been helped by a model proposed by Hopfield that recognizes learned patterns in the brain as random cooperative phenomena[14], which require similar mathematical treatment to that developed in SG theory.

1.2 Experimental Signatures

According to Binder and Young[3], a spin-glass should possess the following qualities: (i) a frequency dependent peak in the susceptibility, caused by "frozen" magnetic moments at $T<T_f$; (ii) lack of periodic long range magnetic order; (iii) remanence and magnetic relaxation on macroscopic time scales at $T<T_f$ when the magnetic field is changed. The definition of "frozen" is of course dependent on the observation time, because the system is relaxing, leading to frequency dependence as shown in Figure 1.1 . Some systems contain both ferromagnetic and SG order in a mixed phase, and so may contain some degree of long range order. These are the reentrant SGs (RSGs), and will be discussed later.

Characteristic (i) is easily observed in a magnetic susceptibility scan with the application of a small oscillating measuring field. Condition (ii) is verified through the lack of the sharp neutron scattering peaks that identify long range ferromagnetism and antiferromagnetism.[15,16]

Criteria (iii) manifests itself in several ways. Thermoremanent magnetization (TRM) may be observed by field cooling (FC) the SG from $T > T_f$ to a point $T < T_f$, and then removing the field.[17] Isothermoremanent magnetization (IRM) is seen by cooling the system in zero field (ZFC), and then applying a field for a short time and removing it. In both cases the system will relax[18], showing behavior dependent on the sample magnetic

history. The strong time dependence in the ZFC state indicates that it is not an equilibrium state, while the weak time dependence of the FC state suggests equilibrium.[18] Other experimental methods may probe the relaxation of the spins using different characteristic time scales, such as neutron echo (10^{-12} s < t < 10^{-8} s),[19] electron spin resonance (10^{-9} s < t < 10^{-8} s),[20] and muon spin resonance (t < 10^{-5} s).[21] These experiments reveal rapidly increasing relaxation times near the critical temperature. Such data have been fit to both to $ln(t)$[21] (gradual, glass like freezing) and an algebraic form[22] $t^{-\zeta}$ (phase transition).

Changing the field at fixed temperatures below T_f gives rise to a hysteresis effect, a pronounced irreversibility such as that found in ferromagnets. The shapes of SG hysteresis loops are highly dependent on magnetic history and sample anisotropy (see Section 1.4.3). Figure 1.2 shows the hysteresis of the SG $Cu_{0.75}Mn_{0.25}$ when cooled from above T_f to below T_f in zero and in an applied field.[23] The horizontal shift of the FC loop is a usually attributed to the Dyzaloshinski-Moriya uniaxial anisotropies discussed in Section 1.4.3. Figure 1.3 shows the hysteresis of the SG $Au_{0.92}Fe_{0.08}$ when cooled in field.[24] The AuFe loop is broad and symmetric, unlike the field cooled CuMn loop. This feature is usually interpreted as resulting from a stabilization of anisotropy in magnetic microdomains,[24] although some controversy exists.[25]

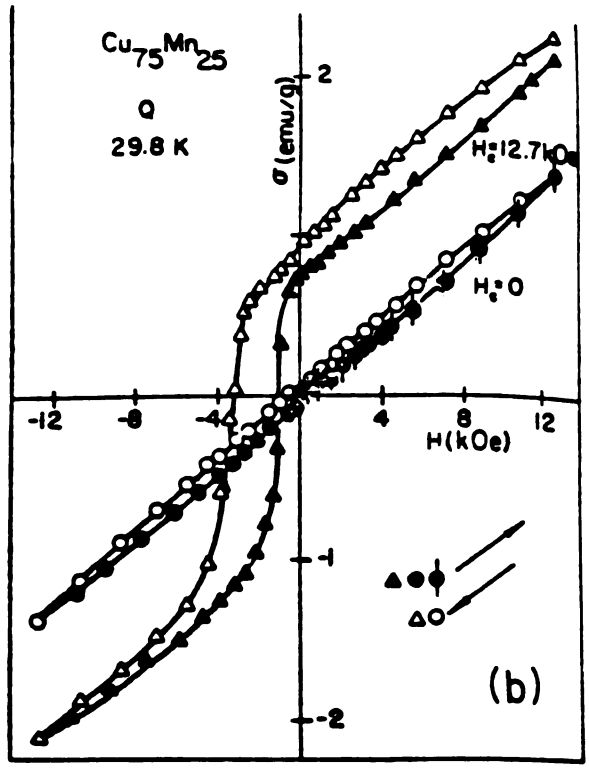

Figure 1.2 Hysteresis behavior of $Cu_{0.75}Mn_{0.25}$ cooled from $T > T_f$ to $T < T_f$ in zero field ($H_c = 0$) and in an applied field ($H_c = 12.7$kG) from Beck.[24]

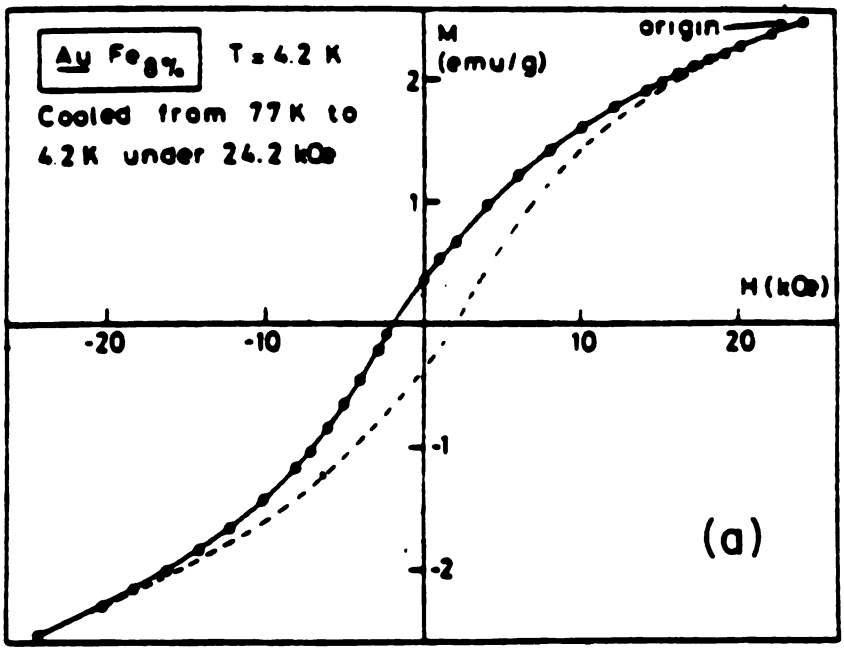

Figure 1.3 Hysteresis behavior of $Au_{0.92}Fe_{0.08}$ cooled from $T>T_f$ to $T<T_f$ in field from Prejean.[25]

Probably the most readily recognized SG signature also stems from relaxation and remanence. A static magnetization vs. T scan will reveal a peak in the ZFC curve and exhibit the difference between FC and ZFC behavior. Two scans are taken, one where the sample is cooled to below T_f in the small measuring field, and another where the sample is ZFC and then the measuring field is applied. The two curves join each other in the vicinity of the ZFC peak, but below the peak irreversibility occurs. In the present study, the location of the ZFC curve maximum (see Figure 1.4) is defined as T_f.

1.3 T_f is not T_c - Relaxation

T_c is the temperature where a true phase transition occurs for a system at equilibrium. The time taken to reach equilibrium, the maximum relaxation time (τ), increases as the temperature decreases towards T_c. In a SG, at some temperature τ becomes longer than the finite measuring time, τ_m. This is the temperature recorded as T_f. Below T_f the system is no longer in equilibrium, and appears to "freeze" into the SG state. T_f therefore should be observed at a temperature *higher* than T_c, and T_c may be determined only by extrapolation of the measuring time $\tau_m \rightarrow \infty$. The T_fs reported in this and other studies using ZFC magnetization measurements to determine T_f are referred to as "quasi-static" freezing temperatures. The measuring time for each data point is relatively long, on the order of several minutes per point.

In order to extrapolate to the true T_c, dynamical experiments must be performed. Figure 1.5 shows data from Sandlund et. al.,[26] of FC curves for a bulk sputtered film (1000 nm thick) of $Cu_{0.86}Mn_{0.14}$. The ZFC curves show the shift of the ZFC peak as a

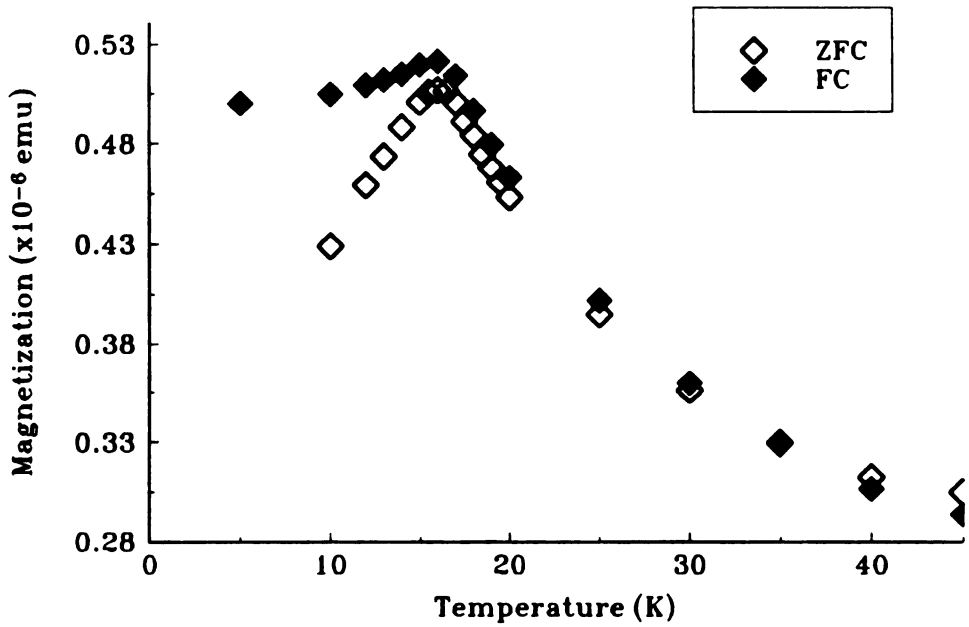

Figure 1.4 Static magnetization curve for a 500 nm thick (bulk) film of $Au_{0.97}Fe_{0.03}$.

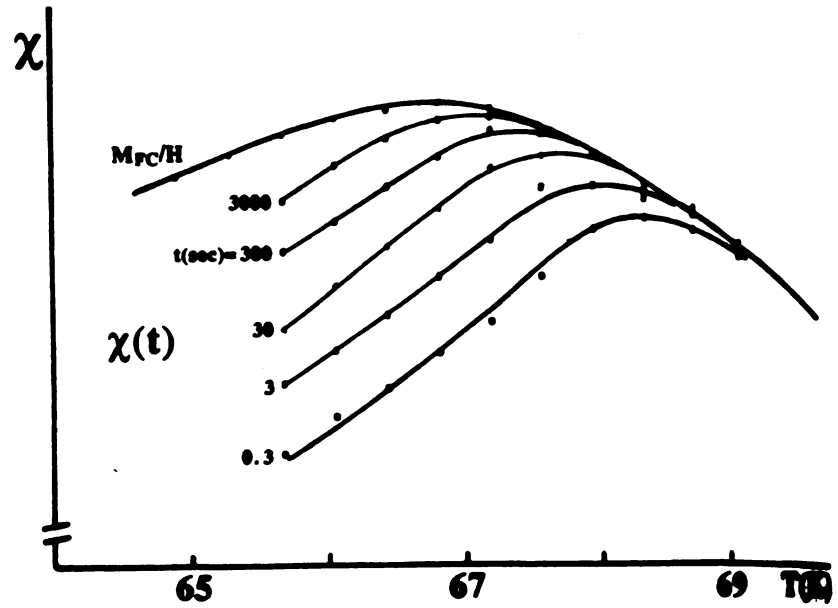

Figure 1.5 ZFC susceptibility at different measuring times for a 1000 nm (bulk) film of $Cu_{0.86}Mn_{0.14}$. From Sandlund et. al..

function of measuring time. Conventional critical slowing down predicts that τ should diverge when approaching T_C, according to the power law[3]

$$\tau/\tau_o \sim \left(T - T_c/T_c\right)^{-z\nu}.$$

Here τ_0 is a microscopic relaxation time, and z and ν are critical exponents, defined later in Section 1.6.3. Since T_f is defined as the temperature where the measuring time and relaxation time are equal, this expression may be written as[26]

$$\tau_m/\tau_o \sim \left[(T_f - T_c)/T_c\right]^{-z\nu}. \qquad \text{Equation 1.1}$$

Equation 1.1 was successfully applied to Figure 1.5, where T_f is measured as the peak in each curve, giving $T_C = 66 \pm 0.2$ K, and $z\nu = 9 \pm 1$, using $\log_{10}\tau_0 = -13 \pm 1$ (where τ_0 is in seconds).[26] The $z\nu$ and τ_0 values are reasonable for a 3D system of this type.[27] The CuMn sample had a quasi-static $T_f = 67 \pm 1$ K, indicating that the value of T_C is not significantly smaller than the quasi-static T_f value.

1.4 Spin-Glass Concepts

1.4.1 Disorder and Frustration

The two conditions necessary to obtain SG behavior are believed to be *disorder* and *frustration.*[3] Frustration, following the definition of Sherrington,[28] is the inability to simultaneously satisfy all local ordering requirements as dictated by energy considerations. Both real SG systems and theoretical SG models must contain these two elements to exhibit the necessary properties to be classified a SG. Many examples exist that contain

either randomness or frustration. A one dimensional (1D) Ising spin system with random nearest neighbor interactions, ±J,

↑ + ↑ - ↓ - ↑ - ↓ + ↓

results in a disordered array of spins but no frustration. A triangular antiferromagnet (for simplicity consider Ising spins),

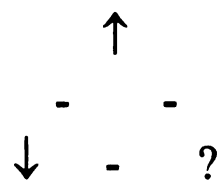

although contains no disorder will always be frustrated (the third spin cannot simultaneously point up and down). Neither of these systems are considered suitable SGs.[29]

Frustration plus disorder state in SG is created in two primary ways:

a) Randomly spaced elements coupled through an interaction that oscillates between ferromagnetic and antiferromagnetic with distance. The competing ferromagnetic and antiferromagnetic interactions create the frustration. This is the situation in transition metal/noble metal alloys (e.g. CuMn), where the dilute, randomly mixed transition metals interact primarily via the long range oscillatory RKKY interaction. The SG state of amorphous $Al_{0.63}Gd_{0.37}$ arises from the same circumstance, but the random spatial placement of atoms is provided by an amorphous structure. Other interactions may spawn the same result, as in $Eu_xSr_{1-x}S$, where the randomly placed magnetic Eu atoms interact ferromagnetically for nearest neighbors and antiferromagnetically for next nearest neighbors.[30]

b) Addition of bond disorder. This situation often occurs in the reentrant SGs (RSGs), systems that undergo a paramagnetic to ferromagnetic (FM) transition, then FM to a SG-like state transition as the temperature is reduced. One way to form a reentrant SG is to dilute one magnetic species, such as ferromagnetic (FM) nickel, with another, such as antiferromagnetic (AF) Mn. The Ni-Mn interaction is FM, so initially as Mn is added randomly the system remains FM. At some critical Mn concentration, enough AF bonds from Mn-Mn neighbors have been added to create sufficient disorder to form a SG-like state at low temperatures.[32] Further addition of Mn leads to a more typical SG regime, with a single paramagnetic to SG transition.[33,34] Such a reentrant phase is predicted theoretically,[9,35] giving a magnetic phase diagram like Figure 1.6.

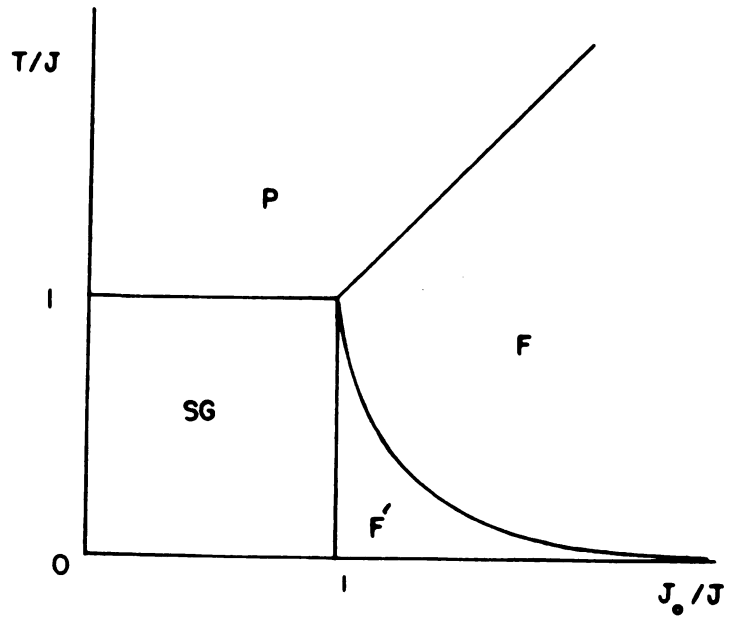

Figure 1.6 Phase diagram showing reentrant transition (diagram copied from reference 3).

1.4.2 Magnetic Interactions

As stated above, SGs result from primarily one of two types of interactions - long range oscillatory interactions, or a combination of FM and AF short range interactions. The prototypical SGs, CuMn, AgMn, AuFe, etc. are of the first variety, containing transition metal ions randomly distributed in a non-magnetic host. The magnetic impurities interact via the coupling of the moment with the conduction electrons in the host. The dominant interaction is commonly accepted to be the RKKY interaction. Ruderman and Kittel originally derived this interaction to describe the coupling of nuclear moments through the hyperfine interaction.[35] Kasuya[36] and Yosida[37] later contributed an explanation of how localized d electrons in transition metals scatter conduction electrons. The result is an interaction with an unwieldy name, the Ruderman Kittel Kasuya Yosida (RKKY) interaction:

$$\mathcal{H} = \sum_{i,j} J_{ij} \vec{S}_i \cdot \vec{S}_j$$

$$J(R_{ij}) = \frac{{\mu_B}^2 m}{(2\pi)^3 \hbar^2} \left[\frac{2k_F R_{ij} \cos(2k_F R_{ij}) - \sin(2k_F R_{ij})}{{R_{ij}}^4} \right].$$

Here R_{ij} is the distance between spins S_i and Sj, k_F is the Fermi number of the host, and m is the mass of a conduction electron.

At very short distances, $2k_F R \ll 1$, the numerator may be expanded for $x \equiv 2k_F R$

$$\sin x - x\cos x \sim x - \tfrac{1}{6}x^3 + \ldots \sim \tfrac{1}{3}x^3 \sim \tfrac{8}{3}k_F R^3$$

so the interaction has the form:

$$J(R_{ij}) \sim 1/R_{ij}.$$

This expression diverges at the origin, which does not affect the energy of the interaction of the two moments, and causes only an apparent divergence in the self energy of a moment, which itself is small.[38]

For long distances, $2k_FR >> 1$, the term $2k_F cos(2k_F R)$ dominates, leaving an oscillatory interaction that decays as $1/R^3$. The classical SGs (noble metal plus transition metal impurities) may be considered in this interaction range, since k_F is on the order of 2 $Å^{-1}$, and R is on the order of 2 - 20 Å, depending on the impurity concentration. The $1/R^3$ envelope leads to a prediction of an approximately linear dependence of T_f on the moment concentration, c,[39] which is not observed in the classical SGs.[40,41] Instead, the relationship is sublinear (for CuMn, $T_f \sim c^{0.7}$), a behavior not yet completely understood .

The sublinearity of T_f has been attributed to mean free path (mfp) effects.[42] Vier and Schultz[40] mixed nonmagnetic impurities In, Sn, and Sb, into the SGs CuMn and AgMn to decrease the mean free path and observe the effect on T_f. They reported that as mfp effects are removed from CuMn, T_f tends towards, but does not reach, a linear dependence on Mn concentration. Also, for CuMn and AgMn with constant Mn concentration, the T_f depression resulting from reducing the mfp levels off as the mfp continues to decrease, giving a value for $T_f(mfp \rightarrow 0)$ of half $T_f(mfp \rightarrow \infty)$ through extrapolation. This suggested to Vier and Schultz that a significant part of the interaction contributing to T_f must be mfp independent. Larsen[43] was able to explain both the T_f vs. Mn concentration nonlinearity and the T_f depression saturation, through a calculation using the original RKKY damping function of deGennes.[44] Here the RKKY interaction is damped by an exponential decay, $e^{R/\lambda}$, representing the finite lifetime of the conduction electrons with mfp λ. Later, Jagannathan et. al.[45] reported that Larsen's method contained an improper phase average, and through an alternate calculation were able to show that the mfp had little effect on the strength of the RKKY interaction. This result agreed with

earlier conclusions from unsuccessful attempts to fit experimental results to the exponential form.[46]

Soon after, Zhang and Levy[47] recalculated the interaction between transition metal impurities in a non magnetic host, claiming that the point contact interaction for the spin scattering used in the RKKY derivation was inappropriate. Zhang and Levy assert that the s-d orbital mixing is the primary source of spin coupling of Mn in Cu, and so the associated energy and angular dependence must be taken into account from the onset. The result was the identification of two regimes regarding the interaction strength envelope: the preasymptotic region, where $R < \sim 3$ nm, and the asymptotic region, where $R > \sim 3$ nm. The interaction in asymptotic region differed from the RKKY interaction only by a constant, retaining the oscillatory nature and the $1/R^3$ envelope. The interaction in the preasymptotic region, however, was found to decay more slowly, as $1/R^2$. Zhang and Levy were then able to make mfp effect corrections to the preasymptotic region for CuMn and AgMn, and argued that the preasymptotic effects were the major source of the sublinear dependence of T_f on Mn concentration.

Short range interactions are normally thought to cause SG behavior in insulators or semiconductors. Here the interaction occurs via superexchange, where a ligand or anion between two magnetic atoms transfers an electron between them. The resulting orbital mixing may create a ferromagnetic or antiferromagnetic bond between the two moments. SG alloys composed entirely of magnetic atoms, such as NiMn (one of the materials studied in this thesis), can also be dominated by short range interactions. Many of the early behaviors seen in NiMn, such as the concentration dependent magnetization, were explained through a nearest-neighbor molecular-field model with FM Ni-Ni and Ni-Mn interactions and AF Mn-Mn interactions.[48] The strong dependence of the Mn moment direction upon the nearest neighbor environment, and the competing AF and FM bonds, were later confirmed through neutron diffraction work.[49]

1.4.3 Anisotropy

Other interactions present in a SG, which can be important to its primary features (such as existence and location of T_f, degree of remanence, etc.), are the *anisotropic interactions*. Whereas the interactions discussed above are purely isotropic, independent of the direction of a given spin, anisotropic interactions are crucially linked to some particular direction, such as an easy axis in the crystal lattice or along an external field. Anisotropy adds additional energy requirements for the spin to fulfill, thus increasing the frustration. The Hamiltonian for a SG thus consists of two parts:

$$\mathcal{H} = \mathcal{H}_{iso} + \mathcal{H}_{anis}$$

where

$$\mathcal{H}_{iso} = \frac{1}{2}\sum_{i,j} J_{ij}\vec{S}_i \cdot \vec{S}_j$$

Two types of anisotropy are always present in a SG, dipolar and Dyzaloshinski-Moriya. The dipolar interaction is the classical interaction of two dipoles, giving[3]

$$H_{dip} \sim \sum_{i \neq j}\left[\vec{S}_i \cdot \vec{S}_j - 3(\vec{S}_i \cdot \vec{R}_{ij})(\vec{S}_j \cdot \vec{R}_{ij}) / R_{ij}^{\,2}\right] / R_{ij}^{\,3}.$$

This term is normally very small for point dipoles. If the moment contains an orbital character, however, as does Fe in Au, then this dipolar anisotropy can become much larger.

The other expected anisotropy, introduced by Dzyaloshinski[50] and Moriya[51], results from the spin-orbit scattering of metal conduction electrons off a third atom. The third atom may be another impurity of the same type, or an additional impurity, magnetic or nonmagnetic. The Hamiltonian for a SG with spin-orbit anisotropic interactions of strength D is[52]

$$H_{DM} = \frac{1}{2}\sum_{i,j} \vec{D}_{ij} \cdot \vec{S}_i \times \vec{S}_j$$

Taking the root mean squares of the configuration averages of J_{ij} in the isotropic part and D_{ij} in the anisotropic part, the mean field approximation gives[53]

$$T_f \sim \sqrt{J^2 + 2D^2},$$

meaning T_f is expected to increase as anisotropic interactions increase. Experimental[24,40,54,55] and theoretical[52,56] evidence strongly suggest that this mechanism is particularly important if the third impurity is a strong spin-orbit coupler, such as Au, Pd, Co, Fe, or Pt.

Neither of the above anisotropies are global; they do not select a single preferred direction for all spins. They do, however, add additional interactions, increase frustration, and stabilize spin configurations.

Anisotropy strength is represented in this thesis by the *anisotropy field*, H_A, the field that holds the remanent magnetization in place. H_A is defined by[57]

$$H_A = 2K/\sigma,$$

where σ is the remanent magnetization and K is the anisotropy constant. H_A may be measured directly by transverse susceptibility[57]

$$\chi_\perp = \sigma(H_A + H_0)^{-1},$$

where H_0 is an external field, or from a shift in the electron spin resonance frequency, ω[55]

$$\omega \sim (H_A + H_0).$$

Hysteresis measurements, which determine the field of magnetization reversal, H_r, allow H_A determination indirectly from the relation[24]

$$K = \frac{1}{4}\sigma H_r.$$

1.4.4 Short Range Order and Spin Density Waves (CuMn and AgMn)

Randomizing a metal alloy experimentally can be a considerable challenge. Even two mutually soluble materials may cluster, or develop short range order, when alloying. One commonly used method for producing random SG samples involves annealing at high temperature and then quenching to freeze in the thermally induced disorder. Other methods include evaporation and sputtering, where the atoms are randomized during their flight towards a substrate. Substrate cooling is often used to aid the freezing of the atoms in their random positions.

Ordering in the SG sample will often manifest itself in detectable magnetic signatures of ferromagnetism or antiferromagnetism. Neutron studies on CuMn with Mn concentrations of 5 - 25 at.% Mn have revealed ferromagnetic domains containing 20 to 50 atoms even for well annealed samples,[16], indicating a preference for Mn at the next nearest neighbor position. X-ray studies on AgMn with 1.4 - 24 at.% Mn also show Mn n.n.n. preferential ordering.[58] AuFe is known to almost unavoidably form Fe clusters (nearest neighbor) when the Fe concentration exceeds ~ 12 at.%,[59] and NiMn has a strong tendency to form the ferromagnetic compound Ni_3Mn for Ni rich compositions.[60] It is suspected that no SGs experimentally studied are completely random, that all contain at least some small amount of local ordering. In some cases, increasing ordering can lead to a change in properties.

Another type of ordering shared by CuMn and AgMn in the SG state is apparent spin density wave (SDW) formation[61,62] A SDW is a incommensurate wave of helical conduction electron spin directions. It was introduced by Overhauser in 1960 as a proposed ground state of the free electron gas.[63] The theory neglects correlations which are present in real metals, and as a result SDW are seldom the ground state in pure metals. There are a few exceptions, such as Y and Cr, where the shape of the Fermi surface encourages long range SDW formation. Alloys with spin impurities can potentially exhibit a SDW ground state, if the energy from the interactions of the extra stationary spins as

they line up with a SDW is enough to compensate for the higher energy needed for SDW formation. It appears that CuMn and AgMn are able to support finite correlation length SDWs through this process. Careful studies of broad, weak neutron scattering peaks suggest the presence of a helical SDW in CuMn ~ 4 nm in length, containing about 4000 atoms.[61] A SDW modulation may be perturbed by the underlying regions of ferromagnetic order discussed above without losing its coherence. The role of these short SDWs in the SG state, if any, is unclear.

1.5 The Lower Critical Dimension (d_l)

The lower critical dimension, d_l, is the dimension below which a system can no longer support a phase transition. If the value of d_l is above 3, $T_c = 0$ in the real 3D system; if it is below 2, T_c will be finite in a film of "zero" thickness. One of the main foci of finite size effect studies is how T_c changes as a film is thinned towards the 2D limit, which should be affected by the value of d_l.

Efforts to calculate d_l for SGs have proved somewhat unsatisfactory.[3] High temperature series expansions, which usually work well for systems without quenched disorder, gave for 3D Ising SGs $d_l > 4$.[64] This value was widely believed until the early 1980's when some serious problems were noticed with the calculation.[65,3] Exact partition function calculations allow direct estimates of static quantities, but are restricted to small samples. As a result they are mainly appropriate for the 2D lattice, giving $d_l > 2$.[66]

One fruitful method for determining d_l comes from Monte Carlo simulations. Ising SGs with short range interactions are found to have $d_l < 3$.[67] Heisenberg short range SGs with no anisotropy are found to have $d_l > 3$, but adding anisotropy drops d_l below 3.[68] Heisenberg SGs with long range, RKKY type interactions are found to have $d_l \sim 3$,

and to be in a different universality class than their short range Heisenberg counterparts.[69,70] These simulations suggest that two things are affecting d_l, the type of interactions and the degree of anisotropy.

1.6 Finite Size Effects in Spin-Glasses

A true thermodynamic phase transition occurs only in the thermodynamic limit of infinite volume and number of particles. Real systems are not infinite, but macroscopic systems are large enough to produce close agreement with theory. If a system is significantly reduced in size, the behavior near the singularity begins to deviate from the thermodynamic prediction. A thin film may be considered as infinite in two dimensions and finite in the third. Films of ordered systems, such as ordered ferromagnets and antiferromagnets, do not show finite size effects until the film thickness reaches a few monolayers,[71] limiting the range of study and making experiments in general rather difficult.

Interest during the early 1980's in d_l[72] and finite size scaling for SGs[73] set the stage for a finite size effect study in SGs. Theoretical and experimental evidence on 3D and 2D RKKY-like SGs suggested that the lower critical dimension (d_l) lies between 2 and 3 (see Section 1.5). Thin SG films would simultaneously provide an opportunity to explore finite size effects on a disordered magnetic system, and allow study of behavior across a lower critical dimension boundary. Unfortunately the magnetic signal of a single film SG thin enough to show a significant finite size effect is comparable to the sensitivity of modern commercial susceptometers. The solution is to make many layers of the same thickness and decouple them magnetically; i.e. to make a multilayer. The technology to fabricate multilayers of high enough quality has emerged only in the last decade or so, with the advent of ultra high vacuum sputtering and evaporation techniques.

1.6.1 Static Measurements of Linear Magnetization

Motivated by the possibilities just described, in the mid 1980s the Michigan State group with Kenning et. al. undertook such studies using sputtered multilayers containing $Cu_{0.93}Mn_{0.07}$ and found the first evidence of finite size effects in a long-range, RKKY type SG. Observable decreases were found in the quasi-static T_f as the SG layers were thinned, with the decreases starting at SG thickness (W_{SG}) ~ 50 nm. W_{SG} ranged from 500 nm to 4 nm, and magnetic decoupling for the spin-glass layers was achieved via thick interlayers (ILs) of amorphous Si.[74] Later, the Mn concentration in the SG was varied and the experiment repeated for $2\ nm \leq W_{SG} \leq 1000\ nm$.[75] Three concentrations of 4, 7, and 14 at.% produced T_f values for bulk samples (T_f^b) of 23 K, 34 K, and 62 K respectively. When the T_fs for the thin SG layers were normalized by the appropriate value of T_f^b for each concentration, a nearly universal behavior was found; curves for all three concentrations collapsed almost onto one another (see Figure 1.7).

To check effects of conducting vs. insulating ILs, similar studies were also done using Cu as the IL.[76] The results were qualitatively similar to the study with Si, but the "universal" curve for the CuMn/Cu decreased more slowly with decreasing W_{SG} than that for CuMn/Si. The authors postulated that this difference was primarily due to contamination of the CuMn from diffusion of Si into the CuMn grain boundaries. Presuming that most of this diffusion occurs during sample growth, the growth temperature was lowed from ~ 90°C to below room temperature in an attempt to slow the diffusion. The result was a satisfying shift of the CuMn/Si curve towards the CuMn/Cu curve,[76] with the CuMn/Cu curve unaffected by the growth temperature change.

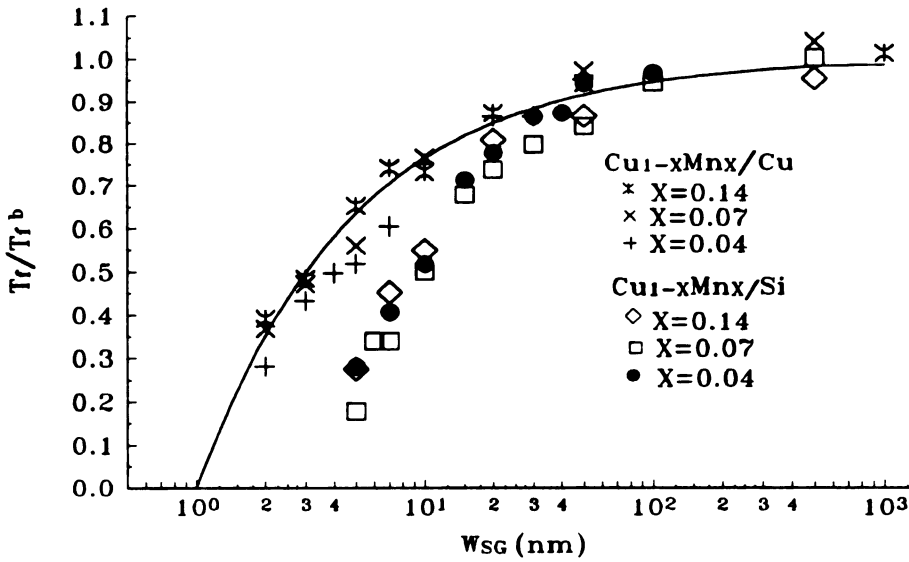

Figure 1.7 Universal curves for CuMn/Cu and CuMn/Si. From Kenning et. al. The solid line represents the generalized scaling law with $\nu = 1.6$ and W_c=1 nm.

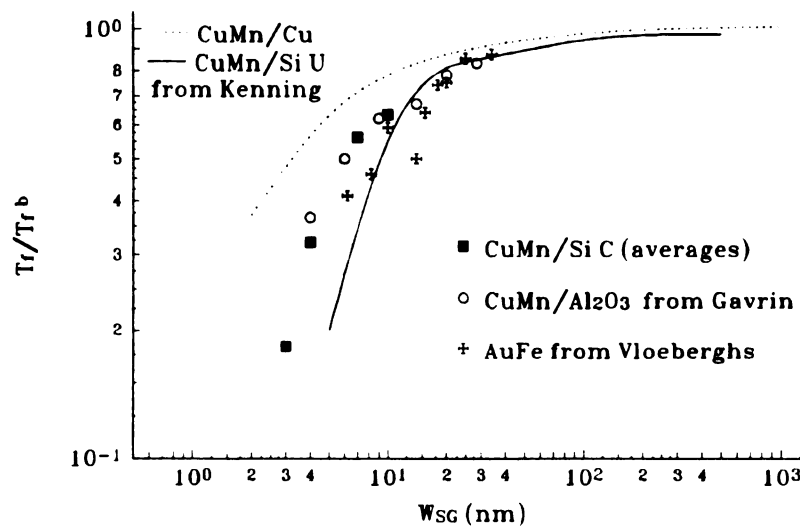

Figure 1.8 Finite size effect curves for CuMn with cooled (C) and uncooled (U) Si ILs from Kenning, Al_2O_3 ILs from Gavrin et. al. and AuFe SG from Vloeberghs et. al.

1.6.2 Static Scaling of Linear Magnetization

1.6.2.1 General Finite Size Scaling

The first attempts of Kenning et. al. to fit the data in Figure 1.7 to theory utilized the only scaling law available at the time, a general scaling law adapted for thin films. The thin film may be considered infinite in two dimensions and finite in the third, the width of the film, W. As W is reduced, the bulk critical temperature, T_c^b, shifts to a new value, $T_c(W)$, according to

$$\frac{T_c(W) - T_c^b}{T_c^b} \sim AW^{-\lambda} \qquad \text{Equation 1.2}$$

where λ is defined as the shift exponent,[77] with the relation $\lambda = 1/\nu$, where ν is the correlation length exponent. This scaling law, discussed in more detail in Chapter 2, is derived via a perturbative method and so is only expected to be valid where $T_c(W) \sim T_c^b$. The value of ν found from nonlinear susceptibility measurements is $\nu \sim 1.3 \pm 0.2$ or $0.77 \geq \lambda \geq 0.91$ for AgMn [11] and $\lambda = 0.62$ for CuMn.[78]

Replacing $T_c(W)$ by T_f, using T_f^b for T_c^b, and allowing both λ and A to be free fitting parameters, the data for Si and Cu ILs could be fit to Equation 1.2 over the entire range of thicknesses, 2 nm $\leq W_{SG} \leq$ 1000 nm, with different values of λ and A for each IL. Fitting this way gave $\lambda = 0.70$ for Cu IL and $\lambda = 0.80$ for Si ILs. Both values are within the estimated uncertainties for λ from the AgMn nonlinear χ experiments, but somewhat larger than the CuMn λ (although the uncertainty is not given). The range of the fit is interesting, since much of the data (T_f(2 nm) $\sim 0.4T_f^b$) is not in the expected region of validity, $T_f \sim T_f^b$. Fitting the CuMn/Cu data only to thick $W_{SG} \geq 20$ nm, a different value of $\lambda = 0.91$, or $\nu = 1.1 \pm 0.3$,[79] was obtained. This is still in agreement

with the independently acquired value of ν above for AgMn, but is farther from the CuMn value.

If Equation 1.2 is considered in the region where $T_f << T_f^b$, the critical thickness where $T_f(W) = 0$ K corresponds to $W = W_c$, determined by

$$W_c = \left(\frac{-1}{A}\right)^{-\lambda}.$$

Using the exponent from the fit to the entire thickness range, the CuMn/Cu system gave values of $W_c \sim 1.0$ nm, and the CuMn/Si system had a larger critical thickness, $W_c \sim 3.6$ nm.[80] The larger W_c value for the CuMn/Si resulted from the faster dropping of the CuMn/Si curve, and so was attributed largely to the interface effect of Si diffusing into the CuMn layer.

To test whether these results were reproducible in other SGs, this same Michigan State group repeated the CuMn experiment using AgMn (Stubi et. al.[81]), a similar long range RKKY-type low anisotropy SG.[3] Two concentrations were tested, 4 and 9 at.% Mn, and two ILs were tested, Cu and Ag. The same SG thickness range as above was covered, 2 nm ≤ W_{SG} ≤ 1000 nm, with the addition of one $Ag_{0.91}Mn_{0.09}$/Cu data point at $W_{SG} = 1$ nm. The AgMn data for both concentrations reproduced the CuMn/Cu curve of Kenning et. al. within mutual uncertainties, independent of which metal IL was used.

Not long after the above CuMn studies of Kenning et. al., Gavrin et. al.[82] published results on sputtered multilayers of thin $Cu_{0.92}Mn_{0.08}$ ($T_f^b = 34$K) with Al_2O_3 ILs, with 4 nm ≤ W_{SG} ≤ 125 nm. These data were fit to the scaling Equation 1.2, giving an exponent of $\lambda = 0.64$ with a critical thickness $W_c = 1.95$ nm. Figure 1.8 shows that these T_f data normalized to their appropriate T_f^b fall close to the cold sputtered CuMn/Si data discussed above.

The three different values obtained for λ and W_c for three different IL materials exposed the need to better understand the role of the IL and boundary conditions on the finite size behavior. In the present thesis, samples containing several different IL materials are used to attack this problem.

1.6.2.2 Scaling for SGs - Droplet Excitation Model

The scaling theory used in all of the above cases was developed to fit data with $T_c \sim T_c^b$, not for providing information in the range of W_c, where $T_c \rightarrow 0K$. In response to the data of Kenning et. al., D.S. Fisher and D.A. Huse formulated a scaling model which included dimensionality and was extendible to the region where T_f is far below T_f^b.[83] This model, discussed in detail in Chapter 2, assumes that the low lying excitations in the SG state are droplets of coherently flipping spins. The lower critical dimension is assumed to be between 2 and 3, meaning $T_c = 0K$ for $d = 2$ ($W_{SG} = 0$).

For $T_f \sim T_f^b$, the theory predicts:

$$\frac{T_f^{\,b} - T_f(\tau)}{T_f^{\,b}} \propto W_{SG}^{-(1/\nu_3)} \left[ln\left(\frac{\tau}{W_{SG}^{\,z}} \right) \right]^{[(\psi_3 + \nu_2 \psi_2 \theta_2)\nu_3]^{-1}} \qquad \text{Equation 1.3}$$

The subscripts in the exponents denote the dimensionality, W_{SG} and τ are normalized by a microscopic length and time, and the exponents are defined in table 1.1. Equation 1.3 is the same as Equation 1.2, with the addition of a weak logarithmic factor in the measuring time, τ: At present, the difference between the Fisher-Huse logarithmically corrected equation and Equation 1.3 is beyond experimental resolution.

For $T_f << T_f^b$, the model predicts

$$\frac{T_f}{T_f^{\,b}} \sim W^a \quad , \qquad \text{Equation 1.4}$$

where a is a compilation of critical exponents (see Section 2.2). This model was applied to the CuMn data of Kenning et. al.[79] and Stubi et. al.[81] also applied this model to AgMn data. The CuMn/Cu data were fit to Equation 1.4 for 2 nm $\leq W_{SG} <$ 20 nm, obtaining an exponent of a = 0.5.[79] Since data in this region also fit the general scaling law of Equation 1.2, studies on thinner SG layers were needed to determine the validity of this model, as well as help determine whether T_f is finite at W_{SG} = 0 nm. The AgMn/Ag and AgMn/Cu were fit together to Equation 1.3 for 1 nm $\leq W_{SG} <$ 10 nm, obtaining an exponent of a = 0.65.[81] Since the AgMn and CuMn data lay along closely parallel curves, the values for a might have been the same were it not for the inclusion of slightly thinner W_{SG} data in the AgMn fits. This difference in a thus also suggests the need for more data in the thickness range $W_{SG} <$ 2.

When the project reported in this thesis was beginning, Vranken et. al.,[84] published results on single thin films of $Au_{0.95}Fe_{0.05}$ of 4 nm $\leq W_{SG} \leq$ 40 nm, flash evaporated onto a glass substrate and protected with an overlayer of SiO. AuFe is similar to CuMn, but generally believed to have much higher anisotropy,[85] (although some opinions differ[25]). As in CuMn, size effect depression in T_f of AuFe was observed. The AuFe data produced a shift exponent λ = 1.5, much larger than that found for the CuMn case. The T_f values also decreased faster with thinning than any of the above mentioned CuMn studies, leading to a larger W_c (see Figure 1.8). Although these data suggest that the AuFe SG might be different than CuMn, one must be careful in the comparison since the flash evaporation process used to produce the AuFe single films is quite different from sputtering. We concluded that sputtered AuFe multilayers were necessary to determine any difference between the AuFe and CuMn behaviors, and such a study also became part of this thesis.

1.6.3 Critical Behavior of CuMn

A phase transition involves a divergence in the free energy (or its derivatives) of a system, which in turn create divergences in its physical properties such as the specific heat or magnetic susceptibility. Analysis of critical behavior attempts to describe the form of these divergences, characterized by algebraic expressions typically containing the critical temperature, T_C, and *critical exponents*. Critical exponents of interest to this discussion are described in the following table.

Table 1.1 Definitions of critical exponents

	Exponent	Defined
γ	Magnetic Susceptibility Exponent	$\chi \sim (T-T_c)^{-\gamma}$
ν	Correlation Length Exponent	$\xi \sim (T-T_c)^{-\nu}$
β	Order Parameter Exponent	$q \sim (T-T_c)^{-\beta}$
z	Dynamic Exponent (For relaxation time τ)	$\tau \sim \xi^z$
θ	Free Energy Exponent (for excitation at length scale L)	$F \sim L^{\theta}$
Ψ	Barrier Exponent (for relaxation of an excitation at length scale L)	$B \sim L^{\Psi}$

One attempts to fit experimental data to an appropriate form and thereby determine the values of T_C and the relevant exponents. Systems that can be described with the same critical exponents are believed to be a result of the same underlying physics, and said to be in the same *universality class*. Thus the exponents for 3D should differ from those for 2D. Finding critical exponents in thin samples can help determine where the 3D $\rightarrow$ 2D crossover occurs, or if in fact a non-zero T_C exists in the 2D limit.

1.6.3.1 Critical Slowing Down

As mentioned in Section 1.3, the relaxation time for a system with a phase transition ($d \geq d_l$) should diverge as Equation 1.1. Fitting Equation 1.1 to data for a bulk sputtered film of $Cu_{0.86}Mn_{0.14}$ revealed reasonable exponents and a T_c very close to the quasi-static T_f (see above). Below d_l, there is no phase transition, so the dynamics of the system should be governed by a thermally activated process. Such *activated dynamics*, derived from a theoretical approach based on the droplet model, are represented by[86]

$$ln\left(\tau/\tau_o\right) \sim T^{-(1+\psi\nu)}.$$

This equation involves both the correlation exponent and the relaxation barrier exponent as defined in Table 1.1. Defining T_f as the temperature where the measuring time and relaxation time are equal, the equation may be rewritten as

$$ln\left(\tau_m/\tau_o\right) \sim T_f^{-(1+\psi\nu)} \qquad \text{Equation 1.5}$$

Analysis using Equation 1.1 performed on a $Cu_{0.86}Mn_{0.14}$/Cu multilayer with W_{SG} = 3 nm gave values of $T_f \sim T_c$ = 26K, $\log_{10}\tau_o$ = -10, and $z\nu$ =19. The latter two values are far outside of their expected range, causing the authors to try the activated dynamics. Using Equation 1.5, a good fit was found with T_c = 0K and $\psi\nu$ = 1.6.[26,92] More complete examination of uncertainties yielded $0 < T_c < 10$K and $1.6 > \psi\nu > 1.1$.

Both static and dynamic analysis of CuMn/Cu multilayers show a change in the critical exponents that strongly suggest that by W_{SG} = 2 - 3 nm a 3D to 2D crossover has occurred.

1.6.3.2 Nonlinear Susceptibility Scaling

When experimentally determining critical exponents, it is necessary to measure properties that are sensitive to the ordering. In SGs, the higher order terms in the expansion of the magnetization

$$M/H = \chi_0 + \chi_2 H^2 + \chi_4 H^4 + \cdots$$

are more sensitive to the SG order than is the zero-field susceptibility.[3] Here χ_0 is the linear susceptibility, and the remaining terms constitute the nonlinear susceptibility, χ_{nl}. Two different equilibrium χ_{nl} studies have been done on thin SG samples; high field magnetization, and low field a.c. susceptibility. Since the system must have time to relax into equilibrium, these measurements must be taken far enough above T_f so that the relaxation time is smaller than the measuring time.

For high fields, scaling theory predicts[87]

$$\chi_{nl}(H,T) \sim t^{\beta} F(t / H^{2/(\gamma+\beta)}), \qquad \text{Equation 1.6}$$

or, alternatively,

$$\chi_{nl}(H,T) \sim H^{2\beta/(\gamma+\beta)} G(t / H^{2/(\gamma+\beta)}), \qquad \text{Equation 1.7}$$

where F and G are scaling functions, $t = (T-T_C)/T_C$ and β and γ are critical exponents as defined in Table 1.1.

In the low field limit, the χ_2 term dominates. A low field χ_{nl} measurement involves superimposing a small oscillating field on a static field, so that $H=H_0+h\sin\omega t$. Here, χ_2 is expected to scale as[90,88]

$$\chi_2 \sim t^{-\gamma}. \qquad \text{Equation 1.8}$$

Gavrin et al.[82] were the first to use high field nonlinear susceptibility scaling on thin SG layers. Data from a W_{SG} = 6 nm $Cu_{0.92}Mn_{0.08}/Al_2O_3$, previously shown to exhibit a size effect T_f decrease (see Section 1.6.2.1) and data for a bulk CuMn sample were fit to Equation 1.6. Exponents for W_{SG} = 6 nm of $\beta = 0.85$ and $\gamma = 5.1$ were found using $T_c = T_f(W_{SG}=6\text{ nm}) = 17.5$ K. No information was given on the effect of T_c choice on the fit. The exponent values differed from those found in the bulk sample, (β=0.9, γ=3.0) leading the authors to conclude that a 3D to 2D crossover had occurred.

A similar high field study was later done on a $Cu_{0.14}Mn_{0.14}/Cu$ sample made by Kenning (described in Section 1.5.1.1), with W_{SG} = 2 nm. Fitting the data to Equation 1.6, the data best scaled to a single curve with values of $T_c = 0$ and exponents $\beta = 0$ and $\gamma = 9.2$.[89]

Since high field fits are not very sensitive to the choice of T_c,[90] other techniques such as low field fits should be used in combination with the high field results. The same CuMn/Cu W_{SG} = 2 nm sample discussed above was measured and fit with Equation 1.8, and best fits were obtained with $T_c = 0 \pm 5$K (by setting t = T) and $\gamma = 9.3$,[89] in good agreement with the values from the high field χ_{nl} scaling. Although these values differ from those found for the $CuMn/Al_2O_3$ W_{SG} = 6 nm sample, the results for both samples suggest a 3D to 2D crossover has occurred.

1.6.4 Aging

Aging studies involve measurement of the ZFC relaxation rate,

$$S(\tau_m) = \frac{1}{H}\left(\frac{dM_{ZFC}}{d\ln\tau_m}\right),$$

after various wait times, τ_w. Two regimes should be considered: a) $\tau_m << \tau_w$. When the measuring time is much smaller than the waiting period, the length scales probed (by τ_m) are much shorter than those over which the SG has relaxed (during τ_w), allowing study of

equilibrium behavior. b) $\tau_m \geq \tau_w$. The behavior is non-equilibrium, for the length scales probed are longer than the relaxation lengths.

For the equilibrium case, $\tau_m << \tau_w$, a 3D SG exhibited two behaviors as τ_m was increased, as illustrated by data for bulk CuMn films made by Kenning. The imaginary part of the complex susceptibility, $\chi(\omega)''$, increased with increasing frequency (or decreasing measuring time since $\omega \sim 1/\tau_m$),[91] and $S(\tau_m)$ first decreased, passed through a minimum, and then increased, peaking at $\tau_m \sim \tau_w$. Moving to the non-equilibrium regime, $\tau_m > \tau_w$, $S(\tau_m)$ decreased as τ_m increased.[91,92]

The aging behaviors for $Cu_{0.86}Mn_{0.14}$/Cu multilayers with W_{SG} = 2 and 4 nm were also measured. The W_{SG} = 4 nm sample showed qualitatively similar behavior in $S(\tau_m)$ to that found for the 3D sample in the non-equilibrium regime, with $S(\tau_m)$ decreasing as τ_m increased.[93] The W_{SG} = 2 nm sample showed just the opposite trends in the equilibrium regime as those found in 3D. $S(\tau_m)$ increased with increasing τ_m,[26,94] and $\chi(\omega)''$ decreased with increasing ω.[92] Both these behaviors are seen in the 2D Ising SG $Rb_4Cu_{0.78}Co_{0.22}F_4$.[95]

In the non-equilibrium regime, $\tau_m > \tau_w$, these measurements show qualitatively similar behavior between the 3D film and W_{SG} = 4 nm. In the equilibrium regime, $\tau_m << \tau_w$, qualitatively different behavior was seen between 3D and W_{SG} = 2 nm. The W_{SG} = 2 nm sample is perhaps 2D in character, supported by the similarity between its behavior and the 2D Ising SG above.

1.7 Insulating SG Systems

Only one study of finite size effects with decreasing W_{SG} in an insulating SG has been published, on superlattices of $Cd_{1-X}Mn_XTe/CdTe$.[96] Instead of a shift in the susceptibility peak, the authors reported the peak broadened and disappeared as W_{SG} decreased. The reasons for this behavior are not known.

A more conclusive study on a 2D Ising SG $Rb_2Cu_{0.78}Co_{0.22}F_4$ was performed by Dekker et. al..[90,95,97] Like a 3D sample, this system showed a weakly time dependent peak in χ_l with irreversibility below T_f. The high and low field χ_{nl} measurements fit well to Equations 1.7 and 1.8 giving $T_c \sim 0K$, $\beta \sim 0$, and $\gamma \sim 4.5$. The T_c and β values are the same as those found for the 2D CuMn/Cu samples above, but the exponent γ is lower.

Also like the 2D CuMn/Cu SG, the $Rb_2Cu_{0.78}Co_{0.22}F_4$ was described by the activated dynamics of Equation 1.5. Good agreement was found between the static and dynamic values of T_c, β, and γ. The aging behavior below T_f was similar to that found in the 2D CuMn/Cu SG.

1.8 Coupling

1.8.1 Static measurements

The SG layers in the finite size effect studies described above were deliberately magnetically decoupled by thick ILs of 30 nm Cu or Ag or 7 nm of Si. Preliminary findings of Kenning et. al. using only 9 nm of Cu and 1.2 nm of Si, showed no significant finite size effects with SG thickness,[98] due to insufficient decoupling of the SG layers. To determine the appropriate decoupling value for the Si IL, Kenning et. al. fixed W_{SG} at 7 nm and varied W_{IL} from 3 to 14 nm. They found T_f to be independent of W_{IL} down to at least 3 nm of Si,[74] indicating that the coupling between the SG layers did not extend

beyond this limit. A similar experiment showed that coupling between 4 nm thick CuMn layers extended out to ≥ 20 nm in Cu.[99] Stubi et. al. found similar long range coupling of CuMn through Ag,[100] and of 4 nm thick layers of AgMn through both Cu and Ag.[81,101] This coupling length through the metal ILs is unusually long, especially compared to those found for layers of magnetically ordered materials. Fe layers couple up to 2 to 6 nm through normal metal layers.[102] Materials with spiral order display a longer range coupling more comparable to the SG case. These elements, such as Dy, contain spiral spin density waves (SDWs) and are able to induce SDWs in a certain normal separator layers (such as Y). The SDW induction is possible when the IL is energetically close to supporting SDW formation (see Section 1.4.4). These systems may couple through as much as 13 nm of their separator material,[103] provided the c axis of the HCP crystals is grown perpendicular to the layers (coupling is much shorter along other axes).[104]

As noted in Section 1.4.4, CuMn and AgMn contain finite correlation length SDWs. Perhaps the ILs Cu and Ag allow the same SDW induction process to occur. Tests of different IL materials were needed to determine if this is a plausible explanation and what other factors may affect this coupling length. Part of this thesis uses different ILs to address these issues.

1.8.2 Dynamic Studies of Coupling

In 1992, after this thesis work had begun, coupling effects were studied for the CuMn/Cu systems discussed above using the dynamic relations in Sections 1.6.4 and 1.6.3.1. Granberg et. al. found, through scaling time dependent susceptibility data with the relaxation time scaling Equations 1.5 and 1.6, that some interaction occurred through W_{IL} even greater than 30 nm. For W_{SG} = 4 nm, typical 2D behavior was occurred for

$W_{IL} \geq 60$ nm. When $60 < W_{IL} < 3$ nm, a gradual decoupling of the CuMn layers was observed, and for $W_{IL} < 3$ nm the SG displayed 3D dynamic behavior.[105]

Mattsson et. al.[94] also studied these CuMn/Cu samples, and found that the form of the relaxation rate $S(\tau)$ indicated that the multilayers returned to 3D character as W_{IL} was thinned. $W_{IL} = 30$ nm showed 2D type aging behavior, while $W_{IL} = 10$ nm, $S(\tau)$ started to resemble a 3D system (see Section 1.6.4), with a minimum occurring at approximately T_f. This was explained in terms of a domain model, where domain growth exceeds the interlayer thickness at the time the system behaves as 3D.

1.9 Project Goals

The preceding work led this project to have 4 major goals related to finite size effect in SGs.

First, to extend measurements of the CuMn/Cu and AgMn/Ag systems to W_{SG} as thin as possible, to answer the following questions:

1) Will the general scaling law of Equation 1.3 continue to fit data as $W_{SG} \rightarrow 1$ monolayer (ML), or can a region be reached where the scaling law cannot apply?

2) Will the droplet model power law prediction hold down to $W_{SG} = 1$ ML, and if so will the value of the exponent *a* be the same as that previously found for $W_{SG} \geq 20$ nm?

3) The short range 2D insulating SG described in Section 1.7 gave $T_f > 0$ K. Will $T_f \rightarrow 0$ as $W_{SG} \rightarrow 1$ ML in a long range metallic SG?

Second, to replace the Cu and Si ILs previously used with different materials, to determine the following: Do metal ILs other than Ag and Cu reproduce the same CuMn/Cu curve of Figure 1.7 ? To answer this question, ILs will be used that may introduce a range of stress and roughness to the interface.

Third, attempt a similar finite size effect study with SGs that differ from CuMn in anisotropy and interaction type to investigate the following:

1) Higher anisotropy is expected to lower d_l, will this effect the finite size curve, causing it to fall slower (or faster) with W_{SG} reduction for a SG with higher anisotropy than CuMn and AgMn?

2) Different interactions are expected to affect d_l, will a difference be seen in the finite size curve of a SG interactions other than RKKY-type?

The choices for the new SG materials are AuFe, similar to CuMn but with higher anisotropy, and the SG NiMn, with short range rather than the long range RKKY type interactions.

The fourth goal also involves an interesting trait of NiMn. For Mn concentrations between ~16 and 24 at.% the material has a reentrant (RSG) regime (see Section 1.4.1). Here there are two transitions as the temperature is reduced; paramagnetic to ferromagnetic (or ferro-SG mixed phase (FSG)), and then FSG to SG phase (see Chapter 5). This behavior raises the additional questions of whether the reentrant regime behaves like the SG regime, and how the characteristic temperatures for the P-FSG transition and the FSG-SG transition behave in response to layer width reduction.

The multilayer geometry and materials used in these systems naturally suggests one further experiment: to test the coupling through the differing interlayers to answer the following:

1) Do metal ILs other than Cu and Ag allow long range (~ 20 nm) coupling?

2) Do properties such as electrical resistivity, free electron density, or interface effects affect the coupling length?

Materials for ILs will be chosen for their distinguishing properties, such as differing crystal structure, lattice size, resistivity, spin-orbit coupling ability, and electronic structure.

CHAPTER 2

THEORY

2.1 Mean Field Theory Models

As mentioned in Chapter 1, SGs have presented a difficult problem to mean field theory, causing progress to be heavily reliant upon numerical methods. Mean field models are, however, the starting point for the Monte Carlo d*l* results reviewed in Section 1.5 , and understanding these models and the degree to which they represent experimental SGs lends validity and insight to the numerical results. The following briefly reviews the development of mean field theory for SGs. For more a more detailed review, see reference 3.

The bulk of theoretical effort in this area has been based on variants of the model by Edwards and Anderson (EA).[106] In the canonical SG, the random spin placement plus the oscillatory RKKY interaction lead to random interactions between ions. The EA model simplifies this situation by replacing the site disorder with bond disorder, allowing the spins to be placed on a regular lattice. The Hamiltonian for Heisenberg spins in this system is

$$\mathcal{H} = \frac{1}{2}\sum_{i,j} J_{ij}\vec{S}_i \cdot \vec{S}_j + H\sum_i S_i^z$$

where J_{ij} results from a random distribution. EA considered nearest neighbor interactions only.

To determine whether the model exhibits the thermodynamic properties of a SG, the free energy (F) must be calculated for the system by averaging over all possible states. In non-random systems, or random systems where the observation time, τ_m, is longer than the typical fluctuation time, τ_f, of the random variables x, all possible states may be sampled. F may then be calculated as

$$F = -k_B T ln[Z]_{av}$$

where the partition function, Z, is given by

$$Z\{x\} = \underset{\{S_i\}}{Tr} exp\left[-\mathcal{H}\{x, S_i\} / k_B T\right].$$

Here the random variables are the bond strengths denoted by J_{ij}. In the case of the SG, $\tau_m << \tau_f$, and one cannot average over the partition function. The average must instead by taken over the free energy, to include all possible configurations with the same free energy,

$$F = -k_B T[lnZ]_{av}.$$

The need to average over lnZ rather than Z is a source of difficulty in performing statistical mechanics in random systems. EA used a method to do this average known as the *replica trick*, where the identity

$$[ln Z]_{av} = \lim_{n \to 0} \frac{\left[\left(Z^n\right) - 1\right]}{n}$$

is used and n identical replicas of the system, Z may be written as

$$Z^n\{x\} = \prod_{\alpha=1}^{n} Z_\alpha\{x\} = exp\left[-\sum_{\alpha=1}^{n} \mathcal{H}\left\{x, S_i^\alpha\right\} / k_B T\right].$$

For positive n this expression is more readily averaged. .

To characterize the phase transition, an order parameter is needed (analogous to the magnetization in ferromagnets). An order parameter signals the transition to a correlated phase by becoming non-zero at the transition temperature. Since there did not appear to be any spatial correlations between spins, EA proposed an order parameter to correlate the spins in time. As $t \rightarrow \infty$ this order parameter would average over all possible time scales and converge to a constant value

$$q = \lim_{t\to\infty} \langle\langle S_i(0) S_i(t) \rangle\rangle \ .$$

Here the thermal average is taken before the configurational average. The EA model has been extensively studied for Ising spins, and predicts a cusp in the zero field susceptibility. The order parameter q is found to decay become zero for $T > T_f$ and to a constant value for $T < T_f$, indicating a change from paramagnetism to a state with temporal correlations.

Sherrington and Kirkpatrick (SK), in an effort to imitate the recent success in the theoretical descriptions of ferromagnetism, applied mean field theory to the EA model.[107] While normally an approximation, mean field theory for ferromagnetism becomes exact in the limit of infinite-range interactions.[3] SK therefore replaced the short ranged interactions in the EA model with infinite ranged interactions. The resultant mean field theory in the SK model predicted a second order phase transition and a cusp in the zero field susceptibility, but also a cusp in the specific heat where none is observed experimentally. SK also determined that their solution gave negative entropy due to unstable solutions for $T < T_f$.

The SK solution relied on invariance to permutations of the spin indices in the Hamiltonian when calculating the average of lnZ. While this is true for positive integer values of n, Parisi suggested that it is not true if $n \rightarrow 0$.[9] This idea led to what is believed to be the exact solution of the SK model, found through replica symmetry breaking. The symmetry is broken by requiring all quantities involving a replica to be replica independent, resulting in an infinite number of order parameters. While this solution is

inherently very complex, it does provide a stable solution for $T < T_f$ and predict more subtle features of the SG state, such as the additional boundaries in the magnetic phase diagram of Figure 1.6.

Mean field theory gives a finite transition temperature for SGs, but it gives incorrect results for critical exponents.[108] The model does, however, share enough features with real SGs to have become the most widely used base for Monte Carlo calculations to address dimensionality questions about SG systems. A few exceptions exist; Bray, Moore and Young,[70] cited in Section 1.5 , used a site disorder model to determine that vector SGs with RKKY-like interactions are at their lower critical dimension in 3D. Others, not described in Chapter 1, have used 3D RKKY-type Heisenberg site disorder SG models to determine that anisotropy is needed to induce a transition,[109] or that $T_C = 0$.[110]

2.2 Finite Size Scaling

A true thermodynamic phase transition contains a singularity in the free energy, F, only when calculated in the thermodynamic limit of infinite volume and number of particles. This singularity in F in turn often creates singularities in its derivative physical properties, such as the specific heat and magnetic susceptibility. Although real systems do not extend quite to the thermodynamic limit, many still show apparent singularities which agree with theoretical statistical mechanical calculations. The approach to a critical temperature, T_C, may be characterized by algebraic expressions, the leading term in which is $\left(\frac{T-T_c}{T_c}\right)^m$, where m is a *critical* exponent. The first step to finding a critical exponent comes from Landau theory[111],[112]. The ordering of a system due to a phase transition is described by an order parameter, such as the magnetization, M, in a ferromagnet. The

free energy, F, is then expanded in terms the order parameter. For the example of a ferromagnet, it is helpful to define the alternate free energy function, A = F + MH. Since dF = -SdT - MdH, where T is the temperature, a Legendre transformation gives

$$dA = -SdT + HdM.$$

Now

$$H = \left(\frac{\partial A}{\partial M}\right)_T \quad \text{and so} \quad \chi^{-1} = \left(\frac{\partial^2 A}{\partial M^2}\right)_T.$$

Expanding A in powers of M so that

$$A = A_0(T) + A_2(T)M^2 + A_4(T)M^4 + \ldots,$$

where odd powers of M are excluded due to symmetry M ↔ -M, and then expanding the coefficients in powers of $t = (T-T_C)/T_C$, one gets for the zero field susceptibility:

$$\chi^{-1} = A_{2,0} + 2A_{2,1}t + O(t^2).$$

The leading term contains $\left(\frac{T-T_c}{T_c}\right)^m$, where $m = -1$. This critical exponent value proves to be incorrect experimentally, not surprising since the expansion assumes that the free energy function is analytic about T_C. From the original work of Widom[113], the phenomenological practice of scaling arises allowing the exponents and T_C to be fitting parameters to compare the theoretical form to experiment. Systems that have phase transitions described by the same critical exponents are believed to operate under the same physical mechanisms, and so are said to belong to the same universality class.

One critical exponent of particular interest to the subject of finite size effects is the *correlation exponent*, ν, defined by

$$\xi \sim t^{-\nu} \qquad \text{Equation 2.1}$$

where ξ is the correlation length. This correlation length may be limited by the size of the sample, and since phase transitions occur via growth of correlations towards infinity, the nature of the phase transition is also affected by the size of the sample. As a result, as a system is reduced in size, the real behavior near the singularity begins to deviate from that seen in the bulk. For a system described by a large but finite dimension L, the critical temperature shifts according to[77]

$$\frac{T_c - T_c(L)}{T_c} \sim L^{-\lambda}, \qquad \text{Equation 2.2}$$

where λ is defined as the *shift exponent*.

Fisher and Ferdinand[114] assert that the shift exponent may be related to the correlation exponent ν of Equation 2.1 by realizing that finite size effects occur when the correlation length at $T_C(L)$ equals the finite length L. Setting ξ = L in Equations 2.1 and 2.2, we get

$$\lambda = \frac{1}{\nu} \quad \text{so that} \quad \frac{T_c(L) - T_c}{T_c} \sim L^{-1/\nu}. \qquad \text{Equation 2.3}$$

This is a generic result for a finite length scale L. In the layered samples reported in this thesis, L = W_{SG}, the width of the SG layer, T_f^b replaces T_C, and T_f replaces $T_C(L)$. Equation 2.3 then becomes

$$\frac{T_f(W_{SG}) - T_f^{\,b}}{T_f} \sim W_{SG}^{-1/\nu}. \qquad \text{Equation 2.4}$$

This is the relationship used to derive the exponent ν from data. Formally, it should only be valid for $T_f \sim T_f^b$.

2.2 Droplet Excitation Model (D.A. Fisher, D. Huse, 1986)

In 1987, Fisher and Huse[83] formulated a scaling theory specific for SGs that may be applied when $T_f(W)$ is far away from T_f^b. This droplet excitation model is an attractive choice for size effect studies, as it includes spatial dimensionality from its onset. (Other commonly used models tend to be in the category of infinite range interactions (Sherrington-Kirkpatrick) or short range models which have not been successfully analyzed for any spatial dimensionality.) The low lying excitations that may disrupt SG ordering are pictured as clusters (droplets) of coherently flipped spins. The free energy associated with the flipping of a droplet of length scale L , in units of some microscopic length, is

$$F \sim YL^{\theta}$$

where Y is an interfacial tension, and $0 < |\theta| \leq (d-1)/2$ where d is the dimension. The lower critical dimension, d_l, is assumed to lie between 2 and 3, meaning a phase transition occurs in 3 dimensions but not in 2. When $d = 2 < d_l$, θ_2 (where the subscript denotes the dimensionality) must be negative, allowing large scale excitations to exist at low energies, destroying the SG order at finite temperatures. The relaxation barrier for the droplets also scales as L,

$$B \sim L^{\psi}.$$

For a film, of finite thickness W, that is infinite in two dimensions, two regimes shall be considered (i) low temperature where $T << T_c$, and (ii) critical, where $T \sim T_c$.

(i) Low temperature $T << T_c$

When $L < W$, the system behaves 3D, and the free energy scales with a 3D exponent

$$F \sim W^{\theta_3}.$$

The temperature is then renormalized to keep the renormalized energy scale of order unity,

$$T_R(L) \sim T \cdot W^{-\theta_3}.$$

At lengths $L > W$, the system behaves 2D, and the temperature is renormalized again using the 2D exponent

$$T_R(L) \sim T \cdot W^{-\theta_3} \left(\frac{L}{W}\right)^{|\theta_2|},$$

where $\theta_2 < 0 < \theta_3$, since $2 < d_l < 3$.

When $T_R(L) \sim 1$ entropy dominates and disorder occurs. This happens when $L = \xi$, yielding

$$\xi \sim T^{-\nu_2} W^{1+\nu_2\theta_3} \quad \text{where} \quad \nu = \frac{1}{|\theta|} \qquad \text{Equation 2.5}$$

The barrier heights also scale in a similar manner:

$$\underline{L \sim W} \qquad B_W \sim W^{\psi_3}$$

$$\underline{L \sim \xi} \qquad B_\xi \sim \left(\frac{\xi}{W}\right)^{\psi_2} W^{\psi_3}$$

So that the relaxation time,

$$\tau_L \sim \exp[\, B/T \,] = T^{-(1+\nu_2\psi_2)} W^{\psi_3+\nu_2\psi_2\theta_3},$$

increases as T decreases. At some point, $\tau_L \geq t_m$ (measuring time) causing the system to fall out of equilibrium, appearing to freeze, at temperature $T = T_f(t_m)$

$$\frac{T_f(t_m)}{T_c} \sim \left[\frac{W^{\psi_3+\psi_2\nu_2\theta_2}}{ln(t_m)}\right]^{\frac{1}{1+\nu_2\psi_2}}$$

For fixed t_m,

$$\frac{T_f}{T_c} \sim W^a \quad \text{where} \quad a = \frac{\psi_3 + \psi_2\nu_2\theta_3}{1+\nu_2\psi_2} \qquad \text{Equation 2.6}$$

A rigorous upper bound on a can be obtained from a general dimensionality argument which states $\theta_d \leq \psi_d \leq d\text{-}1$. This gives for $d=3$ $\theta_3 \leq \Psi_3 \leq 2$ resulting in $a \leq \psi_3 \leq 2$. To try to better restrict the value of a, we've gathered values for ψ, ν, and θ from theory and/or experiment in the literature. Monte Carlo calculations on Ising short range SGs put a lower bound of 1 on the parameter $\Psi_2\nu_2$[115]. Fitting studies of temperature dependent relaxation times in thin CuMn films to a generalized Arrhenius law, $\ln\tau \sim T^{(1+\psi\nu)}$, sets an upper bound on this parameter of 1.6[116]. Similar studies done on $Rb_2Cu_{0.88}Co_{0.22}F_4$, a 2D short-range Ising SG with random nearest neighbor bonds, yield a value of $\Psi_2\nu_2 = 2.2$.[117] Also, non-linear susceptibility divergence and relaxation time studies on CuMn provided boundaries on θ_2 and Ψ_3. Composing all these values together,

$$0.2 \leq \theta_2 \leq 0.3$$

$$1 \leq \Psi_2\nu_2 \leq 2.2$$

$$0.5 \leq \Psi_3 \leq 1$$

allows an estimate of $0.3 \leq a \leq 0.65$.

This result should be good for $T_f << T_f^b$ where W is small, but greater than the average impurity spacing.[83] All the SGs we've studied have an FCC lattice, giving 12

nearest neighbors for each atom. For impurity concentrations ~ 10 at.%, the average separation is on the order of one atomic spacing.

Note that the limits from the literature averages include values from a short-range Ising SG, whereas CuMn is long-range Heisenberg type. This combination may pose a problem, since there is some evidence that short range Ising SGs and long range RKKY-like SG are in different universality classes[69], and systems in different universality classes in general have different critical exponents.

(ii) Critical region $T_f \sim T_c$

Near the bulk transition temperature, we define $t \equiv (T - T_c)/T_c$. Here the relaxation time scales with the dynamical critical exponent $\tau(W,T_c) \sim W^{z_3}$, and $\tau(W,T_c) < t_m$, so that the system will not fall out of equilibrium before the correlation length grows to the film thickness (or no finite size effects would be seen). The correlation length below T_c, as indicated in the previous section, is thus less than W: $\xi \sim |t|^{-\nu_3}$.

For excitations $L<<W$, the free energy again scales as

$$F_L \approx Y_3(t) L^{\theta_3} \quad \text{where} \quad Y_3 \sim |t|^{\nu_3 \theta_3}.$$

and for $L>>W$,

$$F_L \sim Y_2(t,W) \quad L^{\theta_2}.$$

Here, where L~ W, Y_2 may be found by matching to Y_3. Using Equation 2.5, the 2D correlation length becomes:

$$\xi \sim W^{(1+\nu_2\theta_3)} |t|^{\nu_3\theta_3\nu_2}.$$

The barriers scale in a similar fashion as in the previous section,

At scale W $\quad B_W \sim |t|^{\nu_3 \psi_3} W^{\psi_3}$

At scale ξ $\quad B_W \sim B_w \left(\frac{t}{W}\right)^{\psi_2} \sim \left(|t|^{\nu_3} W\right)^{\psi_3 + \nu_2 \psi_2 \theta_3}$.

Making use of the relaxation time as before, and for long measuring times $\tau_m >> \tau$, an expression analogous to Equation 2.6 is found

$$\frac{T_f^{\,b} - T_f(\tau_m)}{T_f^{\,b}} \propto W_{SG}^{\;-(1/\nu)} \left[ln\left(\frac{\tau_m}{W_{SG}^{\;z}}\right)\right]^{-[(\psi_3 + \nu_2 \psi_2 \theta_2)\nu_3]^{-1}} \qquad \text{Equation 2.7}$$

This expression differs from Equation 2.4 only by a weak logarithmic factor involving τ_m.

CHAPTER 3

SAMPLE FABRICATION

All samples referred to in this thesis were grown at MSU in the dc magnetron sputtering system shared by the condensed matter group. Technical details of this apparatus are given elsewhere.[118] The following gives the necessary explanations of sputtering preparation, parameters, and materials used.

3.1 Target Production

The elemental targets Ag and Cu were purchased as 0.25" plates from Angstrom Sciences[119] and cut to a cylinder of 1.25" diameter by the Physics Shop staff at MSU. The Al, Mo, and Si targets were purchased precut to the above size from Tosoh SMD Inc.[120], and the V target was bought precut from Demetron Inc.[121]. The companies have stated the purity of these elemental targets to be

Table 3.1 Purity of elemental targets

Cu	99.999%
Ag	99.999%
Al	99.999%
V	99.9%
Mo	99.99%
Si	99.999%

Alloy targets CuMn, AgMn, AuFe, and NiMn, and the pure target Au target, were all made by us in an rf-induction furnace. The raw materials were of the following form and purity

Table 3.2 Purity of raw materials used in melted targets

material	purity	form	source
Cu	99.9999%	small pellets	Johnson-Mathey Electronics[122]
Ag	99.9999%	small pellets	Johnson-Mathey Electronics
Au	99.99%	wire	Sigmun Cohn Corp.[123]
Mn	99.9%	chips	Angstrom Sciences
Fe	99.9%	chips from old precut target	Tosoh SMD Inc.
Ni	99.99%	large pellets	Angstrom Sciences

The pellets or chips from each material were cleaned in a dilute nitric acid solution (H_20:$N0_3$ 10:1) before loading into a graphite crucible. For all metals excluding Ni, the inside of the crucible was coated with boron nitride, a generally inert substance which prevents contamination of carbon from the crucible. The reactivity of Ni at high temperatures with such a nitrogen compound precluded this approach for NiMn alloying. If BNO_3 is used to line the crucible, the molten NiMn dissolves a significant amount of nitrogen, which is then expelled as a gas (along with some molten metal) as the solubility of the nitrogen decreases in the cooling alloy. For this material it was necessary to purchase smaller alumina crucibles to use as a liner, and cut a graphite crucible to fit around them. Fortunately enough heat was radiated from the graphite and conducted through the alumina to melt the material. This arrangement limited the size of the NiMn

targets. Targets were made in three standard sizes. In order to reduce potential Cu contamination during sputtering (as explained in the next section) the NiMn were cut with a small extra "brim" along the bottom causing the target to resemble a hat.

Table 3.3 Melting temperature ranges and final size of targets

Target	Melting Temperature (C)	Final Size (diameter × thickness)
CuMn all concentrations	1080 - 1100	2.25" × 0.25"
CuGe 2 and 10 at.% Ge	~1010	2.25" × 0.25"
$Ag_{0.91}Mn_{0.09}$*	1000 - 1025	2.25" × 0.25"
Au	1060 - 1090	1.5" × ~0.15
$Au_{0.97}Fe_{0.03}$	1040 - 1130	1.5" × ~0.15
NiMn all concentrations	1340 - 1400	1 3/8" × 0.25" ("hat" cut)

*Melted by Michael Wilson

For all targets the base pressure inside the induction furnace quartz tube was ~ 5× 10^{-6} torr. The tube was then backfilled to ~250 torr with 90% Ar and 10% H_2 gas mixture, the H_2 removing residual oxygen from the chamber. Pure Ar was used in the case of NiMn, due to the high solubility of H_2 in Ni. Typically each melt was removed, turned over, and remelted one or two times to improve homogeneity. A cap made from a graphite crucible with a break in the side was frequently used on the NiMn to increase heating from the top. Temperatures were read on the outside of the glowing crucible with an optical pyrometer. The latest targets (the NiMn) were melted with the aid of a graphite cap made from another crucible. The cap, sensitive to the r.f. induction, adds heat to the top of the melting target, encouraging homogeneous melting. Melting was observed through a break in the cap (see Figure 3.1).

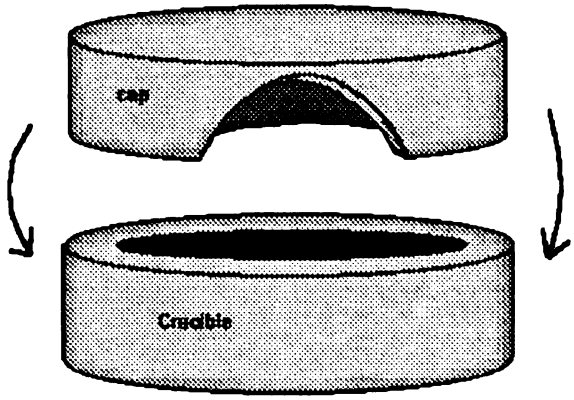

Figure 3.1 Graphite crucible and graphite cap

3.2 Sputtering

3.2.1 Sputtering Machine

The UHV compatible sputtering chamber holds four dc magnetron sputtering guns, a rotatable SPAMA (Sample Positioning and Mask Assembly) plate which can hold up to 16 samples, two available film thickness monitors (FTMs), two available thermocouples, and a liquid nitrogen cooling system for the SPAMA plate. A computer controlled stepping motor positions the SPAMA plate so as to hold the exposed substrate over the chosen sputtering gun for the appropriate time to produce the desired thickness of each layer.

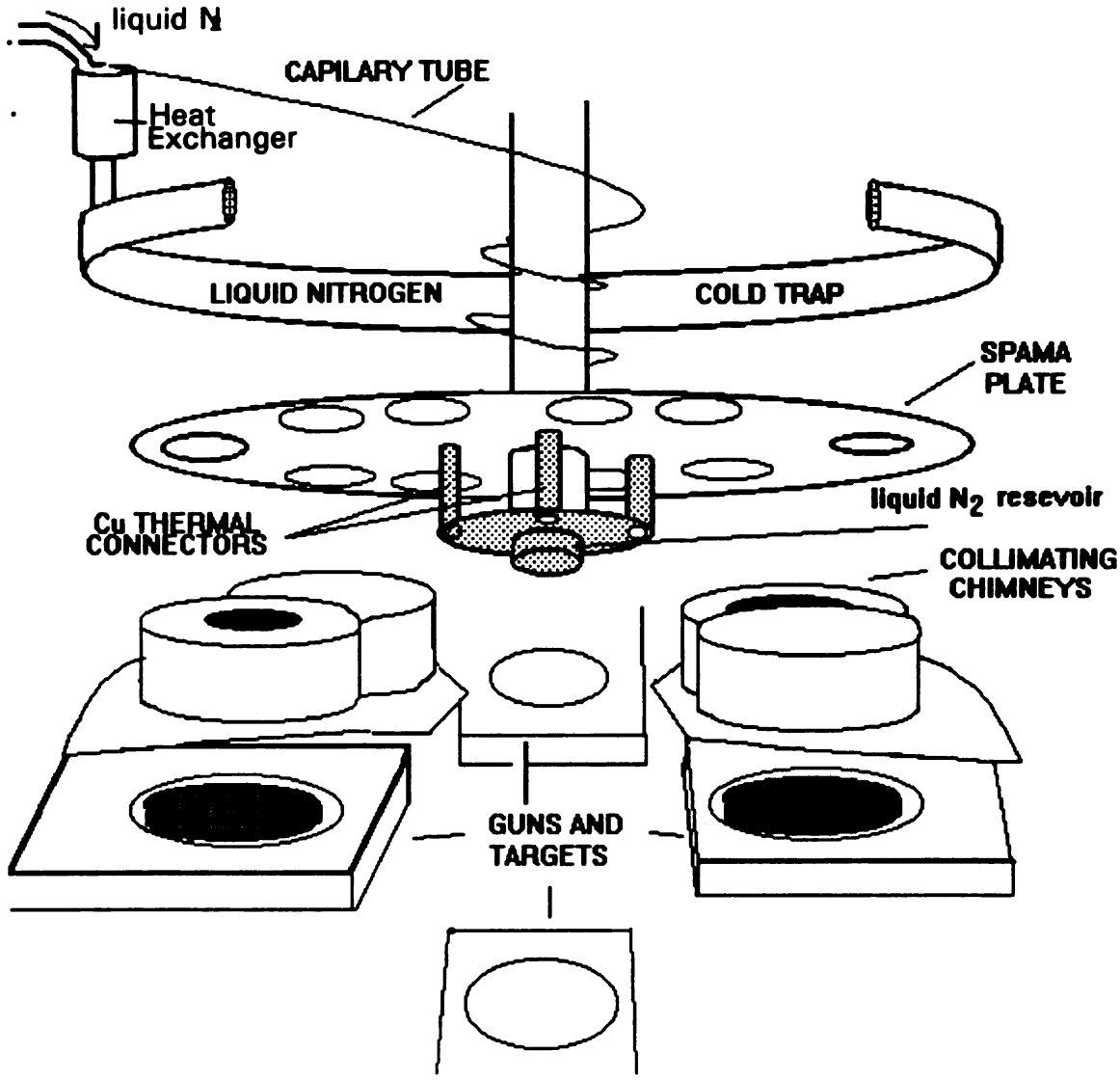

Figure 3.2 Schematic of inside of sputtering apparatus

A filament is located under one end of the gun parts, an anode at the other end. Electrons emitted from the filament speed towards the anode through a space between upper and lower gun parts, ionizing argon gas into a plasma. A negative voltage is applied to the target to attract the ions, causing sputtering.

Figure 3.3 Close-up of target and gun assembly

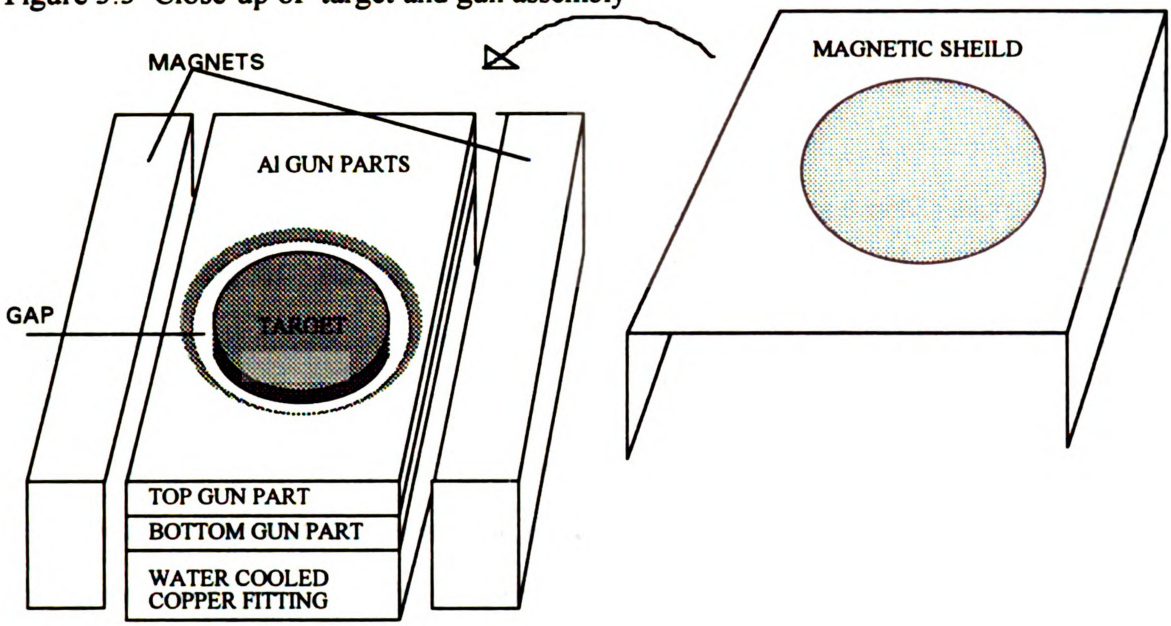

3.2.2 Cleanliness

It is the nature of the sputtering process to coat the machine parts surrounding the target with material from the target. It is necessary to remove this material in order to avoid contamination from the previous run and also assure the proper gap size between target and gun needed for operation.

The collimating chimneys between the sputtering guns and the SPAMA plate are not directly cleaned, rather the aluminum foil covering is changed between sputtering runs using different materials. The chimneys are kept clean between wrappings and are never handled without gloves. The aluminum SPAMA plate, substrate holders, substrate shutters, and sputtering gun parts are all etched in acid solutions to remove the deposits. Cu, CuMn, CuGe, Mo, and V are easily removed with a solution of 3:1 HNO_3:H_2O. Al, Si, and NiMn may be removed by the addition of ~10% HF acid. Caution must be

exercised when using this acid as it attacks the Al parts, which over time reduces their size. Because the fit of the gun parts to the sputtering machine is critical they are removed from the HF solution as soon as possible to reduce exposure. This may result in small amounts of sputtered material remaining on the gun parts. For this reason each material has its own associated gun parts. Ag and AgMn may be removed with a mixture of 1:1:1 H_2O: H_2O_2:NH_4OH. Au and AuFe required an exotic acid echant, and since their use was low were not etched. Any larger deposits were mechanically removed with a razor blade.

Other items in the sputtering chamber are not cleaned regularly because they are not exposed to the sputtering beam and therefore cannot contaminate the sample, or, as in the case of the magnetic confinement shield, are made of a material too reactive for acid etching. These items are however kept clean from other contaminants while not in the chamber.

The substrates used were <100> single crystal, polished, boron doped Si, cleaved into 0.5" squares from a Silicon Quest International[124] 3" round wafer. All substrates were cleaned with acetone and alcohol each for ~1 min. in an ultrasonic cleaner immediately prior to loading in the chamber.

Upon closure the chamber was baked for ~8 hours, after which pumping commenced until the base pressure was $\sim 2\times10^{-8}$ torr. Ultra High Purity Ar, run through a liquid nitrogen cold trap and a Hydrox purifier, was used to backfill the chamber to 2.5×10^{-3} torr for sputtering. The estimated impurity concentration at the sputtering pressure using this process is < 10ppm.

3.2.3 Cooling system

The sputtered atoms carry heat to the sample, so a cooling system is operated in order to control the growth temperature. Heat in the sample is transferred through the Si

substrate to an oxygen free high conductivity (OFHC) Cu block, which is thermally coupled to the SPAMA plate through an OFHC Cu shim. The SPAMA plate is cooled through contact with a liquid nitrogen reservoir filled by the capillary tube (see Figure 3.2). The capillary tube carries high pressure nitrogen gas to the heat exchanger, where it comes in contact with the liquid nitrogen used for the cold trap. The gas inside the capillary tube becomes liquefied, and then proceeds to the SPAMA plate reservoir.
The temperature reading is taken from a thermocouple atop the OFHC Cu block

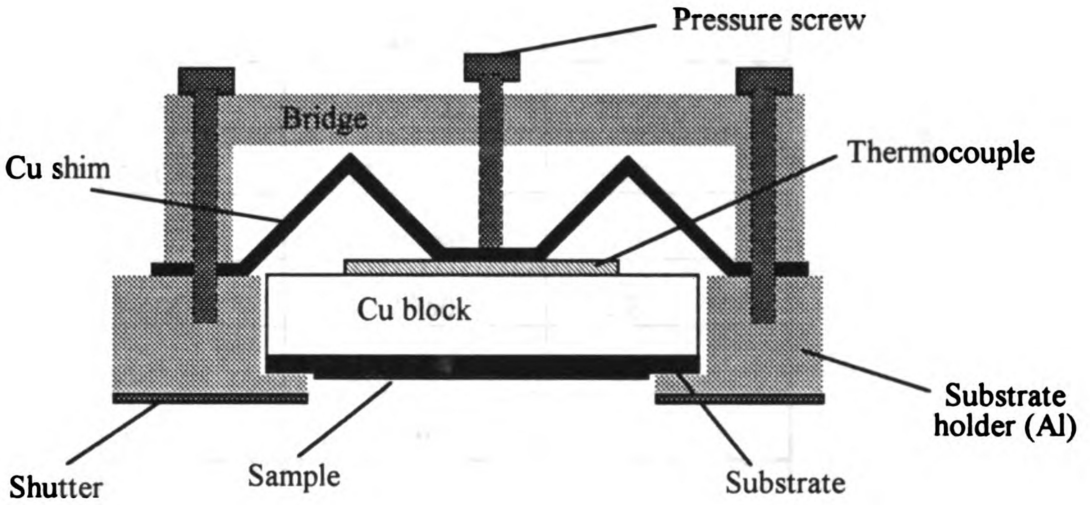

Figure 3.4 Sample holder

3.2.4 Sputtering parameters

All samples were sputtered under 2.5 mT pressure of the backfilled UHP Ar gas. The gas flow rates through the pinholes near the filament varied from 35-42 cm^3/min. The anode to filament voltage was typically 50-60V, and anode to filament current was 5-7 Amps. The Ar plasma to target voltage and current were adjusted to attain plasma stability and the desired sputtering rate (usually the highest rate possible). These

parameters were highly material dependent, affected by the target density, conductivity, and possibly other factors such as melting temperature. Although the computer was able to use deposition rates to calculate the timing needed to produce the desired thicknesses and move the sample to those locations, the plasma voltage and current must be monitored and adjusted against drift by hand.

Table 3.4 Plasma to target parameters and associated deposition rates

Material	Plasma to target V/I (kV/mA)	Deposition Rate (Å / second)
Cu	- 400/.700	14.0
CuMn	-400/.700	12.7
CuGe	-370/.600	10.8
Ag	-350/.480	6.0
AgMn	-400/.750	6.8
Au	-215/.400	8.5
AuFe	-320/.400	~6
Al	-300/.890	3.3
Mo	-325/1.10	8.8
V	-680/1.01	6.6
Si	-350/1.00	3.1

CHAPTER 4

SAMPLE CHARACTERIZATION

4.1 Compositional Analysis

All SG T_f values reported in this study were normalized by the T_f of a bulk sample of the same concentration in hopes of making the results for each series of samples concentration independent.[76] It is necessary, however, to check the actual sample concentration: a) to predict the sputtered concentration from a known target concentration; b) to determine any concentration drift throughout a sample series; and c) to compare T_f values with literature values.

Energy Dispersive X-ray (EDX) analysis was used to determine concentrations for both targets and sputtered samples. This non-destructive process uses a beam of electrons to excite the atoms into emitting characteristic x-rays. These x-rays are tallied, and three major corrections are made to the ratio between the number of x-rays from each element. The element with the larger atomic number has a larger cross section and will produce more x-rays (Z correction). The energy of a characteristic x-ray determines how likely it is to be absorbed before it escapes the sample (A correction) and how likely it is to create a secondary x-ray in the sample material (fluorescence or F correction). Together these are the ZAF correction factor, and when properly taken into account atomic concentrations can be calculated. When the ZAF factor is close to 1, few corrections are needed to the raw ratio. All EDX data was taken on a JOEL JSM-35C Scanning Electron

Microscope with a Tracor Northern X-ray detector, both belonging to the Center for Electron Optics at MSU. A hard x-ray aperture was used around the electron beam, where W, a strong Mo x-ray absorber, is deposited on the underside of the Mo ring opening to absorb any stray Mo x-rays that may be created by the beam. A physical barrier was placed around the detector to prevent backscattering background x-rays (mostly from the Cu chamber walls) from entering the detector. The x-ray counting, composition calculation, and any necessary peak deconvolution were done on a dedicated PC running Noran Inc. commercial software.

Although the presence of small amounts of material (<1 at.%) may be detected, low counting statistics makes analysis of elements comprising < 2 at.% difficult. The lowest concentrations checked with EDX were those of AuFe with 3 at.% Fe and CuGe with 2 at.% Ge. Most alloys were in the 10 - 25 at.% impurity range.

The accuracy of the concentration c for this method is ($c \pm 0.03c$) if the ZAF corrections are calibrated to scans of pure samples taken at the same electron energy. Without this calibration the error is closer to ($c \pm 0.07c$). Unfortunately nearly all the pure standards available were bulk pieces, thicker than the depth of the electron beam penetration. Only the thickest of the films made (1000 nm) are seen as bulk by the 20 kV electron beam. If the sample doesn't encompass the entirety of the tear shaped penetration area, two problems may occur: a) The substrate will produce x-rays which may then cause fluorescence in the sample. Fortunately x-rays from Si substrates are not energetic enough to excite the metallic atoms; also they do not overlap any x-rays of interest. b) The ZAF correction calculation assumes the entirety of the penetration area is encompassed by the sample when calculating the secondary effects, and some error is expected when this is not the case.

NiMn, with its abrupt change in magnetic behavior with concentration, was given the most attention. Because the ZAF factor is so close to unity for a NiMn alloy (typically

1.02), the error on the concentration was estimated by the Noran software to be less than (c ±0.07c) for a thin film[125]. This result, however, does not give any indication of potential systematic error between thick and thin films. Better concentration definition was needed, since some of the NiMn films with thicknesses 100 - 1000 nm showed different magnetic behaviors when the measured concentrations were the same. Three films of varying thicknesses were made of the same concentration by sputtering one third of each film at a time, switching between films until all were complete. The 1000 nm film, seen as bulk to the electron beam, was taken to read the true concentration, c, while the 300 and 100 nm films gave readings of 0.89c. Using this behavior as a calibration, corrections were made to the thin film values, after which consistency was achieved between concentration and magnetic behavior.

The CuMn and NiMn sputtered films were approximately the same composition as the target. AgMn and AuFe sputtered lower impurity concentrations than were originally in the target. Stubi et. al.,[81] in the AgMn study discussed in Chapter 1, measured a T_f^b in a bulk sputtered films of AgMn which was 40% lower than T_f^b measured from target chips. This corresponded to a drop from 15.5 at.% Mn to ~ 7 at.% Mn, a loss of more than 50% of the impurity. Since the effect was sensitive to the pressure of the Ar sputtering gas, it was postulated that the loss was due to larger scattering angles of the lighter Mn as it collided with the gas, preventing more Mn atoms than Ag atoms from reaching the sample. Since the AuFe system has even greater differences in atomic mass than the AgMn, a more pronounced effect was expected. Surprisingly, a similar loss of 50% was observed, suggesting that the scattering angle effect is not the only mechanism at work.

Concentration fluctuations in the CuMn and AgMn runs varied the T_f^b of thick sputtered films by a few percent between samples. AuFe concentration fluctuations gave rise to T_f^b variations of closer to 5%. Every NiMn target made produced film

concentrations that drifted or changed between runs, so T_f^b values from different runs with the same target could be quite different. This behavior necessitated the sputtering of many thick films; frequently every third or fourth NiMn sample grown was a thick film.

4.2 Mechanical Determination of Film Thickness (Dektak)

The film thickness monitors (FTMs) used to determine the rate of sputtering (and hence the eventual layer thickness) have a ± 1-2 % precision in their reading, but other factors, such as sputtering gun power fluctuations and change of FTM response with temperature, cause larger variations in the resulting layer thicknesses. Single films 500 nm thick are measured with the Dektak IIA surface profilometer as the first check of layer thicknesses. The Dektak uses a sensitive needle that physically traverses the sample, preferably over an abrupt sample edge. Typically a small piece of the film is torn away from the substrate to expose such an edge, after which the challenge becomes finding an area along the edge that has not lifted from the substrate. Edge lifting leads to spurious inflated values of the thickness. The scan is always done from the substrate surface, up over the edge, then onto the sample. This way a lifted edge may be identified by its profile, shown in Figure 4.1.

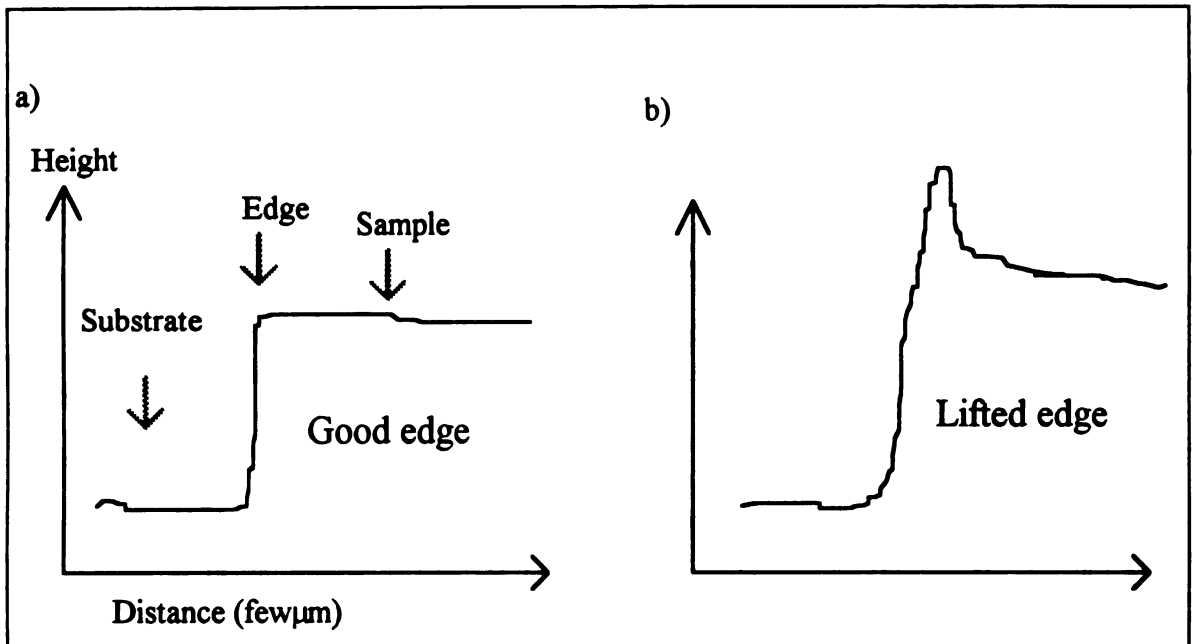

Figure 4.1 Schematic of Dektak profiles of a) sample edge secured to substrate b) sample edge lifted from substrate.

The standard used for calibration of this instrument is only given to an accuracy of 5% (unfortunate, since the precision of the Dektak when measuring the standard is better than 5%). Averages from films of each material gave their nominal thickness values to within 5%, with a standard deviation of ≤ 5 %. An exception was found for $Ag_{0.91}Mn_{0.09}$ in the AgMn/Si series, where the AgMn thickness was ~ 10% low for both films. This discrepancy was also noticed in the analysis of Section 4.3.4, and W_{SG} was adjusted before analyzing the magnetic data. Layer thicknesses used in Chapter 6 are to be considered as having an uncertainty ± 5% to reflect the spread of thickness values found for sputtered films.

NiMn, which was not suitable for edge production due to the hardness of the material, was not measured with this method.

4.3 X-ray Diffraction

4.3.1 Diffractometer and Sample Alignment

θ -2θ x-ray diffraction was used on all samples to determine layer thicknesses, size and crystallographic orientation of crystallites, and to give some estimate of layer quality in the multilayers. The diffractometer used was a Rigaku powder x-ray diffractometer with rotating Cu anode. Between the sample and the x-ray detector a graphite monochrometer screens out all but the Cu-K_α radiation, wavelength 0.1542 nm. A divergence angle of 1/6° for the x-ray beam was selected by inserting appropriate collimating slits, one between source and sample and one between sample and monochrometer. The fixed θ-2θ orientation of the diffractometer (see Figure 4.1) ensures that only periodicities perpendicular to the sample holding surface can fulfill the Bragg condition for an interference maximum

$$l\lambda = 2d\sin\theta. \qquad \text{Equation. 4.1}$$

Here l is the order number, λ the x-ray radiation wavelength, and d the spacing producing the maximum at θ. Since the bilayer periodicity Λ (Figure 4.2) is of interest in the multilayered samples, it is necessary to carefully line up the surface of the sample so the layers make angle θ with the incident and reflected beam. Since the reflection peak could be as narrow as $2\theta \sim 0.2^\circ$ for a well layered sample, if the sample is tilted more than 0.2° from the desired plane the peak may be missed. If the sample is tilted less than the peak width, the detector will still pick up part of the peak (see Figure. 4.3).

this page blank

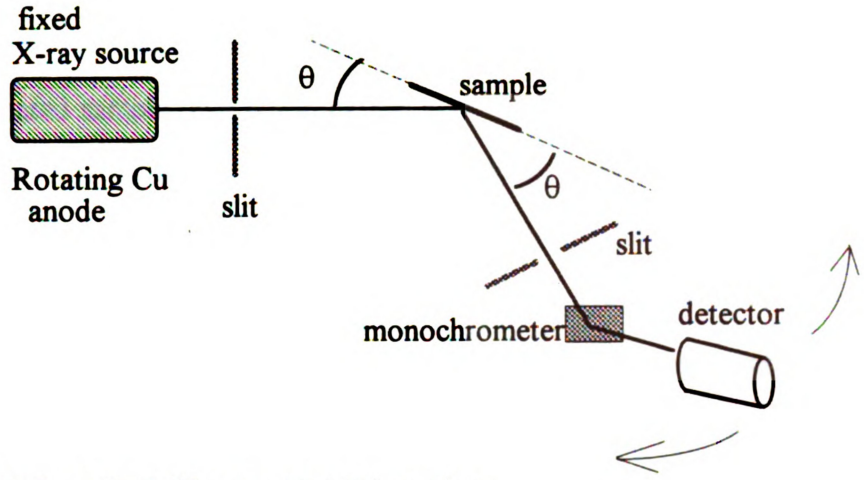

Figure 4.2 Powder Diffractometer Orientation

Figure 4.3 Periodicities in a multilayer sample

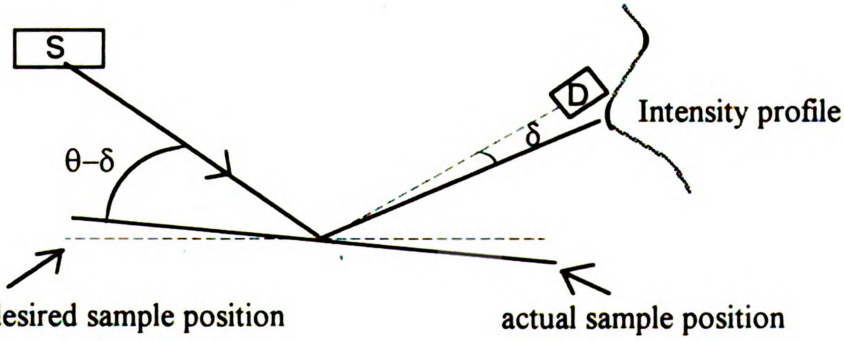

Figure. 4.4 The effect of sample misalignment by small angle δ.

The diffractometer is meant to hold a powdered sample, where the nature of the random mixture allows every crystallographic orientation to be viewed. There is no sophisticated sample orientation device like those found in single crystal diffractometers. To achieve the necessary alignment, the samples were mounted on an aluminum holder specially made by the machine shop in the MSU Physics Dept. to fit the Rigaku diffractometer and hold the sample face in position. The highest precision milling available to make the holders is ± 0.025 mm at each sample corner, introducing error in the alignment of the sample surface of up to ± 0.1°. This small misalignment can result in reduced peak height, and also a shift of peak location of $2\theta \sim 0.1^{o}$.

4.3.2 Texture Analysis

The first striking observation in the large angle region of $2\theta = 35 - 45^{o}$ is the usual presence of only one Bragg peak per material, whether multilayer or thick film. If the sample were a distribution of randomly oriented crystallites, a powder type pattern would be observed, showing peaks for all allowed Bragg reflections. The sputtered metal, however, while resembling a powder with its polycrystalline nature, is highly textured with only one orientation lying parallel to the sample surface; the <111> for fcc metals and the <110> for bcc. (The only exception was a single film of Al, where a weak <200> peak was observed.) These orientations allow the densest packing of the sample from top to bottom as the atoms to settle into their lowest energy state during sputtering.

The location of the reflection indicates strains are present in the sample. Even for a thick film (500 - 1000 nm) the peak is shifted (generally to a lower value) a fraction of a degree in 2θ from it's predicted position for an annealed sample of the same material or alloy composition. This shift corresponds to an expanded lattice parameter of up to 0.5%. This is not unexpected for a polycrystalline film, where crystallite boundaries and defects in crystallite growth put strains on the structure.

The size of the crystallites may be estimated from the width of the reflection line, via Sherrer's formula[126]

$$s = \frac{\kappa\lambda}{\beta\cos\theta}$$

where s is the coherence length perpendicular to the plane, κ is a constant approximately equal to 1, λ is the x-ray wavelength, and β is the FWHM of the line in radians. When determining the actual FWHM, the limits in the instrumental resolution of the beam must be considered. Two effects contribute to the resolution, the first is related to the collimating slits used in the system, the second arises from the separation of the Cu $K_{\alpha 1}$ and $K_{\alpha 2}$ lines, which are too close in wavelength to be separated by the monochrometer. At the region of interest (2θ = 35-45°) the apparatus adds an instrumental line width of $2\theta \sim 0.1^{o}$. None of the samples studied had a linewidth this narrow. In order to compensate for this effect, the instrumental linewidth was subtracted from the measured FWHM in a gaussian fashion $\beta = \sqrt{FWHM^2 - 0.1^2}$. The results are shown in table 4.1.

Table 4.1 Typical sputtered 2θ and ξ values for each material

Material	*d* Annealed Value[127] (nm)	*d* Sputtered Value (nm)	ξ - Coherence Length (nm)
Cu <111>	0.2088	0.2092	62.0
Ag <111>	0.2359	0.2365	114.0
Au <111>	0.2355	0.2359	37.0
Al <111> <200>	0.2338 0.2024	0.2343 0.2028	59.6 62.9
V <110>	0.2141	0.2137	29.2
Mo <110>	0.2225	0.2235	
Si	----------	amorphous	----------
CuMn <111> 10, 11, 12 % Mn	0.2113-0.2112	0.2116-0.2112	26.7 - 37.5
$Ag_{0.91}Mn_{0.09}$ <111>	0.3609	0.2369	50.9
$Au_{0.97}Fe_{0.03}$ <111>	0.2355	0.2363-0.2359	21.3 - 27.6
$Ni_{0.71}Mn_{0.29}$ <111>	0.2091	0.2075-0.2072	36.3 - 38.0
$Ni_{0.69}Mn_{0.31}$ <111>	0.2096	0.2084-0.2082	40.7 - 41.5

Extracting information from the Bragg peaks becomes considerably more complicated when looking at multilayers. Neighboring materials add additional strain to each other and so induce shifts in both peak locations, and cause broadening as the layer thickness limits the size of the crystallites. Satellites due to the periodicity Λ appear around and between the peaks, making line width analysis impossible in all but one case, the SG/amorphous Si samples. In these samples the Bragg peak of the metallic SG showed a width corresponding to a coherence length equal to that of the SG layer thickness to within a few nanometers.

4.3.4 Determination of the Bilayer, Λ

The multilayered samples contain typically 50 - 200 bilayers, depending on the value of W_{SG}. The bilayer number is chosen so that the total SG thickness is 100 - 500 nm, in order to provide suitable magnetic signal strength. The bilayer thickness, Λ, is the only true periodicity of a multilayer, and is capable of producing Bragg reflections (substitute Λ for *d* in Equation 4.1). Since Λ is large (4 - 30 nm), the 2θ reflections for this periodicity occur at small angles. Although the reflection from higher orders of *l* decrease in intensity with increasing θ, a reflections from Λ are also observed in the vicinity of the material lattice parameter reflections at large angles (see Section 4.3.6 for a model of this behavior). These will be referred to as large angle satellites.

The Bragg equation stated above is actually a simplified version neglecting the index of refraction. This neglect is normally valid, as the index of refraction for x-rays in metals is $n = 1 - \delta$ where δ is small and positive, and may be calculated from the expression

$$\delta = \lambda^2 \frac{r_e n}{2\pi}[f + \Delta f' + \Delta f''].$$

Here λ is the x-ray wavelength, r_e is the classical electron radius, and n is the atomic number density. f is the atomic form factor, with $\Delta f'$ and $\Delta f''$ its real and imaginary corrections due to absorption edges. For most metals this value is $\sim 10^{-6}$. The following shows that neglecting this small change is acceptable for large angles, but not for $\theta \leq \sim$ few degrees.

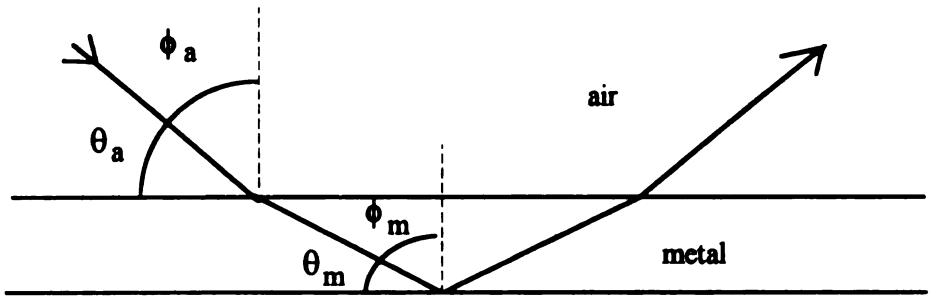

Figure 4.5 Exaggerated x-ray deflection due to index of refraction

From the above Figure, the angle considered in Bragg's Law is actually θ_m, but the measured angle is θ_a. To find the relation between the two, use Snell's Law

$$n_a \sin\phi_a = n_m \sin\phi_m$$

since $n_a = 1$, $n_m = 1 - \delta$, and $\sin\phi = \cos\theta$, we get

$$\cos\theta_a = (1-\delta)\cos\theta_m$$

Considering that δ is small ($\sim 10^{-4}$), and $\sin^2 + \cos^2 = 1$,

$$\sin^2\theta_a = \sin^2\theta_m + 2\delta$$

Thus replacing this expression for $\sin\theta_a$ in Bragg's Law yields

$$(2\Lambda)^2 \sin^2\theta = (l\lambda)^2 + 2\delta \qquad \text{Equation. 4.2}$$

where Λ is the bilayer thickness. For large θ, δ is so small as to be negligible and Equation. 4.2 reduces to its simpler form of Equation 4.1. But for a periodicity the size of a typical bilayer, the reflections occur at small enough θ ($\sim 1^o$) that it is necessary to include the 2δ term. To determine Λ to the greatest possible accuracy it is desirable to

compile the measurements for multiple orders of l. Plotting $sin^2\theta$ vs. l^2 for several reflections allows Λ to be extracted from a least squares fit of the slope of the line. An average δ may be extracted from the intercept, but the value lacks both accuracy and precision, because our instrument and the sample holder are unable to meet the stringent alignment conditions required to successfully carry out such an analysis[128]. It is necessary in this analysis to use the correct values for l, where $l = 1$ is the first reflection after $2\theta = 0$. Typically this reflection is at so low an angle that the first observed peak is $l = 2$ or 3. Choosing improper l values is signaled by a curve rather than a line in the $sin^2\theta$ vs. l^2 plot.

A similar analysis is done with Large angle satellite reflections, but δ may be neglected. Using Bragg's Law in Equation 4.1, only $sin\theta$ vs. l need be plotted, so the choice of starting l value is irrelevant, as long as the ls are consecutive with the peaks.

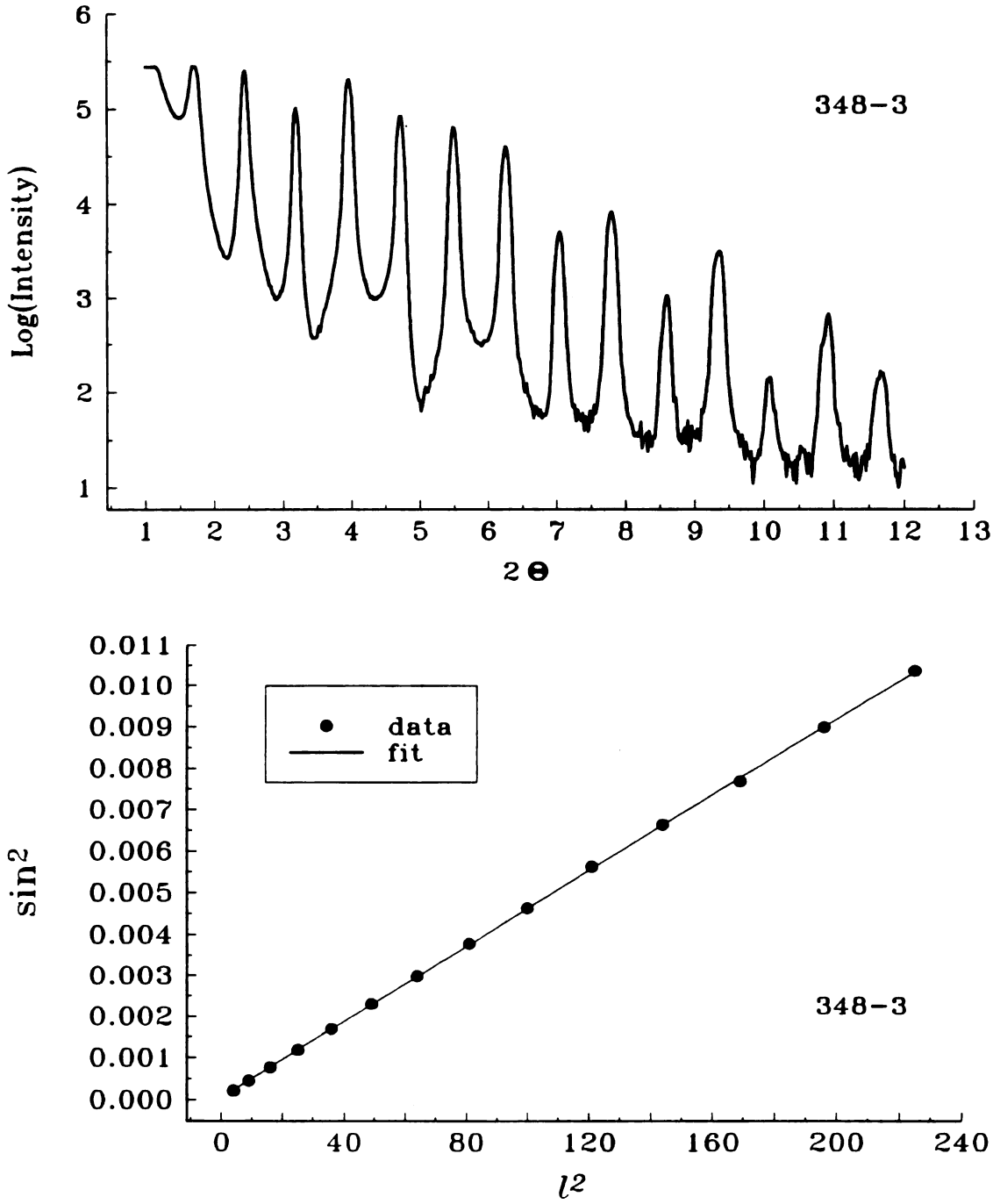

Figure 4.6 Small angle diffraction scan and bilayer analysis (Λ=14nm) for an AuFe/Si 7nm / 7nm sample.

4.3.5 Series Analysis

Although any one sample will give only the bilayer thickness, Λ, a series of samples with one bilayer component held fixed will reveal whether systematic or random errors exist in the thicknesses of each component. First assume the actual thickness of each material may be different from the expected thickness by a linear factor, as would occur for a low or high film thickness monitor reading during sputtering. If we define:

W_{SG}, W_{IL}, Λ = actual SG, IL, and bilayer thicknesses

W_{SGN}, W_{ILN}, Λ_N = nominal SG, IL, and bilayer thicknesses

$W_{SG} = c\,(W_{SGN})$ $\qquad$ $W_{IL} = d\,(W_{ILN})$

then the bilayer Λ may be rewritten as:

$$\Lambda = W_{SG} + W_{IL} = c(W_{SGN}) + d(W_{ILN})$$

$$\Lambda_N = W_{ILN} + W_{SGN}$$

$$\Lambda = d(W_{IL}) + c(\Lambda_N - W_{IL})$$

$$\Lambda = c(\Lambda_N) + W_{ILN}(d - c)$$

If W_{ILN} is constant (usually 30 nm), then plotting Λ vs. Λ_N gives values for *c* and *d*. A similar expression may be found for constant W_{SGN}. A perfect set of samples will give a straight line of slope 1 and intercept 0, which is often nearly the case. Fluctuations in the layer thicknesses appear as noise. Since the samples are never sputtered in an order relating to their thicknesses, any drift in the rate during the run would also appear as noise in this plot. Figure 4.7 shows a typical line produced by this method.

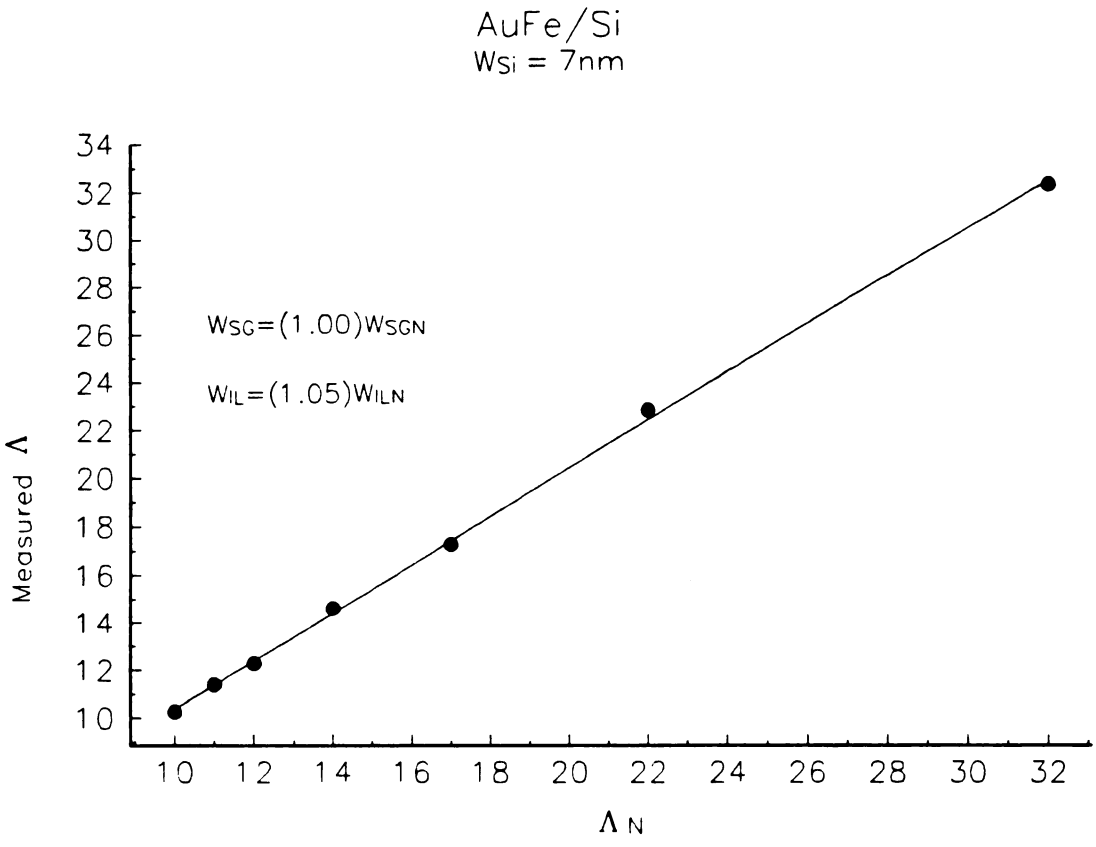

Figure 4.7 A typical plot for individual thickness calculations

The AgMn/Si series gave the only line with significant deviation from experiment. The AgMn/Si slope was 0.87, indicating that the AgMn layers were 13% thinner than expected, a value supported by the results in Section 4.2.

4.3.6 Step Model for Λ Reflections

As indicated above, there are three periodicities in the sample, bilayer Λ and lattice spacing for each non-amorphous material, $d_{material}$. The three periodicities cannot be viewed as independent, as the larger is made from layers of the smaller. A simple, one dimensional step model, proposed by Segmuller and Blakeslee[129], can help to qualitatively understand the relationships.

In this model, each layer is assumed to have an integer number of atomic planes having the same lattice constant as in the bulk material. The structure factor, S(q), is found by summing the contributions from each part of the multilayer:

$$S(q) = \frac{\sin(N\Lambda q/2)}{\sin(\Lambda q/2)}\left\{ f_1 \frac{\sin(n_1 a_1 q/2)}{\sin(a_1 q/2)} + f_2 \frac{\sin(n_2 a_2 q/2)}{\sin(a_2 q/2)} \exp(i\Lambda q/2) \right\}$$

Thus the diffracted intensity is S*S,

$$I \sim \frac{\sin^2(N\Lambda q/2)}{\sin^2(\Lambda q/2)}\left\{ f_1^{\,2} \frac{\sin^2(n_1 a_1 q/2)}{\sin^2(a_1 q/2)} + f_2^{\,2} \frac{\sin^2(n_2 a_2 q/2)}{\sin^2(a_2 q/2)} + 2 f_1 f_2 \frac{\sin(n_1 a_1 q/2)}{\sin(a_1 q/2)} \frac{\sin(n_2 a_2 q/2)}{\sin(a_2 q/2)} \cos(\Lambda q/2) \right\} . \qquad \text{Equation 4.2}$$

Here N is the number of bilayers, $q = \sin\theta/\lambda$ is momentum transfer, λ is the x-ray wave length, and f_1 and f_2 are the atomic scattering factors for materials 1 and 2. Only one

lattice parameter is used per material, since the samples are all highly textured, with only one orientation parallel to the sample surface (see section 4.3.2).

The term $sin^2(\Lambda q/2)$ has zeros at $q = l\pi/2\Lambda$, producing maxima corresponding to the reflections from Λ. Successive orders of l produce peaks starting at zero and reoccurring every 2θ = 0.5 to ~ few degrees. The heights of these peaks are modulated by the terms inside the curly brackets. The atomic form factors, f_i, contain the DeBye-Waller factor, $exp\left(\frac{-B\sin^2\theta}{\lambda}\right)$, which exponentially attenuates the intensity as θ increases. As a result the multiple order reflection at low angles from Λ decrease in height and generally disappear by 2θ = 10°. The intensity decrease is not smooth however; the faster oscillations occurring from the numerators of the enclosed terms, $sin^2(n_i a_i q/2)$, modulate the intensity in a potentially complex manner. A simplification may be used for the SG/Si samples, where the form factor for the light Si is so small f_{Si} may be set to zero. Equation. 4.2 then becomes

$$I \sim \frac{\sin^2(N\Lambda q/2)}{\sin^2(\Lambda q/2)}\left\{ f_{SG}{}^2 \frac{\sin^2(n_{SG}a_{SG}q/2)}{\sin^2(a_{SG}q/2)} \right\}.$$

An envelope of period related to $n_{SG}a_{SG}$ is superimposed on the Λ maxima. An example of this effect is shown in Figure 4.6. If the minima of this envelope could be accurately determined, a value for the thickness of the SG layer could be calculated.

The denominators of the enclosed terms, with their small arguments, oscillate slowly with increasing q, and do not become zero (thus producing a maximum) until 2θ reaches about 40°. These zeros occur at $q_i = \frac{\lambda}{2a_i}$, producing the first order maxima from each material's lattice parameter. Superimposed upon these two maxima (or maximum if a-Si is the second material) are the oscillations from the Λ reflections, and less noticeably the oscillations from the numerators of the enclosed terms. If one or both

layers of materials are thin enough, their lattice parameters come together and only one main peak is seen, with satellites on each side from the Λ reflections. Figure 4.8 shows two examples of high angle satellites. This scenario repeats itself in the region of the second order maxima of the material lattice parameters.

The step model considers only a perfect sample. Features in the sample such as layer thickness fluctuations, layer boundary mixing, and layer roughness, all affect the x-ray profile. These effects are discussed further in Section 4.3.7.

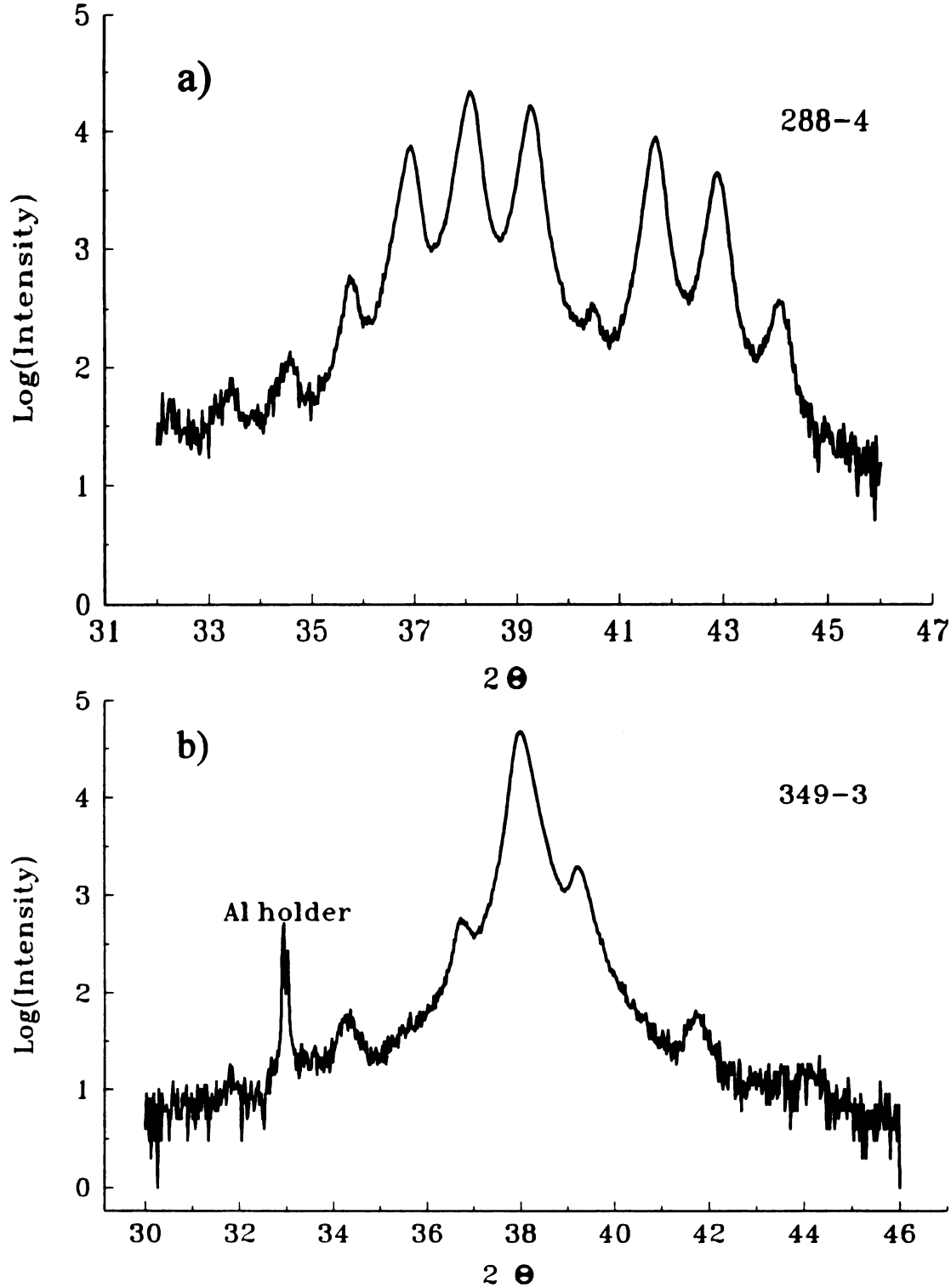

Figure 4.8 Large angle x-ray scans for a) CuMn/Au 4nm/4nm where a_1 is significantly different from a_2 b) AuFe 4nm/4nm where $a_1 \sim a_2$.

4.3.7 Estimating Quality of Layers from X-ray Diffraction

An x-ray diffraction scan of a multilayer showing numerous peaks is a good indication that the sample is layered. But a scan with modest peaks may not mean the sample is poorly layered, it may be the unavoidable result of the material choice in the multilayers. Understanding a general set of rules for diffraction behavior at low and high angles can help explain features of a scan. To determine quantitative values of parameters, such as interface mixing or layer roughness, requires comparison of scans to mathematical models.

In general, Equation 3.2 indicates that the prominence of the peaks at small angle (small q) will be determined by the contrast between the scattering factors of the two materials composing the multilayer. Thus a scan for a CuMn/Au sample should display better peak structure than that of a CuMn/Al multilayer for otherwise equal samples. Other effects however tend to affect the small angle spectra more. Most notably of import is the type of roughness at the interfaces. Small angle scans are extremely sensitive to the long range flatness of the layers. A sample with a cross sectional appearance of Figure 4.9 will have poorly defined low angle diffraction peaks because the x-ray incident at low angles samples a broader area. Such a sample may exhibit beautiful large angle structure, where it is flat on the small horizontal length scale of high angle sampling. This behavior is observed in the case of columnar growth, where some structural coherency exists between crystallites of adjoining layers, resulting in a profile of cumulative interface roughness as shown in Figure 4.9. Thus the spectacular small angle scans observed for a SG/Si multilayers (e.g. see Figure 4.6) are due not only to the high scattering factor contrast, but also to the long scale layer flatness imposed by using an amorphous IL incapable of contributing to cumulative roughness.

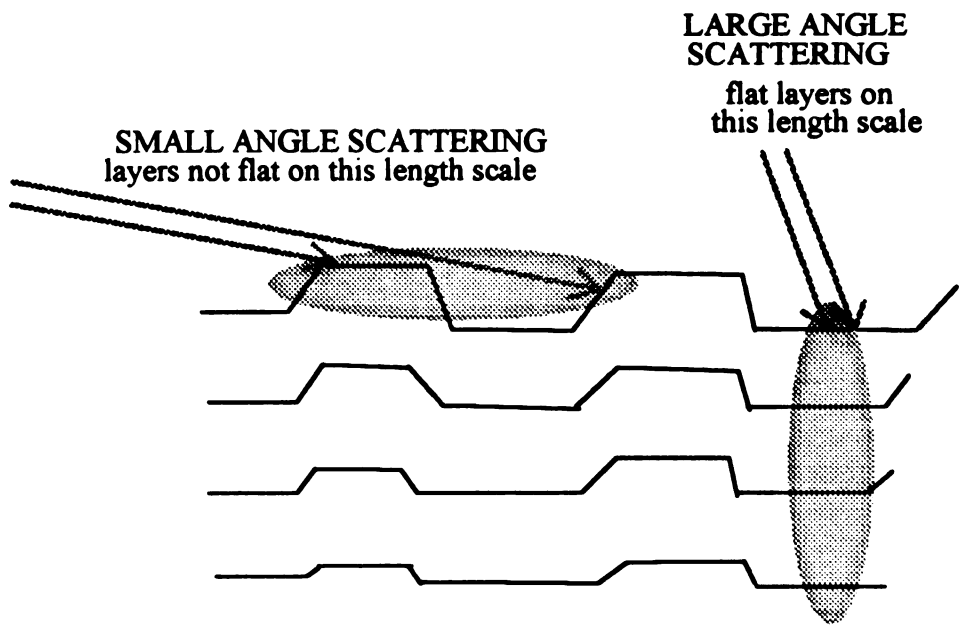

Figure 4.9 Length scales sampled by small and large angle x-ray diffraction beam.

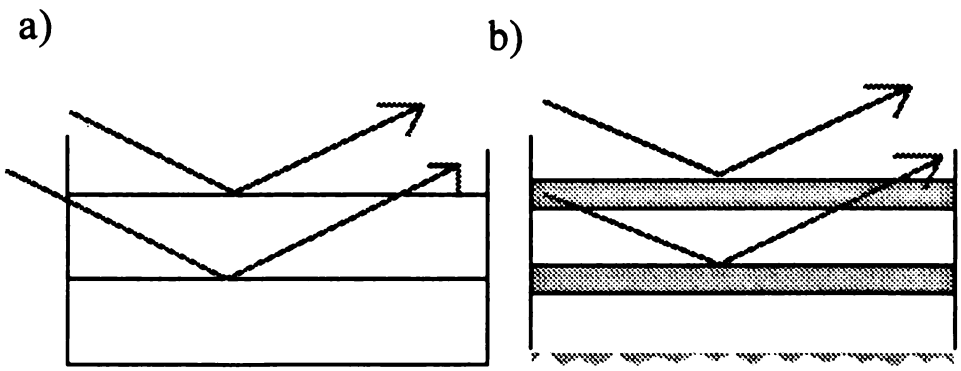

Figure 4.10 Small angle x-ray behavior on unmixed and flat mixed interfaces.

Interface mixing on the other hand will not dampen the small angle peaks if the layers and the mixed area are very flat. Thus Figures 4.10 a) and b) will give virtually the same small angle spectra for the same materials since the mixed region forming the new "layer" has the same periodicity as the unmixed layers.

The above ideas can aid in analyzing a series of multilayers where the materials are the same but the layer thicknesses vary. Figure 4.11 shows small angle scans for the CuMn/Al system as W_{Al} is decreased. The sharp multiple peaks indicate that the layers are quite flat, not columnar, and do not become columnar even when even at W_{Al} = 0.5 nm (~ 2 ML).

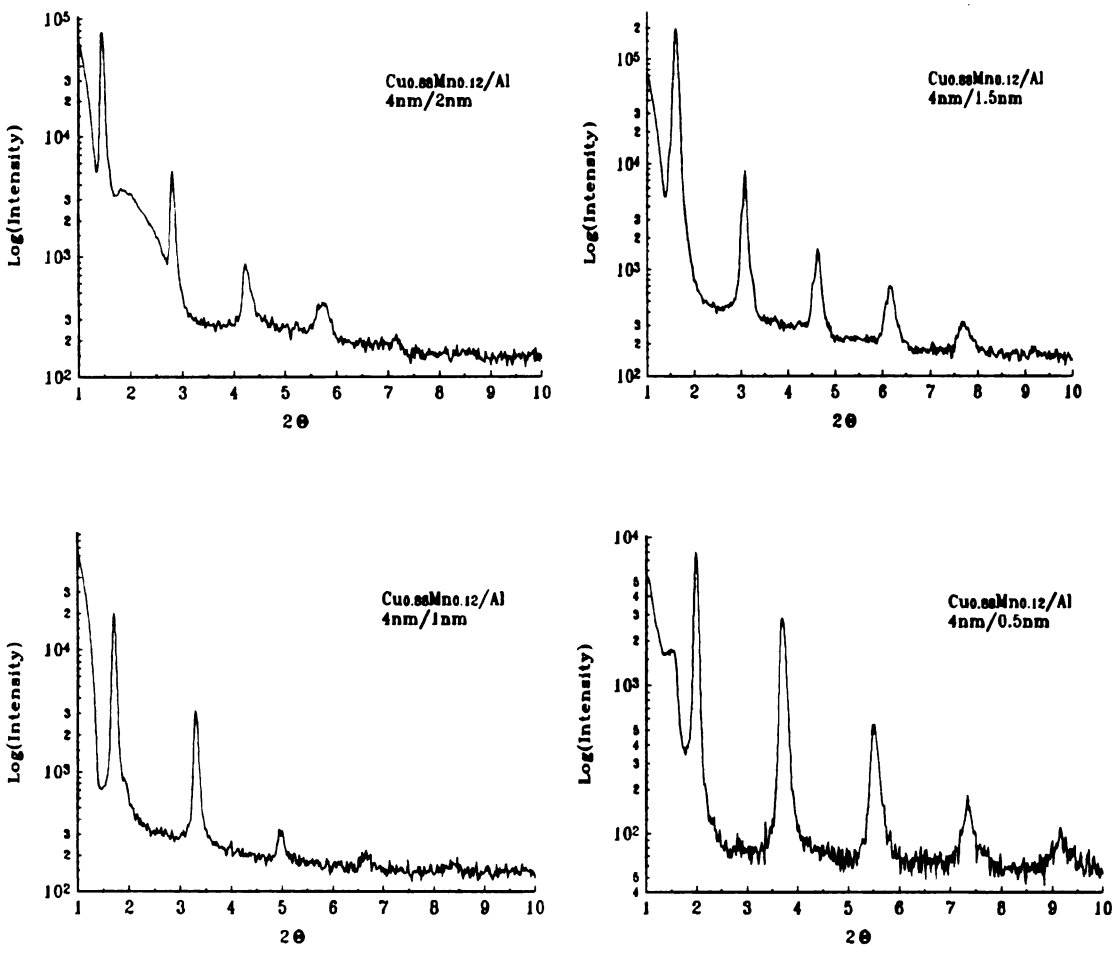

Figure 4.11 CuMn/Al x-ray scans for decreasing Al thickness.

Large angle (large q) scattering is subject to different effects. For large q, the intensity height of the satellites is strongly affected by the contrast in the lattice spacings d_1 and d_2. This effect is demonstrated by Figure 4.8, where a) shows CuMn/Au where d1 ≠d2 , and b) shows AuFe/Ag, where $d_1 \sim d_2$.

Neerinck et. al. determined, through modifying the step model and calculating resultant intensities, that large angle satellite reflections can be entirely wiped out by a small amount of a particular type of multilayer imperfection, *continuous fluctuation* of a layer thickness, on the order of ~ few Angstroms (independent of the layer thickness).[130] Multilayers with two crystalline components can only present *discrete roughness*; the variation in a layer thickness is limited to integral steps of the lattice parameter. An amorphous layer however may possess a continuous distribution of thicknesses. Figure 4.12 shows AuFe/Si, which not only lacks a material lattice parameter peak from the second material (Si), but is missing the bilayer periodicity satellites, leaving only the oscillations from the thickness of the SG layer. All the SG/Si systems with $W_{Si} > 0.5$ nm (see Section 4.4) lacked large angle satellites, indicating that the Si layers are amorphous and fluctuate in thickness by at least several Angstroms.

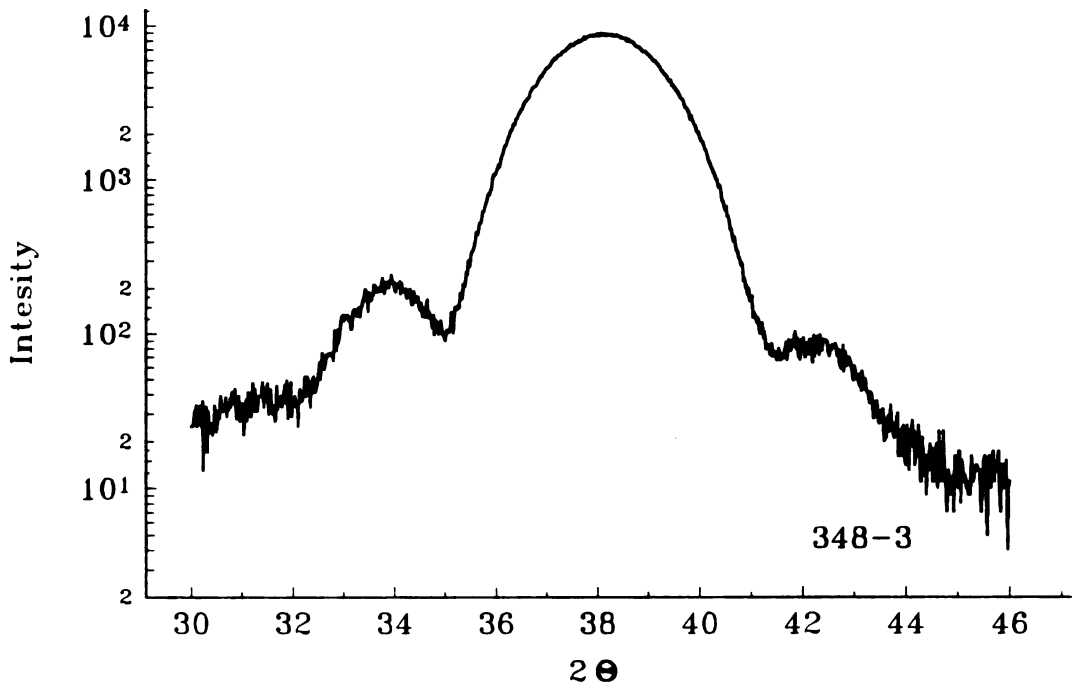

Figure. 4.12 Large angle scan of $Au_{0.97}Fe_{0.03}$/Si 4 nm/7 nm. Scan lacks Λ satellites, but shows thickness modulation.

4.4 Analysis of SG/Si multilayers

4.4.1 X-ray Analysis

Si sputters amorphous rather than crystalline layers, and so metal/Si systems require different structural considerations from those in metal/metal multilayers. As mentioned above, the amorphous nature produces flat, non-columnar layers, and continuous roughness that wipes out high angle satellites. We now address the issue of interface mixing and potential silicide formation.

Silicide formation at the interface between metals and Si has been observed for numerous metals, including Ni, Mo, Co, Cr, and Fe.[131,132,133] In Ni/Si multilayers, it was found that Si will diffuse into the Ni layer prior to silicide formation[131]. The light Si atom can diffuse without significantly changing the atomic density of the metal layer. Such behavior is found by Fullerton et. al.,[133] where Fe/Si multilayers with fixed W_{Fe} only slight changed Λ as W_{Si} was increased from 0 to 2 nm, after which Λ increased with the expected additive dependence (resulting in a Λ smaller than nominally sputtered). The authors concluded that the first 2 nm of Si diffused into the metal layer. Large angle diffraction data from the same study provided evidence for silicide formation in the diffused region. Large angle scans of multilayers with $W_{Si} \geq 2$ nm resembled that of Figure 4.12 , indicating an amorphous layer was present, while similar scans of samples with $W_{Si} \leq 1.5$ nm resembled Figure 4.8 b, indicating two crystalline layers with close lattice parameters. Since room temperature sputtered Si is not crystalline, the crystalline layer must be a silicide.

A few early CuMn/Si samples from this study also showed a smaller Λ than nominally sputtered. It was assumed at the time the discrepancy was due to the use of crystalline Si parameters to calibrate the FTM, and so to compensate, the FTM readings were reduced by 8% over what they would have been normally. For the SG/Si data where

W_{SG} is fixed, this addition of extra Si presents no problem in the magnetic data interpretation, since the Si acts only as a separator. For CuMn/Si coupling studies, W_{SG} held fixed W_{IL} thinned, the 8% is not large enough to qualitatively change conclusions from the magnetic data or the following structural results.

The small angle x-ray scans in Figure 4.14 show the progression in CuMn/Si multilayers as W_{Si} is decreased. A sudden breakdown occurs between W_{Si} = 3 and 2 nm, indicating that at 2 nm that the amorphous, flattening layer is no longer present. The large angle scans, however, indicate the presence of continuous roughness for $W_{Si} \geq 1$ nm (see Fig 4.15a). For $1 \leq W_{Si} \leq 2$ nm, the Si layer is such that cumulative roughness is allowed to grow, but the Si layer is not crystalline.

Figure 4.15b, the large angle scan for W_{Si} = 0.5 nm, shows a narrow peak with small satellites. This value of W_{Si} is much smaller than the silicide thickness of W_{Si} = 1.5 nm observed in the Fe/Si system discussed above. Our profile may indicate two things: a) the layer is no longer amorphous, as would be the case if a crystalline silicide is formed; b) the Si layer is still amorphous but is not thick enough to provide the ~ few Angstroms of continuous roughness needed to destroy the satellites (see Section 4.3.7).

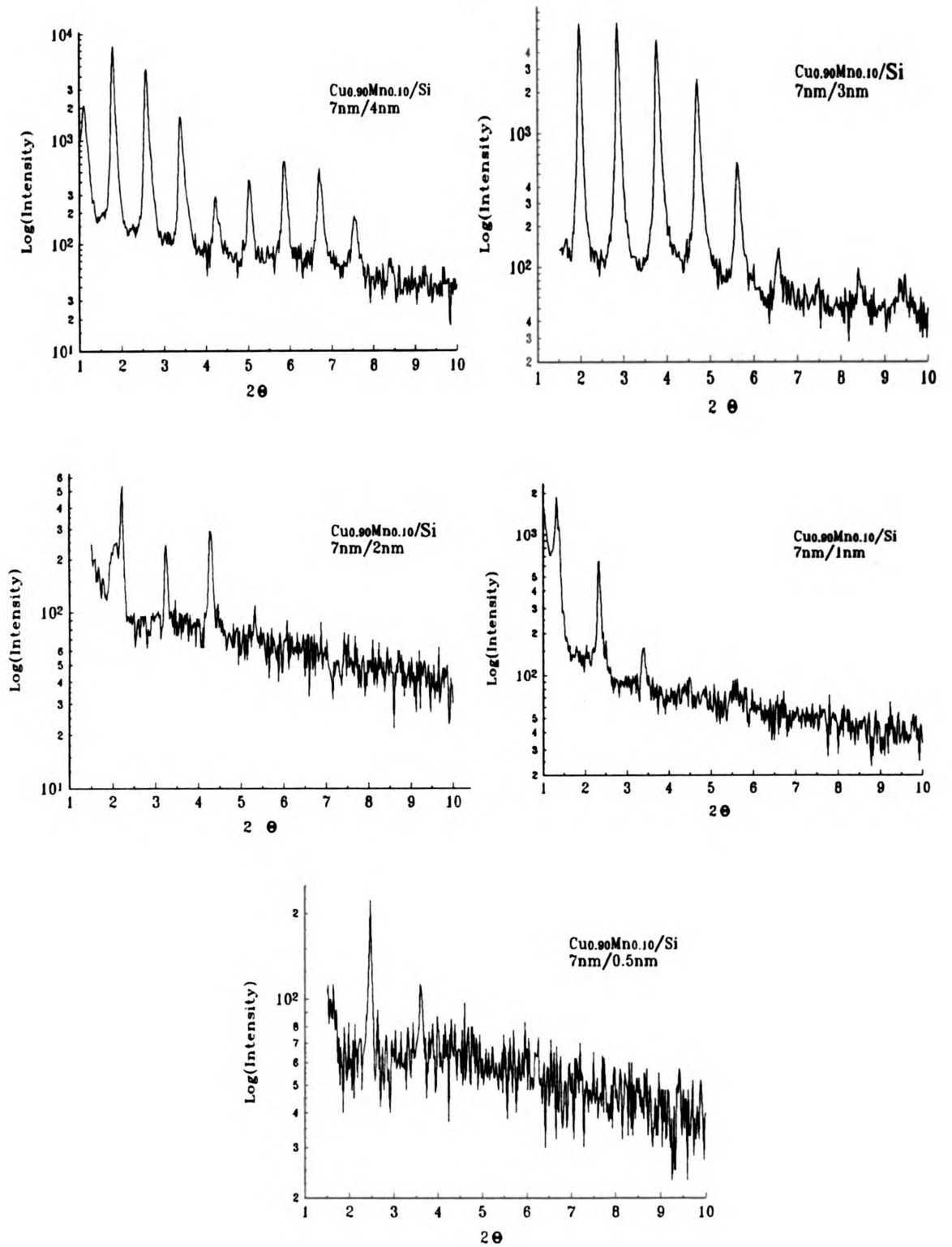

Figure 4.14 Small angle x-ray scans showing the degradation of CuMn/Si layering.

a)

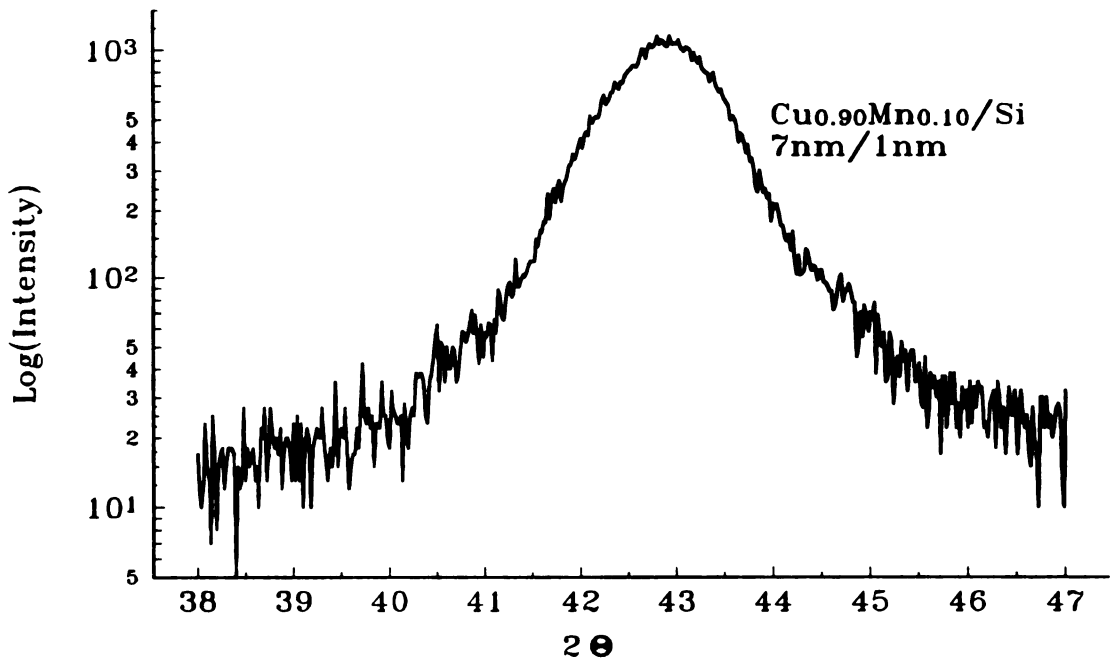

b)

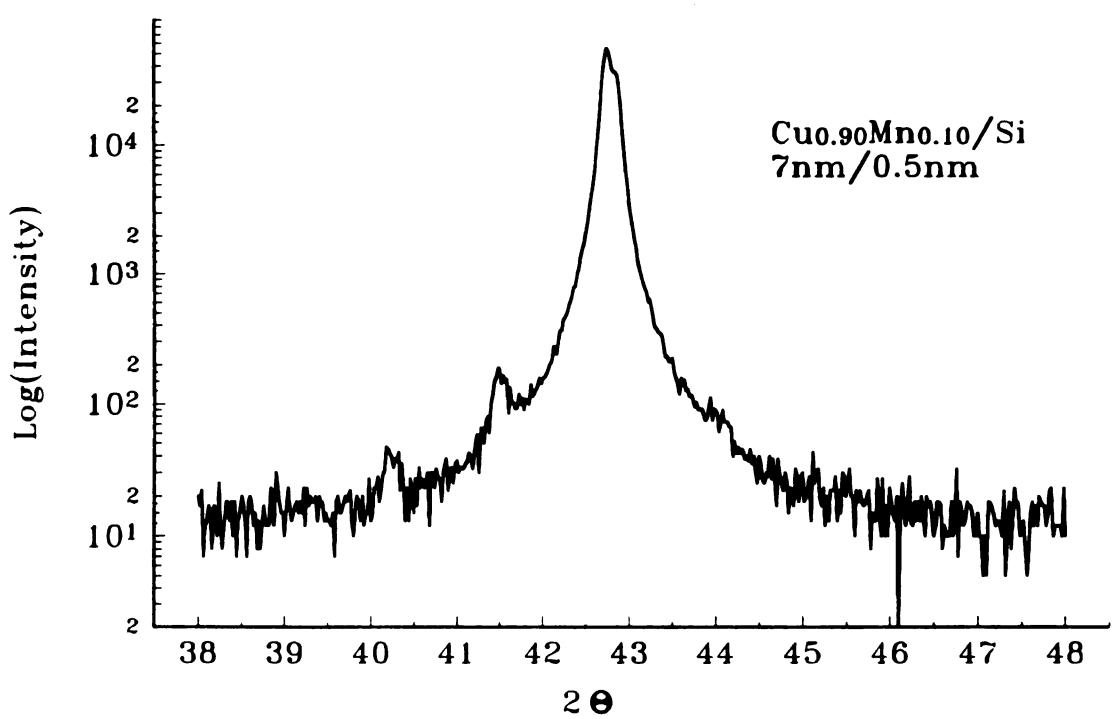

Figure 4.15 Large angle x-ray scans of CuMn/Si showing transition from a) one amorphous layer, to b) two crystalline layers.

4.4.2 Cross Sectional Analysis

In an effort to compare the structural quality of the three SG/Si systems, transmission electron microscopy (TEM) and electron diffraction were performed on cross sectional slices from three samples, $Cu_{0.88}Mn_{0.12}$/Si, $Ag_{0.91}Mn_{0.09}$/Si and $Au_{0.97}Fe_{0.03}$/Si, all 3 nm/7 nm. The samples were sliced with a 55° diamond knife, to an electron beam transparent thickness of ~ 70 nm. The TEM was performed at 200 and 120 keV with a beam current of 10 μA. All cross sectional preparation and imaging were done by D.A. Howell at the Dept. of Material Science and Mechanics at Michigan State University. For more details on this work, see reference 134.

The dark regions of the bright field images in Figure 4.16 correspond to the SGs, and the lighter layers the amorphous Si. The image cannot be used to determine actual layer thicknesses in the sample, because their relative ratio in the image is dependent on the thickness of the cross section when amorphous Si is present.[135] We can only state from these images that the SG/Si samples are well layered.

Electron diffraction operates under the same principles as x-ray diffraction. The orientation of the instrument with respect to the samples is, however, different. Whereas the x-ray diffractometer could only respond to periodicities perpendicular to the layer, transmission electron diffraction can only respond to in-plane periodicities. As with x-ray diffraction, the width of the rings indicate length of coherence. Sharp rings in the pattern denote large crystallites, the rings becoming broader as the crystallites get smaller. Bright spots in the pattern result from in-plane orientation of crystallites. The electron diffraction patterns in Figure 4.17 for the three samples reveal some differences between them. The AgMn layer shows the most crystallinity with a narrow ring and the addition of

bright diffraction spots, while the AuFe layer gives only a diffuse ring, indicating the least crystallinity CuMn lies somewhere between these two.

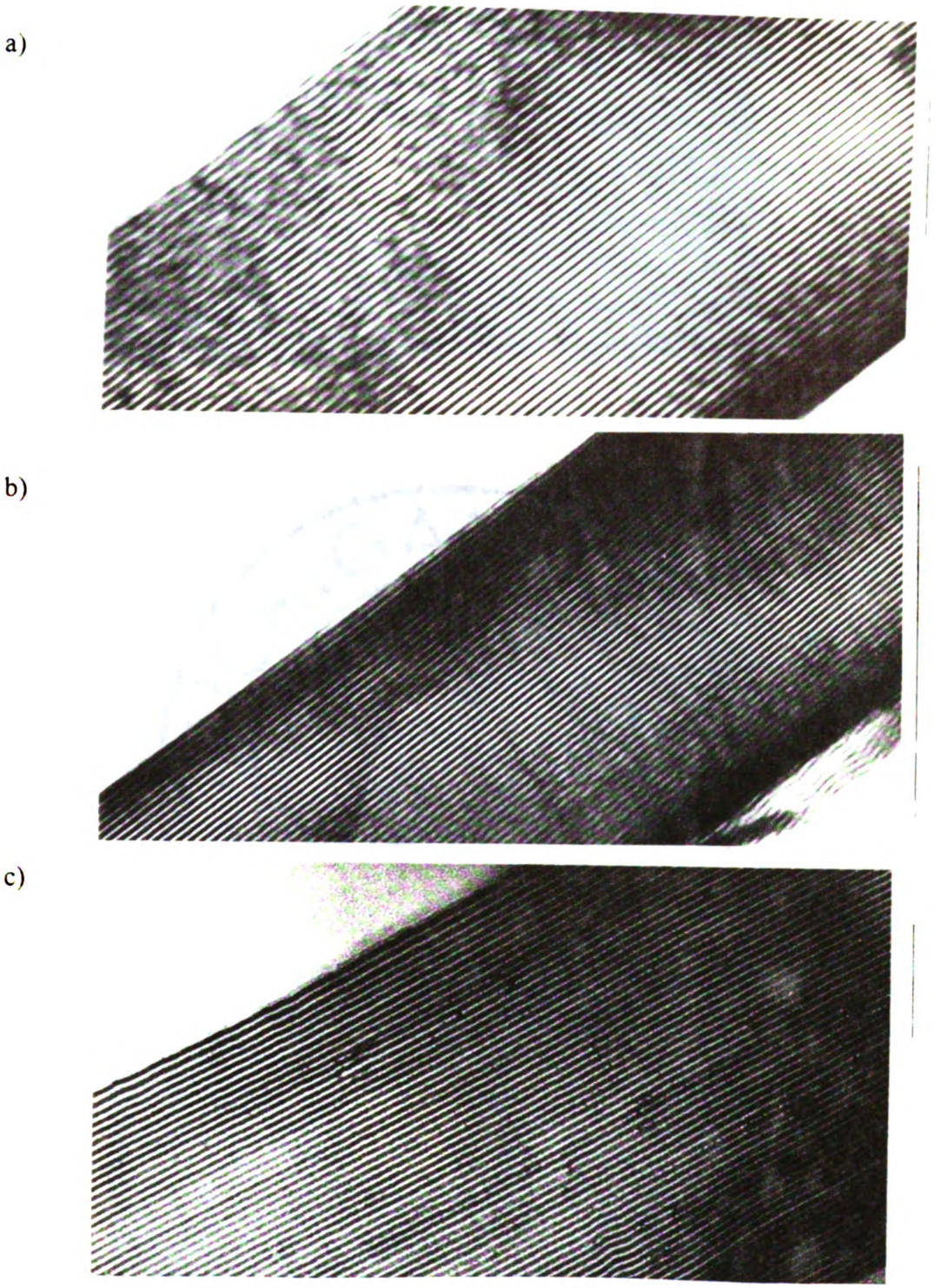

Figure 4.16 TEM images of cross sections of 3 nm/7 nm of a) $Ag_{0.91}Mn_{0.09}/Si$, b) $Cu_{0.88}Mn_{0.12}/Si$ and c) $Au_{0.97}Fe_{0.03}/Si$.

a)

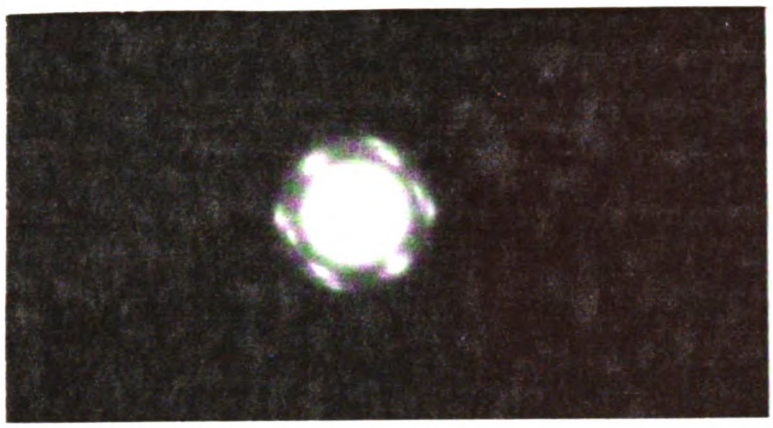

b)

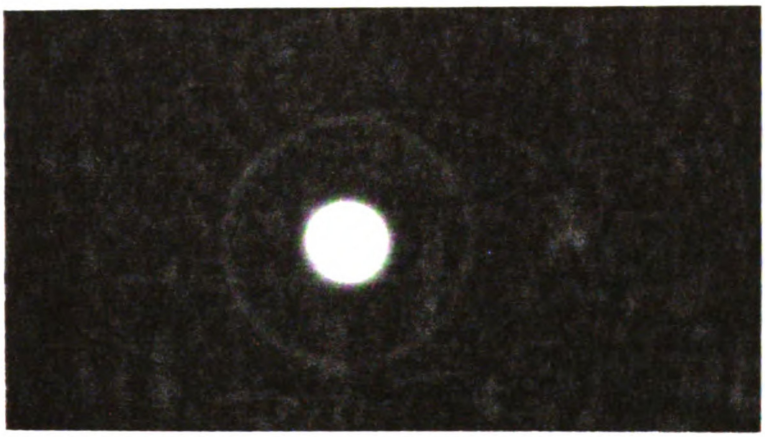

c)

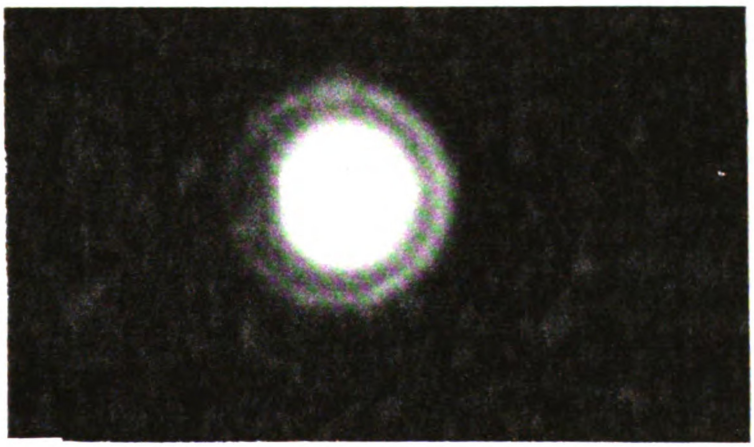

Figure 4.17 Electron diffraction patterns from the samples shown in Figure 4.16.

CHAPTER 5

EXPERIMENTAL PROCEDURES

5.1 Magnetic Measurements

Magnetic measurements were made on one of two commercial SQUID based magnetometers made by Quantum Design Inc. Two types of measurements were possible; static, where a static field is applied and the sample is pulled through three counter-wound pickup coils (see Figure 5.1), and a.c., where the measuring field is a small (< 5G) oscillating sine wave, with or without a supplementary static field. The a.c. measurements require the sample to be stationary and located inside and in-plane with one of the pickup coils. The response of the sample is also a sine wave, but in general lags the input. The response signal may be separated into in-phase and out-of-phase components, referred to as real and imaginary susceptibilities. A non-zero imaginary component indicates energy losses in the sample. The imaginary part of the susceptibility can give valuable information about the SG freezing process, since the frequency dependence of the SG transition implies an intrinsic loss in the material[136]. The behavior of the real part is similar to that seen in the static measurement, but where the static measurement is done on a time scale of ~ few minutes per point, the measuring time in the a.c. susceptibility is much shorter (see Section 1.3). All a.c. susceptibilities in this project were taken at a measuring frequency of 16 Hz, or 0.06s measuring time. This study focuses on the static magnetization and the real part of the a.c. susceptibility.

The majority of measurements were made on the older of the two SQUIDs, which had only static field capabilities. This machine had a temperature range of 1.8 K to 350 (?) K, and a sensitivity of ~ 10^{-8} emu (cgs units). 200 - 500 nm of total SG (50 to 300 layers, depending on the SG layer thickness) was needed to deliver a signal in the 10^{-6} emu range for a good signal to noise ratio. The residual field in the magnet after a magnet quenching procedure was typically 5-7 G. The quenching was accomplished by setting the magnet to the largest available field, 50,000 G, and oscillating towards zero using typically about 10 fields; e.g. 50,000, -30,000, 10,000, -5000, etc.

The newer machine had both static and a.c. capabilities, with the same sensitivity and temperature range. It also possessed a low field option, which allowed reduction of the residual field to < 0.1 G after quenching. Most static measurements were taken with a measuring field of 100 G, and the difference in the residual field between the two machines did not affect the measured value of the transition temperature.

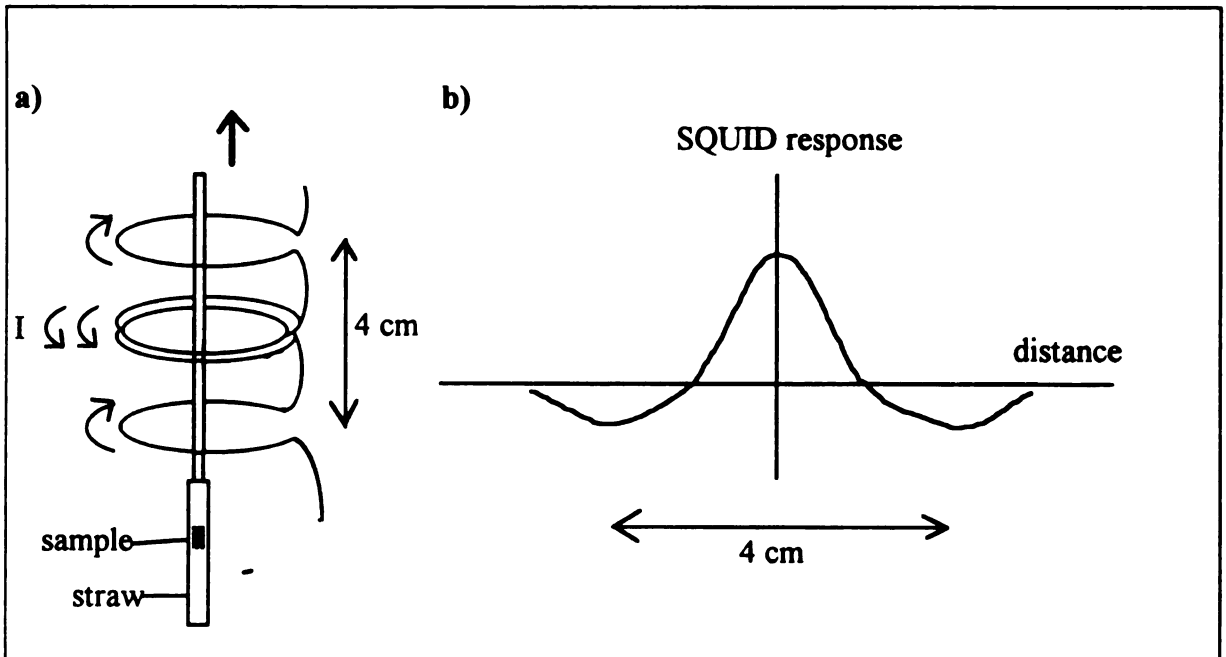

Figure 5.1 a) SQUID pickup coil and sample configuration, and b) resulting signal

The sample was mounted in a soda straw secured to the brass nonmagnetic 12" tip of a long hollow stainless steel rod. The 0.5 x 0.5 " substrate had to be broken in half to fit into the straw, and was held in place in the vertical plane by either a small amount of plastic or cotton thread sewn through the straw, both materials having negligible signal in the amounts used. To enter the measuring chamber, an evacuated narrow dewar containing the pickup coils, thermocouple, and temperature controlling heating elements, the sample must first pass through an air lock which is flushed with ^{4}He boil off and evacuated. Once the sample is lowered to its proper position, the top of the measuring rod is attached to a stepping motor so the sample may be moved up and down for measurement. The vacuum integrity is assured by two knife edge seals in the airlock plug (see Figure 5.2). If these seals are damaged, oxygen (and other gasses) will leak into the measuring chamber. Oxygen is a particular problem for the weakly magnetic SG system, as liquid oxygen has a strong susceptibility of 7699 emu/gram below its boiling point of 90.1 K and a peak of 10,200 emu/gram at its melting temperature of 54.3 K.[137] A leak in the system could allow oxygen to enter as a gas at the top of the tube, and condense or freeze on the sample. For this reason particular care was taken to slide the measuring rod slowly through the seal, allowing the rod to warm to room temperature so it does not cool the o-rings and make them brittle.

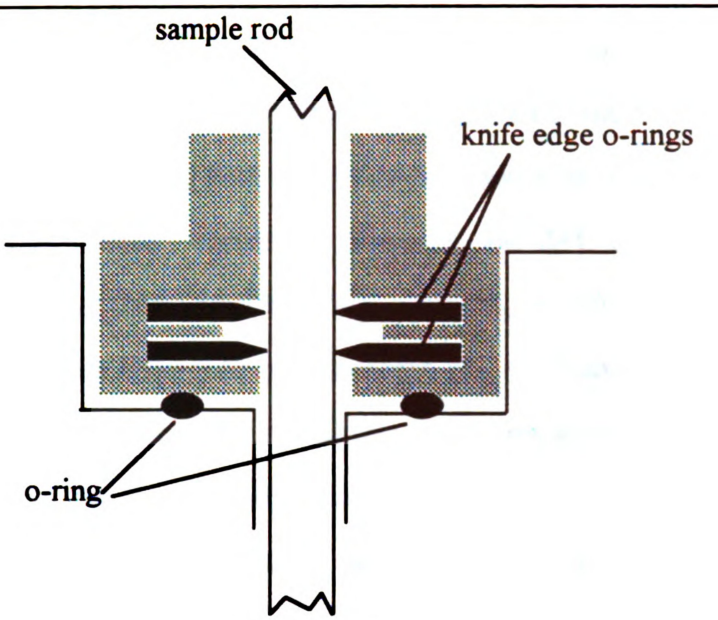

Figure 5.2 Sample rod seal to the magnetometer

5.2 Determination of T_f

Magnetization vs. temperature curves were taken for all multilayered samples. The value for T_f is extracted from the zero field cooled (ZFC) curve, where the sample is cooled from a temperature $T \geq 2T_f$ to a temperature $T << T_f$, where a small measuring field, typically 100G, is then applied. As the temperature is increased, a peak in the magnetization appears, the temperature of which is defined as T_f. Rounding of the ZFC peak limits the determination of T_f to $\pm$ 0.5K in most cases. The sample displays different behavior when field cooled (FC) from above T_f to below T_f. Below T_f, the FC magnetization is significantly stronger than the ZFC signal, and joins the ZFC data at $T \geq T_f$. This joining usually occurs near to the ZFC peak (within the $\pm$ 0.5K error), but in some cases, at temperatures much higher. Since the latter behavior tends to diminish as the sample ages, or is removed from the substrate, strains created during the growth may be the cause. Aging or substrate removal does not alter the ZFC curve peak location to

within experimental uncertainties, and for this reason the ZFC curve peak was used for T_f determination rather that the onset of irreversibility between the FC and ZFC curves.

Ideally the smallest measuring field (H_m) possible should be used in the low field static magnetization measurements. Figure 5.3 shows FC and ZFC static magnetization curves for multilayers with our thinnest value of W_{SG} using H_m = 100 and 10 G. Even in this most challenging case, the difference in T_f between H_m = 10 and 100 G was small, within our ± 0.5 K error. Therefore H_m = 100 G was chosen because it gave better signal to noise ratio. Notice also that the value of T_f in these data is not strongly dependent on whether one defines T_f to be the ZFC peak or the onset of separation between FC and ZFC data.

In Chapter 1, the long relaxations present in the SG state were shown to cause weak measuring time dependence in the location of the peak in a bulk sputtered $Cu_{0.86}Mn_{0.14}$ film, and stronger measuring time dependence in a thin, 2D $Cu_{0.86}Mn_{0.14}$/Cu sample with W_{SG} = 3 nm (see Section 1.63.1). Figure 5.4 shows a typical M vs. T curve taken at ~ 3 minutes per data point and the corresponding peak in the ac susceptibility at 16 Hz for a multilayer with thin W_{SG} = 2 nm $Cu_{0.89}Mn_{0.11}$ layers. The fast measurement gives only slightly higher T_f than found in the ZFC measurement. All T_f values used in this thesis are obtained from the ZFC peak, and are listed in Appendix A.

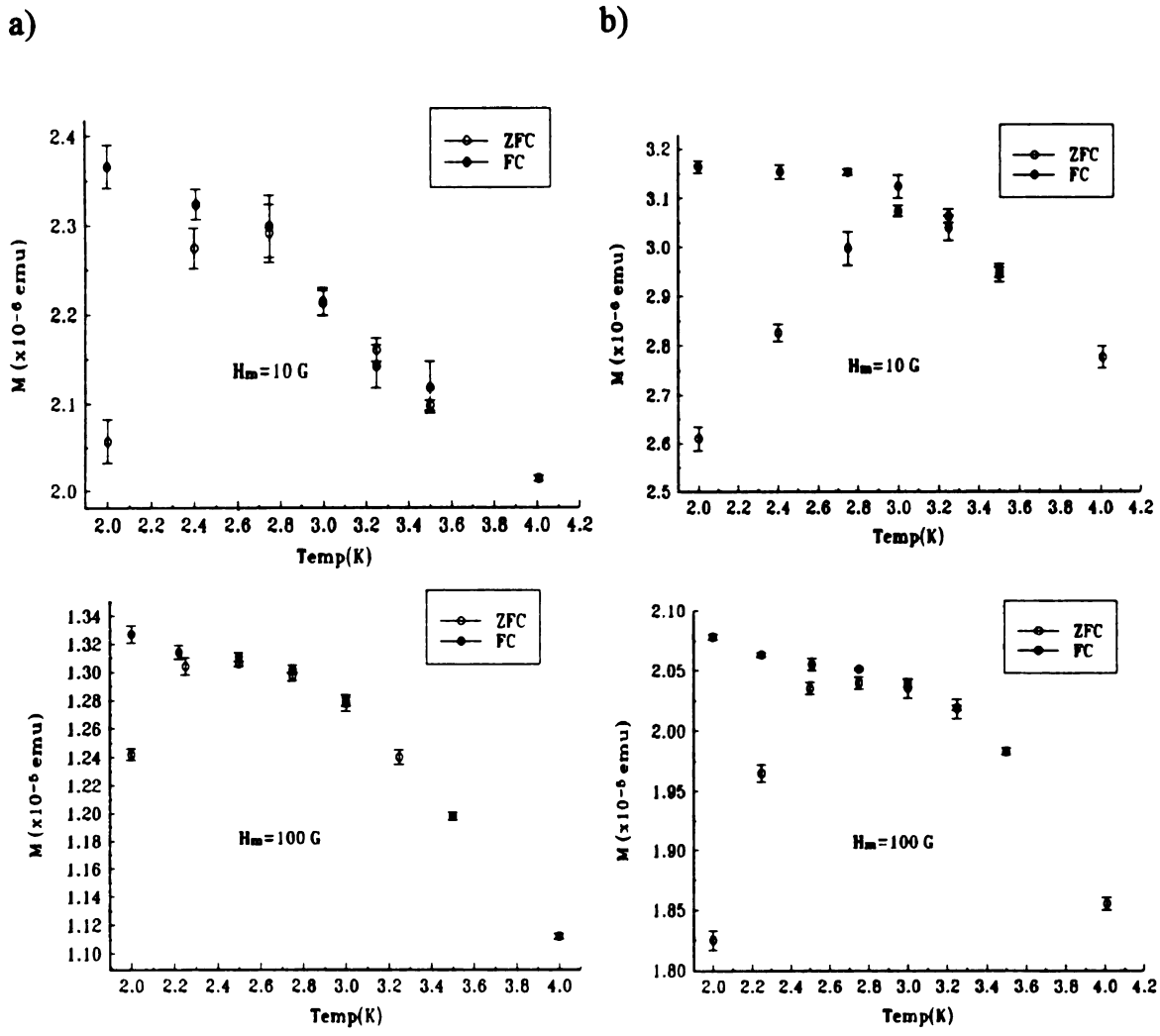

Figure 5.3 Comparison between Hm = 100G and Hm =10 G for a) $Cu_{0.89}Mn_{0.11}$/Cu 0.21 nm/30 nm and b) $Cu_{0.89}Mn_{0.11}$/Ag 0.21 nm/30 nm.

a)

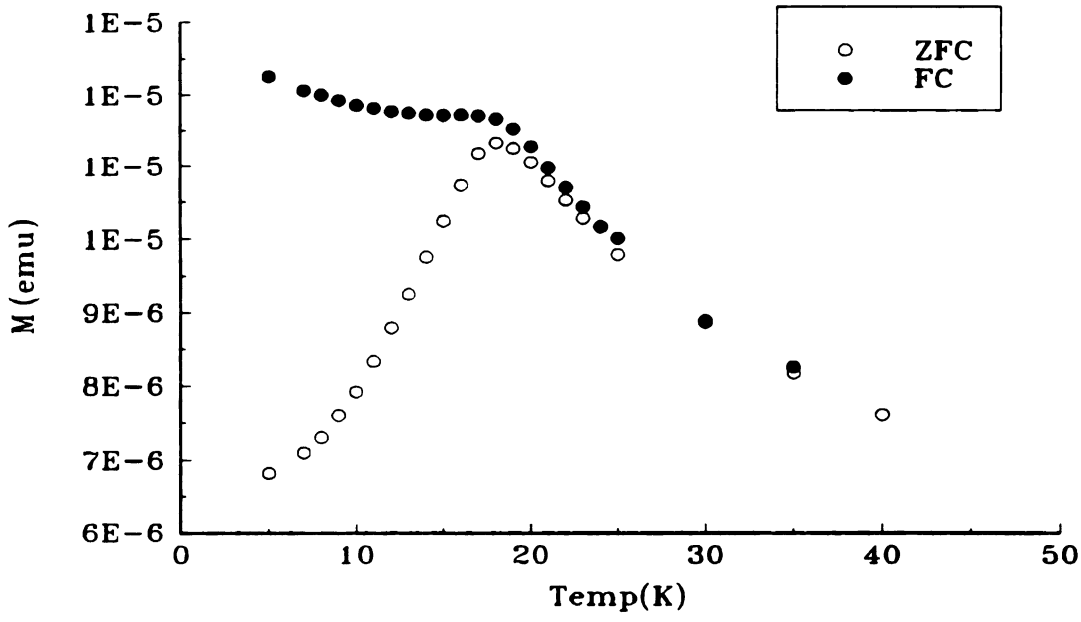

b)

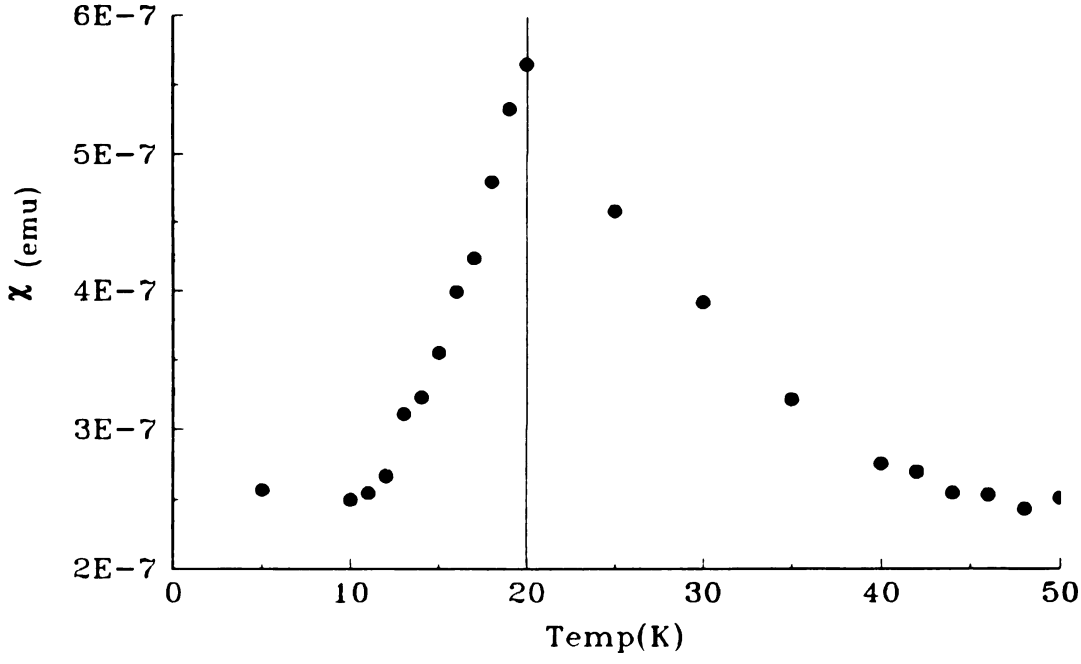

Figure 5.4 a) Static magnetization and b) ac susceptibility for $Cu_{0.89}Mn_{0.11}$/Cu 2nm/30nm.

5.3 T_f^b - CuMn, AgMn, and AuFe

Bulk T_fs, T_f^bs, for $Cu_{0.90}Mn_{0.10}$, $Cu_{0.89}Mn_{0.11}$, and $Cu_{0.88}Mn_{0.12}$ were taken from the T_f of the target shavings, since there was general agreement between the T_f of shavings and the T_f from thick sputtered films ($\geq$ 500 nm). An error of $\pm$1K was assigned to T_f^b to reflect the statistical variation in the values of the T_fs for bulk films.

Target shavings of the other SGs proved unsuitable as T_f^bs. The transition temperature for thick films ($\geq$ 500 nm) of $Ag_{0.92}Mn_{0.08}$ was found by Stubi et. al.[81] to be ~ 40% lower than that found in the shavings. Reasons for this difference are discussed in Chapter 4. As a result, T_f^b for the $Ag_{0.91}Mn_{0.09}$ in this study was averaged from the thick films. The uncertainty on this average is $\pm$ 1.5K, a value reflecting a statistical variation in the T_fs of AgMn films that is somewhat larger than that found in CuMn. The result is a larger overall error in T_f/T_f^b for these samples.

As with the AgMn, $Au_{0.97}Fe_{0.03}$ sputtered a considerably lower concentration than what was found in the target (see Chapter 4), and so also required the use of an averaged T_f^b taken from the thick films in the appropriate run. The average concentration for an AuFe film was ~ 3 at.% Fe, as measured by EDX and T_f values taken from literature. [59] The experimental uncertainty in T_f^b was $\pm$ 1.5 K, reflecting the spread in T_fs occurring for the thick films during the run.

The $CuMn_{0.4}Au_{0.01}$ samples were made much later than the CuMn samples. T_f^b was averaged from the thick films to achieve consistency in method of T_f^b determination between different materials.

Table 5.1 T_f^b values for CuMn, AgMn, and AuFe

SG	T_f^b (K)	Source
$Cu_{0.90}Mn_{0.10}$	47.0 ± 1	Target shavings
$Cu_{0.89}Mn_{0.11}$	49.5±1	Target shavings
$Cu_{0.88}Mn_{0.12}$	58.5±1	Target shavings
$Ag_{0.92}Mn_{0.08}$	24.8±1.5	Film average
$Au_{0.97}Fe_{0.03}$	17.0±0.6 run 1	Film average
$Au_{0.97}Fe_{0.03}$	16.1±0.6 run 2	Film average
$CuMn_{0.4}Au_{0.01}$	25.3 ± 1	Film average

5.4 T_f^b - NiMn

Our first attempt to sputter NiMn films involved a composite sputtering target made by setting flat Mn chips on top of an ordinary Ni target. Not only was it difficult to estimate the number of Mn chips needed to produce the desired film concentration, the sputtered concentration fluctuated widely and decreased with time as the Ni deposited onto the Mn chips, choking off the Mn supply. Alloy targets were then melted as described in Chapter 3. Target shavings could not be compared to the thick films, because the transition temperatures are highly sensitive to sample preparation.

The first thick films grown from the alloy targets using usual substrate temperature (T_{sub}) control of $-30 > T_{sub} > 10°c$ produced samples with unacceptable variance in magnetic behavior. Some films showed a single peak in the susceptibility, and static scans

that changed very little when changing the measuring field from 10 to 100 G. Other films showed behavior seen in Figure 6.13.

a)

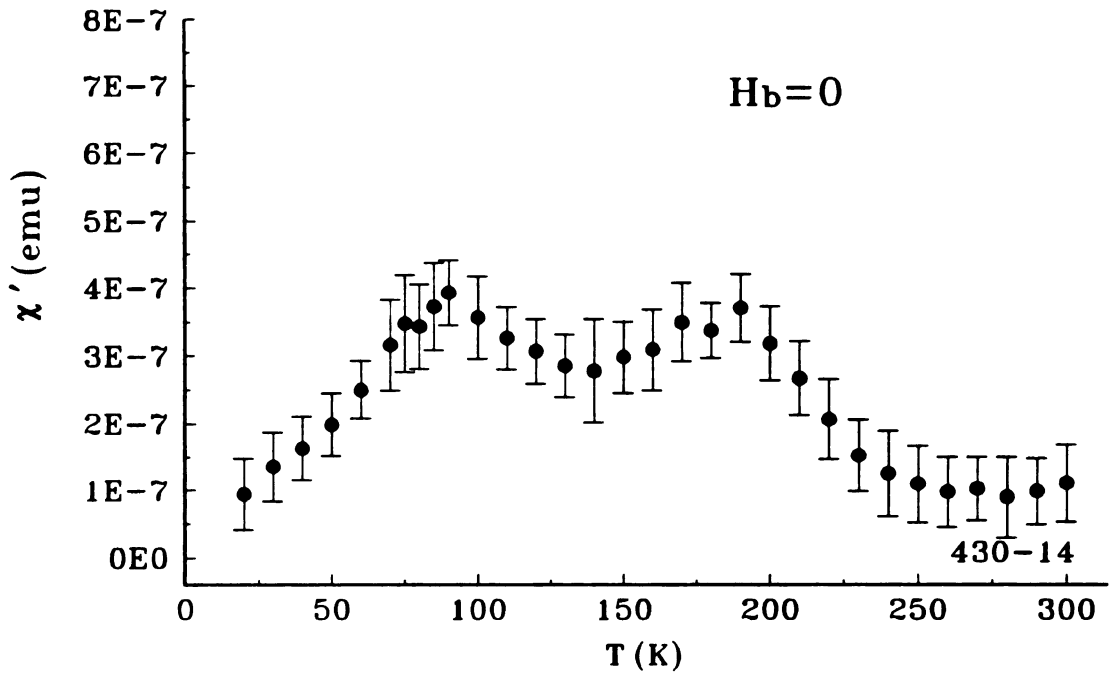

b)

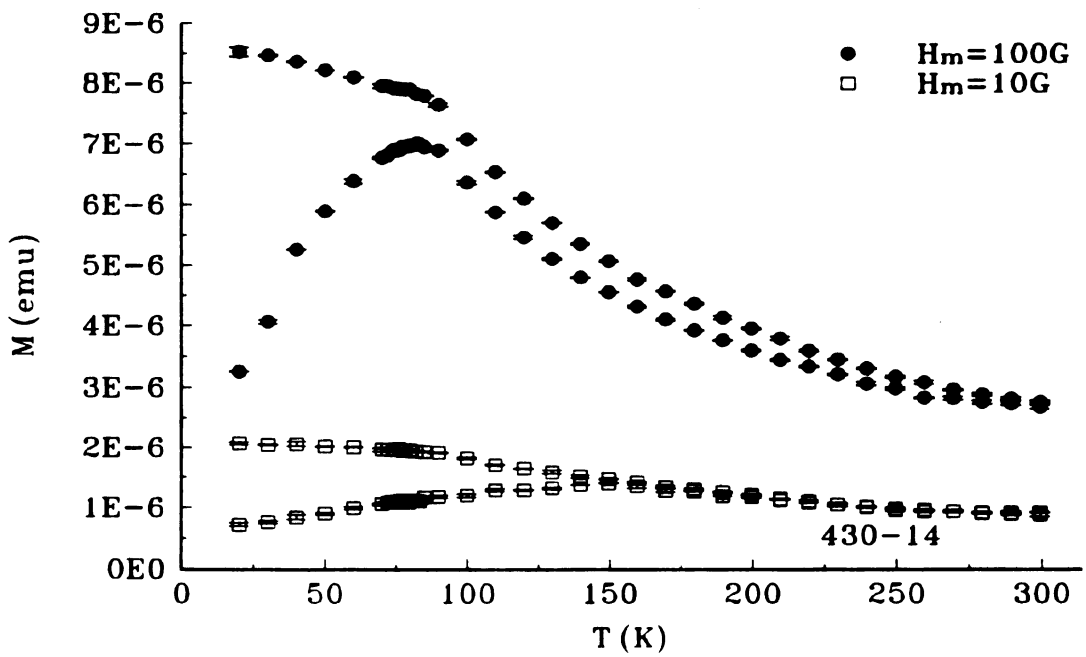

Figure 6.13 An early NiMn bulk film with unusual magnetic behavior a) double peaked χ vs. T scan with no biasing field (H_b) and b) strong dependence of T_f on measuring field H_m.

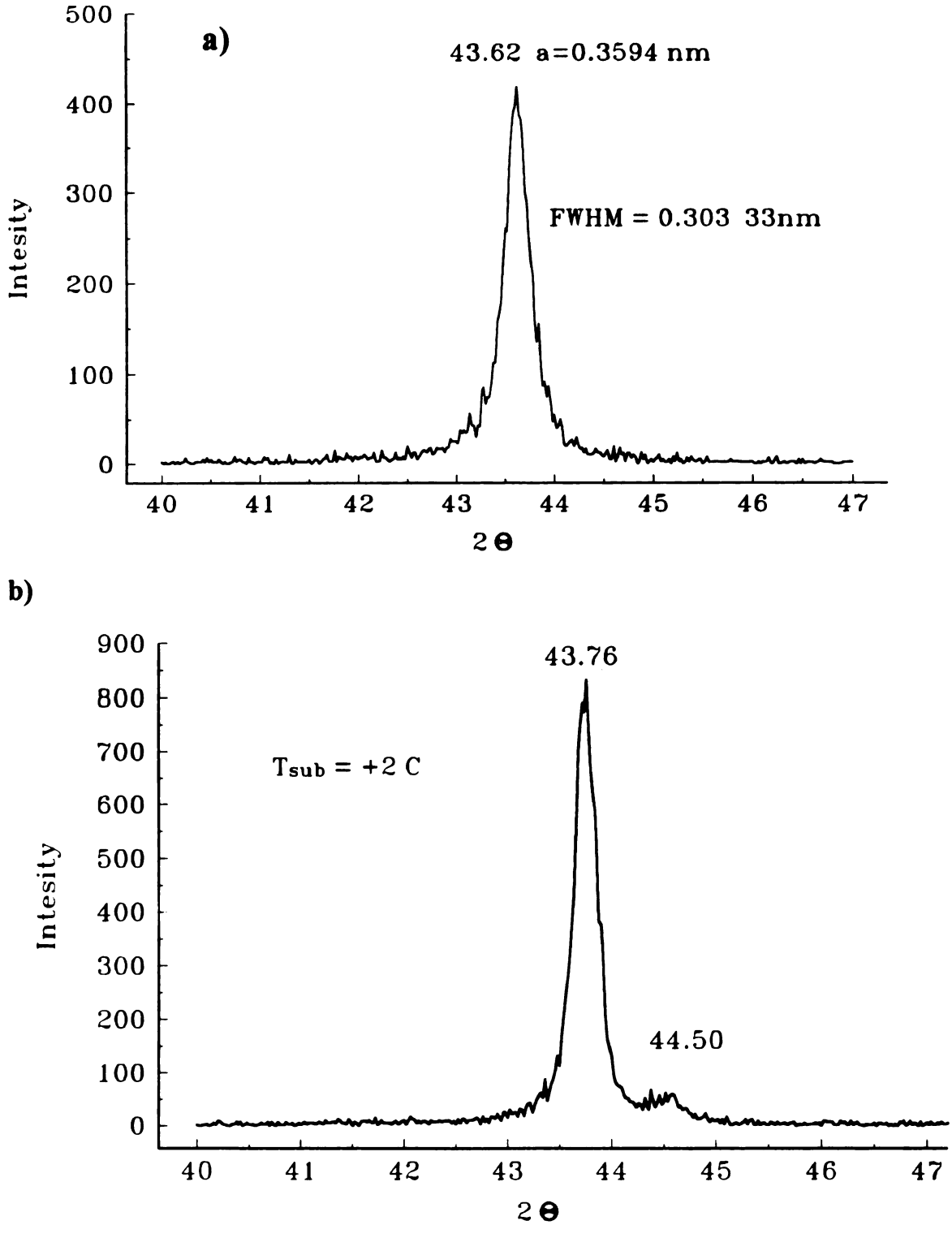

Figure 6.14 X-ray diffraction scans of NiMn SG sample with a) single peak from sample grown under good temperature control b) additional peak suspected to be caused by warmer growth conditions.

Many of these samples also displayed a second x-ray diffraction peak at 44.5° 2θ, where only one <111> peak is expected (see Figure 6.14). This second x-ray peak does not match up with any NiMn crystallographic orientations, but is consistent with a pure Ni <111> peak.

Keeping T_{sub} under more stringent control of (-20 ± 5) °C, at times halting the run to let the sputtering system cool, provided more consistency in film behavior. Some natural drift in the concentration still occurred, particularly between runs, resulting in different average concentrations and T_f^b values for each of the two runs. (Both runs were from the same target.) The first sample from each of two runs were bulk films that gave concentration readings significantly different from the other bulk films in the run (made every other or third sample), and so the first two samples in each run were not used.

Table 5.2 T_f^b values for NiMn

SG	T_f^b (K)	Source
$Ni_{0.71}Mn_{0.29}$	71 ± 3	Film averages
$Ni_{0.69}Mn_{0.31}$	86.4 ±2	Film averages

Averaging the thick film values for the two runs gave T_f^b = 71±3 and 86.4±2 K. Actual T_f^b values from thick films in these runs are listed in Appendix A1 Table **A1.9**. All well-cooled samples produced only one x-ray diffraction peak, that shown in Figure 6.14a. Samples left at room temperature for several weeks, and samples exposed to the electron beam used for the EDX composition analysis, often displayed magnetic behavior which resembled Figure 6.13, and developed the second x-ray diffraction peak like that seen in Figure 6.14b. Whether the x-ray peak is from growth of pure Ni or that of a NiMn

compound, it indicates a change in the sample that is likely similar to that which occurred in the early samples during sputtering. For this reason, and warnings given in literature about potential growth of ferromagnetic Ni_3Mn in samples held at room temperature,[60] the samples were kept in liquid nitrogen until measurement.

Both static magnetization and ac susceptibility scans were taken of the SG samples to verify SG (as opposed to reentrant) behavior. Figure 6.15 shows a SG sample. The purpose of the biasing field, H_b is explained in the next chapter.

5.5 Errors in Relevant Values

As stated above, the error in determining T_f is $\pm$ 0.5K. In some cases, at low temperatures where the peak is better defined or the data are taken closer together, the error may be as low as $\pm$ 0.3 K. T_f values and their errors are tabulated in Appendix A. The experimental uncertainty in the quantity T_f/T_f^b is generated by this error on T_f and the error on the appropriate T_f^b, as stipulated above. These uncertainties may also be found in Appendix A.

Errors in W_{SG} and W_{IL} are $\pm$ 5%, as discussed in Chapter 4.

a)

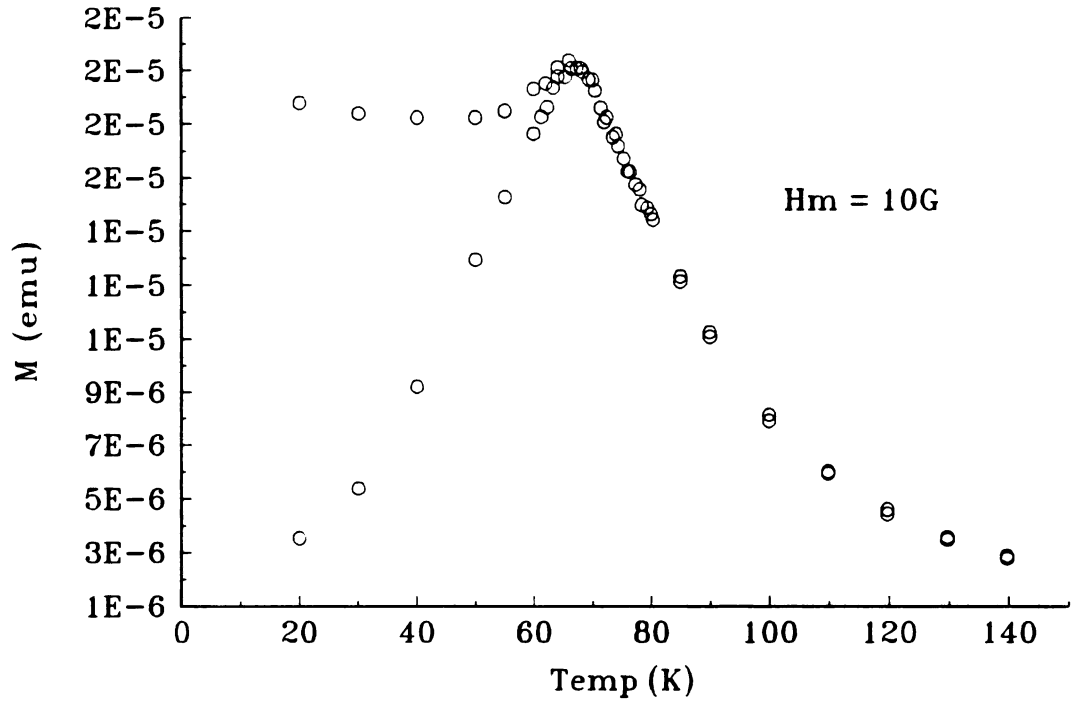

b)

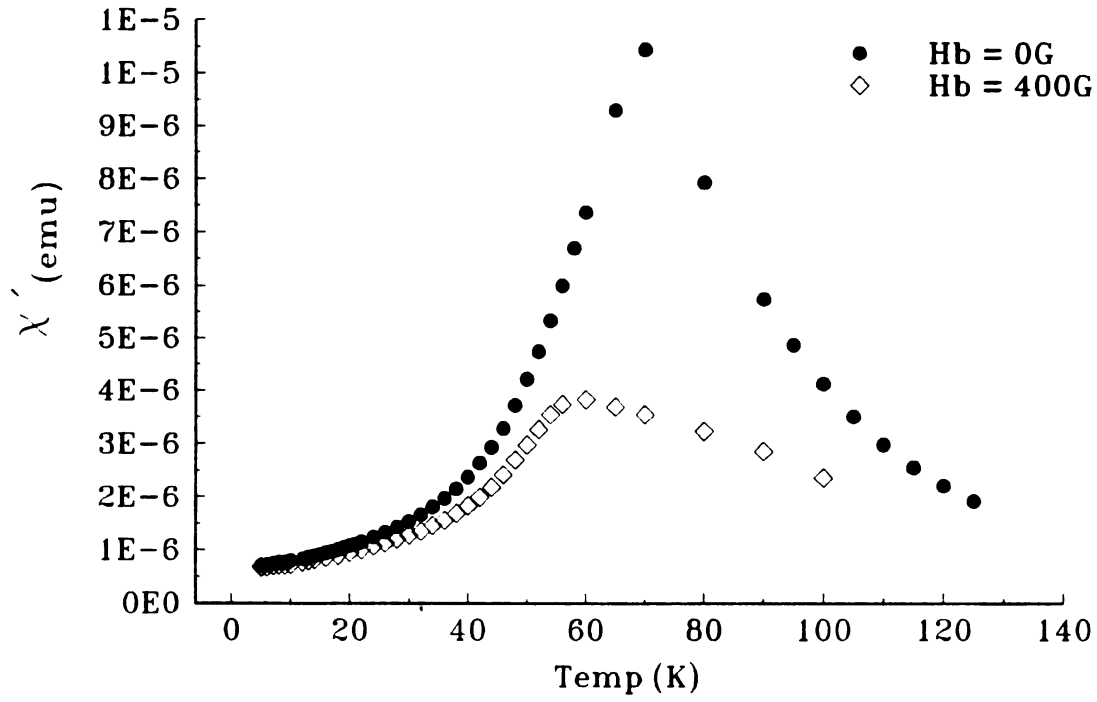

Figure. 6.15 b) Static magnetization and b) a.c. susceptibility SG film with and without the biasing field (H_b) of a 300 nm $Ni_{0.74}Mn_{0.26}$.

CHAPTER 6

DATA

6.1 Finite Size Effects - CuMn

As described in Chapter 1, previous studies of the long range metallic SG CuMn showed significant decreases in T_f with decreasing W_{SG} down to W_{SG} = 2 nm. In Section 1.5 it was argued that samples with thinner W_{SG} were needed to determine the value of T_f for W_{SG} = 1 ML, and to distinguish between the Fisher-Huse Droplet model and general scaling analysis. The following describes the results of such a study.

6.1.1 Host Interlayers

To determine unambiguously whether T_f = 0K at W_{SG} = 1 ML, $Cu_{0.89}Mn_{0.11}$ and $Cu_{0.88}Mn_{0.12}$ multilayers were made down to this thickness, (W_{SG} ~ 0.21 nm). The SG layers were separated by Cu, Ag, or Au interlayers of 30 nm, a thickness previously shown sufficient to magnetically decouple CuMn SG layers[101,100] These ILs were chosen to perturb the SG layer the least; Cu, Ag, and Au all have the same electronic structure as the Cu in the CuMn, the same FCC structure, and Cu has nearly the same lattice parameter as the CuMn.

The presence of SG characteristics in these thinnest W_{SG} samples is confirmed in Figure 5.3. Notice that the value of T_f is not 0 K. A test sample made of W_{SG} = 0.21 nm

and W_{IL} = 60 nm showed no change in the value of T_f from the W_{IL} = 30 nm case, confirming that for the quasi- static T_f measurement these samples are magnetically decoupled by a 30 nm IL.

We showed in Section 1.5 that T_f data from similar samples of $Cu_{1-X}Mn_X$/Cu with W_{SG} > 2 nm collapsed nearly upon one another for X = 0.04 to X = 0.14 when normalized by the appropriate bulk spin freezing temperature, T_f^b (see Figure 1.7). This suggests that $Cu_{0.89}Mn_{0.11}$ ($T_f^b \sim 47$ K) and the $Cu_{0.88}Mn_{0.12}$ ($T_f^b \sim 58.5$ K) data should be similarly compared to each other and to the older $Cu_{0.86}Mn_{0.14}$ data after normalization. The uncertainties in the plotted values are discussed in Chapter 5, and are approximately the size of the symbols depicted in the following figures.

From chapter 2, the data will be fit to the general scaling law

$$\frac{T_f(W) - T_f^b}{T_f^b} \sim \left(\frac{W}{W_c}\right)^{-1/\nu}, \qquad \text{Equation 2.4}$$

where ν is the correlation length exponent, and to the Droplet Model form for thin W_{SG}

$$\frac{T_f}{T_c} \sim W^a . \qquad \text{Equation 2.6}$$

Here $a < 2$ from the droplet theory, and is estimated through a literature average from experiment and calculation to be $0.3 \leq a \leq 0.65$, the uncertainties of which are discussed in Section 2.2.

Figure 6.1 shows the normalized T_f data for CuMn/host multilayers. The normalized data for $Cu_{0.89}Mn_{0.11}$ and $Cu_{0.88}Mn_{0.12}$ do indeed collapse onto a single curve, and the new data are in good agreement in the overlap region with the previous data. The data indicate that T_f is still finite at W_{SG} = 1 ML.

The solid curve in figure 6.1 represents the scaling equation 2.2, with the values of $\nu = 1.6$ and $W_c = 1$ nm that allow fitting over the widest possible range. It is now clear that the generalized scaling law is incapable of fitting data for W_{SG} below ~ 1nm, where the inflection point occurs.

Figure 6.2 shows the data of Figure 6.1 replotted on a log-log scale for comparison to Equation 2.3. Straight line behavior, indicative of a power law, is observed for $0.21 \leq W_{SG} \leq 2$ nm. From Chapter 2, Equation 2.4 should be valid for 1) $T_f << T_f^b$ and 2) W_{SG} > average impurity spacing. Condition 1) is met through the significant T_f depression occurring by 2 nm. Condition 2) should limit consideration to $W_{SG} > 1$ML, so the theory may not be directly applicable to the thinnest W_{SG} data. Since the values for $W_{SG} = 0.21$ nm are in line with the data for thicker W_{SG}, they were included in the calculation of the exponent *a*.

Using a linear regression fit on the $\log(W_{SG})$ and $\log(T_f/T_f^b)$ data for 0.21 nm < W_{SG} < 2 nm, the solid line in Figure 5.5 was produced, corresponding to $a = 0.8 \pm 0.1$. This value is outside the estimate from the literature parameters, but still well below the rigorous bound of 2.

Since determining when each monolayer is complete is not possible for a sputtering technique, the thinnest layers and boundaries between layers will not be perfectly planar. We must thus justify plotting the data as though the layers were "perfect". Figure 6.3a shows a schematic of the cross section for a SG/host system. When the IL is made of *host* material (a material in which the Mn impurity behaves the same as in the SG) a blending of the SG and IL creates a wider, more dilute SG layer. While this dilution reduces T_f ($T_f \sim c^{0.7}$ where c is the concentration in the range 0-13 at.% Mn in Cu[42]), widening the SG layer increases T_f, ($T_f \sim W_{SG}^{0.8}$). Since the powers are so similar, these two effects should approximately cancel each other, yielding a measured value close to that of a true unmixed layer.

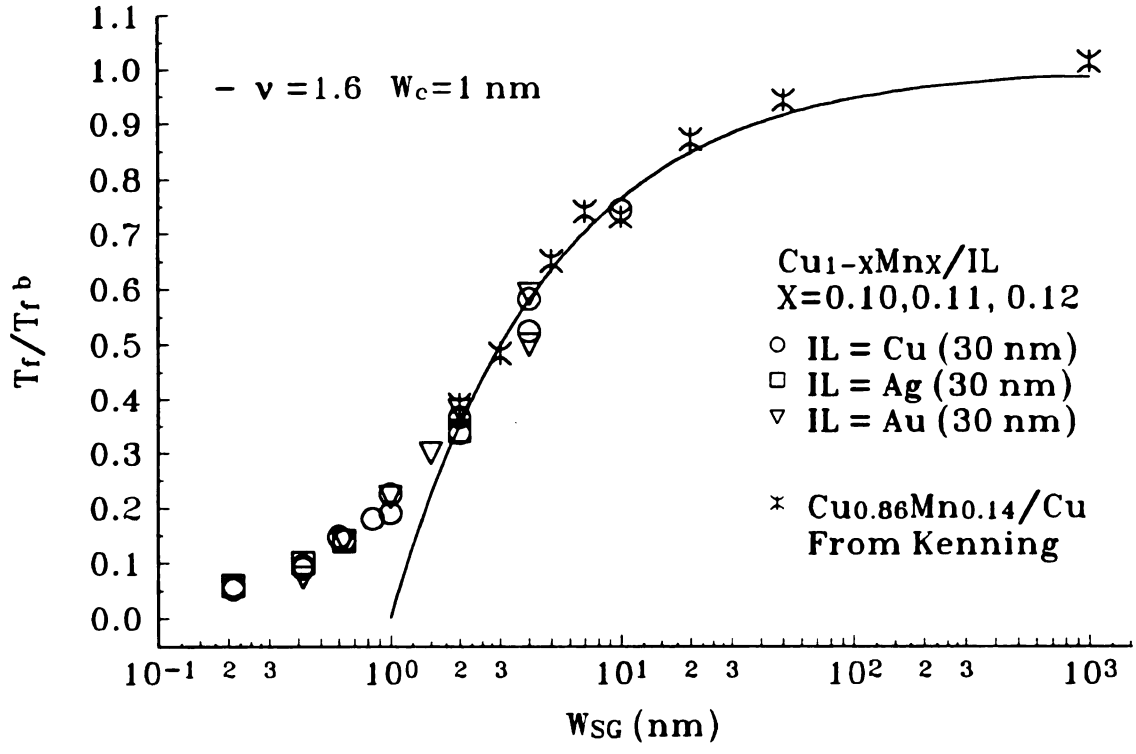

Figure 6.1 CuMn/host multilayers showing scaling law behavior for thick SG layers

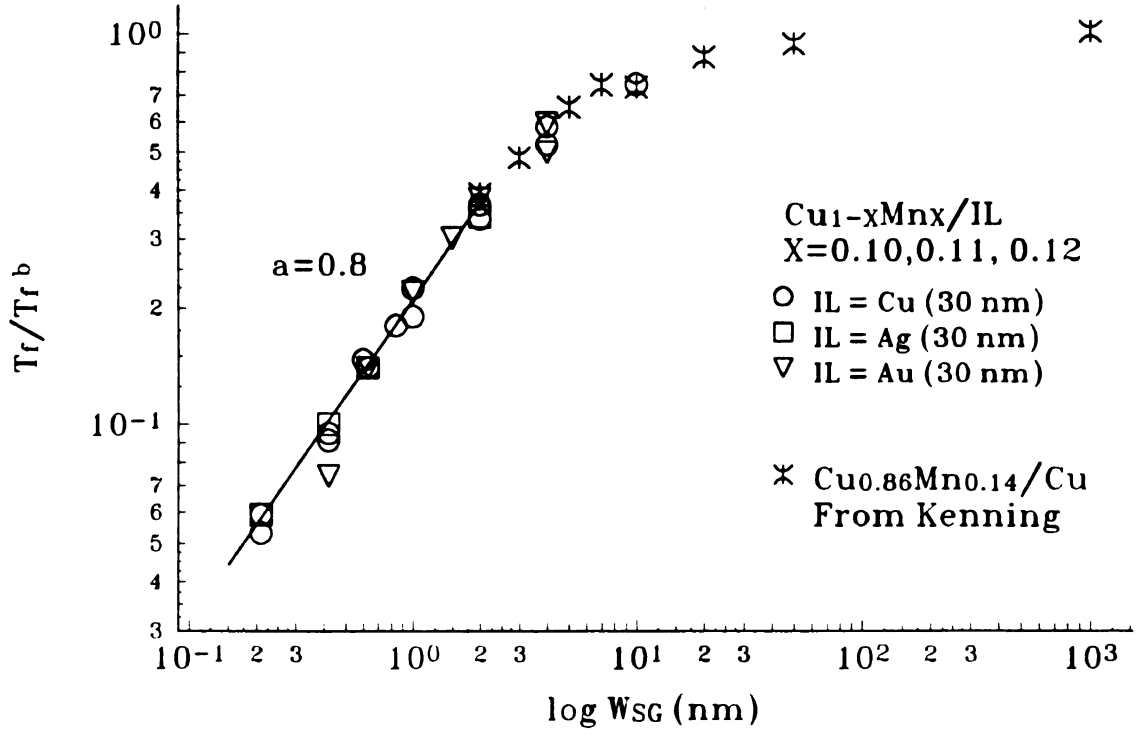

Figure 6.2 Droplet model power law behavior of thin CuMn layers with "host" interlayers.

6.1.2 Non-host Interlayers

As mentioned in the previous section, some mixing between layers must inevitably occur during the sputtering process. We can estimate the degree of mixing by comparing data for host and non-host ILs.

In the case of the non-host IL, two effects are present. Both effects reduce T_f. First, mixing at the boundary removes impurities from the SG layer if the IL doesn't support a SG state, resulting in an effectively thinner SG layer (see Figure 6.3b). Second, the non-host IL may not support the RKKY interaction as well as the host IL, (as is clearly the case with an insulator), causing some loss of interactions between impurities at the edge of the SG layer.

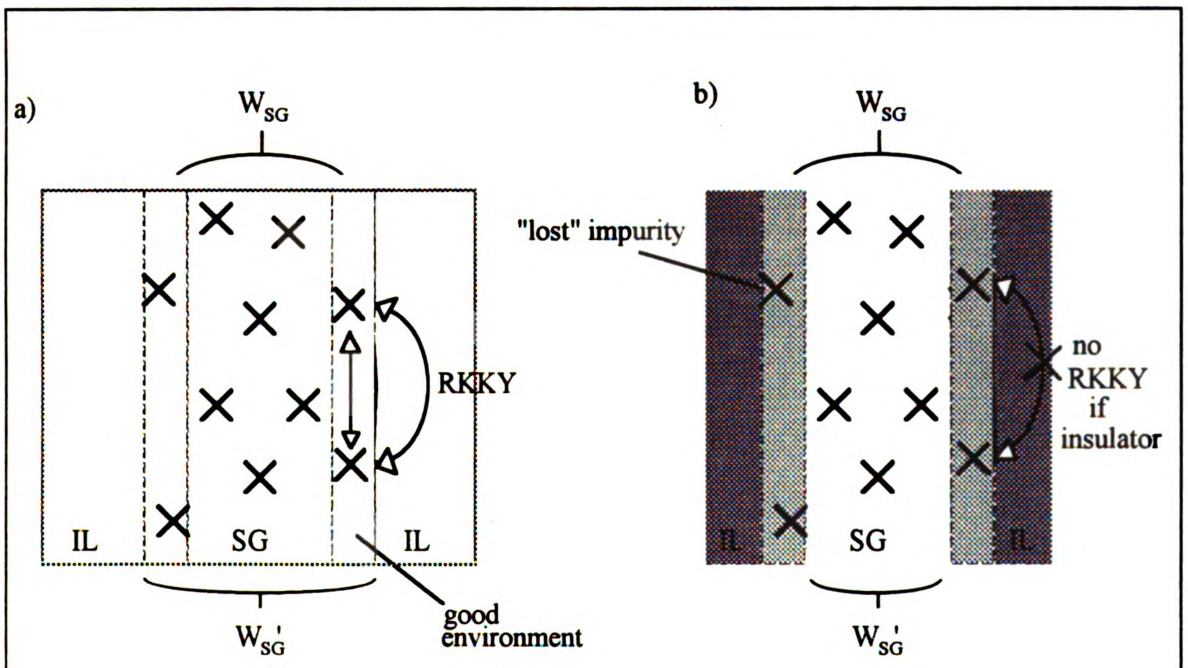

Figure 6.3 Comparison of mixing cases for a) host and b) non-host ILs, where W_{SG} = nominal layer thickness, W_{SG}' = effective layer thickness.

The two studies of CuMn multilayers previously done with non-host ILs (reviewed in Section 1.5) both used insulating ILs (Si and Al_2O_3), and produced faster decreases in T_f than that observed for the CuMn/host samples (see Figure 1.8). To see if this behavior is mimicked by non-insulating materials, samples were made using several metallic non-host interlayers of W_{IL} = 30 nm. Figure 6.4 shows the normalized T_f data plotted next to a solid curve representing the CuMn/host data of Figure 6.2. The downward pointing arrows indicate samples for which $T_f \leq 2K$, the lower limit on the magnetometer. The metal IL data fall faster than the host IL curve, but not as quickly as the insulator IL data previously found. If the CuMn/host data are representative of a nominal thickness SG layer, subtracting a constant thickness of 0.5 to 1.0 nm from each series accounts for the observed reduction in T_f, even if no T_f reduction is attributed to some loss of RKKY interaction through the flanking non-host interlayers. Figure 6.5 illustrates this idea by replotting the data with the estimated effective thickness, W_{SG}'.

Table 6.1 Estimated values of CuMn mixing with non-host metal ILs.

IL	$W_{SG} - W_{SG}'$	ML mixing
Al	1 nm	~ 5
V	0.75 nm	~ 4
Mo	0.5 nm	~ 3

Taking these derived reductions in W_{SG} as a guide, we conclude that mixing at interfaces must be limited to ~ 2 layers on each side, with the largest mixing (~5 ML total) in the CuMn/Al system.

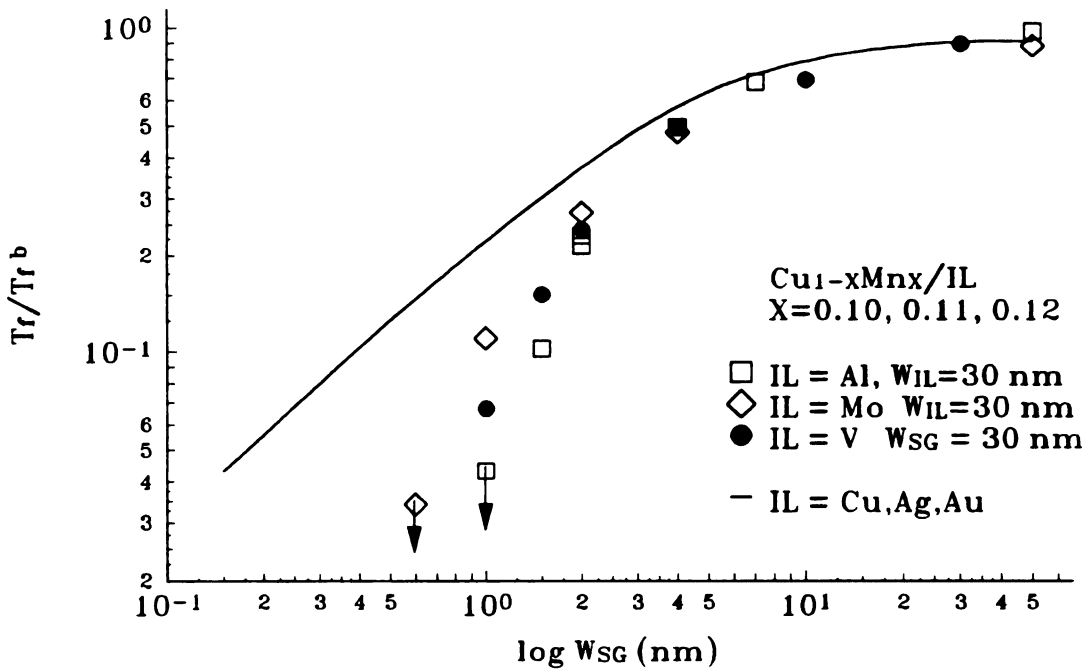

Figure 6.4 T_f reduction due to "non-host" interlayers. The solid line represents data for the CuMn/host IL from Figure 6.2.

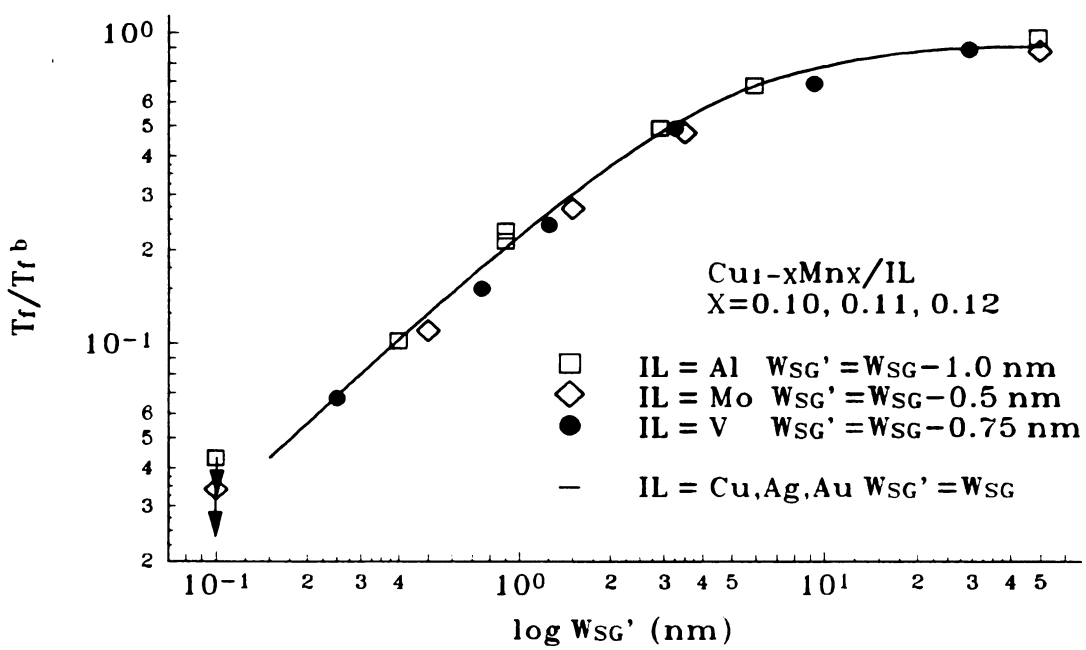

Figure 6.5 Replotted data for metallic ILs using effective SG layer thickness (W_{SG}').

6.2 Coupling -CuMn

In the original studies on CuMn multilayers reviewed in Section 1.5, an unusually long coupling length of CuMn through Cu and Ag ILs was observed, while a shorter coupling length was found through the insulating IL Si. It is of interest to know whether other metal ILs exhibit similar long range coupling as do Cu and Ag. To observe the degree of coupling through a given interlayer, W_{SG} must be fixed, while W_{IL} is changed from 30 $\rightarrow$ 0 nm. A SG thickness must be chosen that is thin enough to show significant T_f depression, so that the depressed T_f value can be seen to return to its bulk value as W_{IL} $\rightarrow$ 0. The chosen W_{SG} must also be thick enough that the mixed regions at the boundaries represent a small portion of the layer. Both conditions are met with W_{SG} = 4 nm, where $T_f/T_f^b \sim 0.5$ for all metal ILs (see Figure 6.4).

6.2.1 Host Interlayers

Measurements on CuMn coupling through Cu and Ag ILs taken by Stubi et. al.,[100,101] showed coupling out to $\geq$ 20 nm in both cases. Since Cu and Ag have FCC lattice parameters that differ by 13%, this behavior suggests that lattice mismatch at the boundaries is not an important factor in coupling. The first metal chosen to be tested against the Cu and Ag IL results was the host metal Au, which behaved similarly to the Cu and Ag ILs in the finite size effect study. Au is a strong spin-orbit coupler, a trait often associated with the ability to provide extra Dyzaloshinki-Moriya anisotropy interaction in CuMn (see Section 1.3.3). Second, CuGe was selected as a small variation on the Cu IL, to test the effect of simply reducing the mean free path. Adding 2 and 10 at. % Ge reduced the mean free path in Cu by a factors of about 10 and 60, respectively[140], while causing little disturbance in the electronic or crystallographic structure.

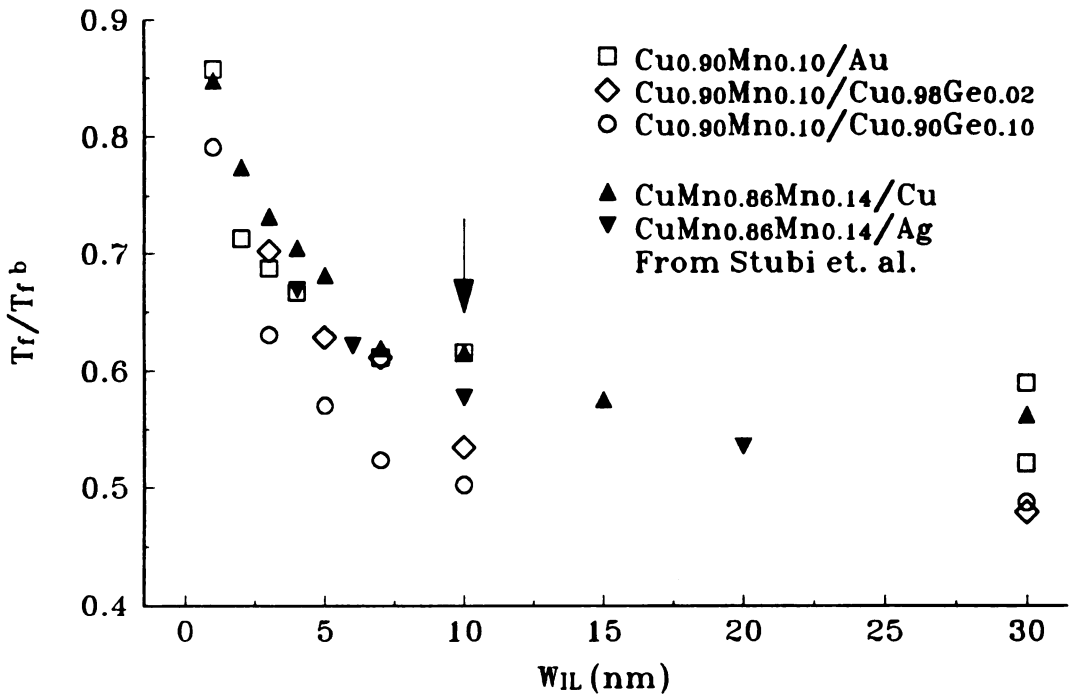

Figure 6.6 CuMn coupling through host interlayers and CuGe ILs.

Figure 6.6 shows the coupling of CuMn through Cu, Ag, Au, and CuGe ILs with W_{SG} = 4 nm. The Au IL data show the same long coupling as Cu and Ag, the effects of which may be seen out to W_{IL}~20-30 nm, with a more noticeable rise in T_f for W_{IL} < 10 nm. Adding the Ge to the Cu has little effect on the coupling behavior. Coupling is still observed out to W_{IL} ~ 20-30 nm, the onset of faster T_f rising occurring perhaps at a slightly lower value for the $Cu_{0.90}Ge_{0.10}$ series than the $Cu_{0.98}Ge_{0.02}$ series. These behaviors suggest that neither spin-orbit scattering in the IL nor mean free path effects play a significant role in the coupling length.

6.2.2 Non-host Interlayers

The non-host IL materials were chosen to have properties which distinguish them from host materials and from each other. Al has the same FCC crystal structure as the noble metals, and nearly the same lattice parameter as Ag and Au. It is a nearly free electron, *s*-band metal, and a weak spin-orbit coupler, but has a different electronic structure from Cu, Ag, and Au. Nb, Mo, and V are all BCC transition metals with predominantly *d*-band electronic states at the Fermi surface. Si is an amorphous insulator. To make a comparison between metal IL samples and Si IL samples, a series of the latter was made using a fixed W_{SG} = 7 nm with variable a-Si IL thicknesses. Such samples correspond to T_f/T_f^b ~ 0.5 when decoupled (see Figure 6.10).

Figure 6.7 compares the coupling behavior through five non-host materials with that for Cu, Ag, and Au. Al, while having many similarities to the hosts, does not allow the long range coupling of the noble metals. Neither do the transition metals nor Si. All these materials show significant coupling only when $W_{IL} \leq$ 2-3 nm.

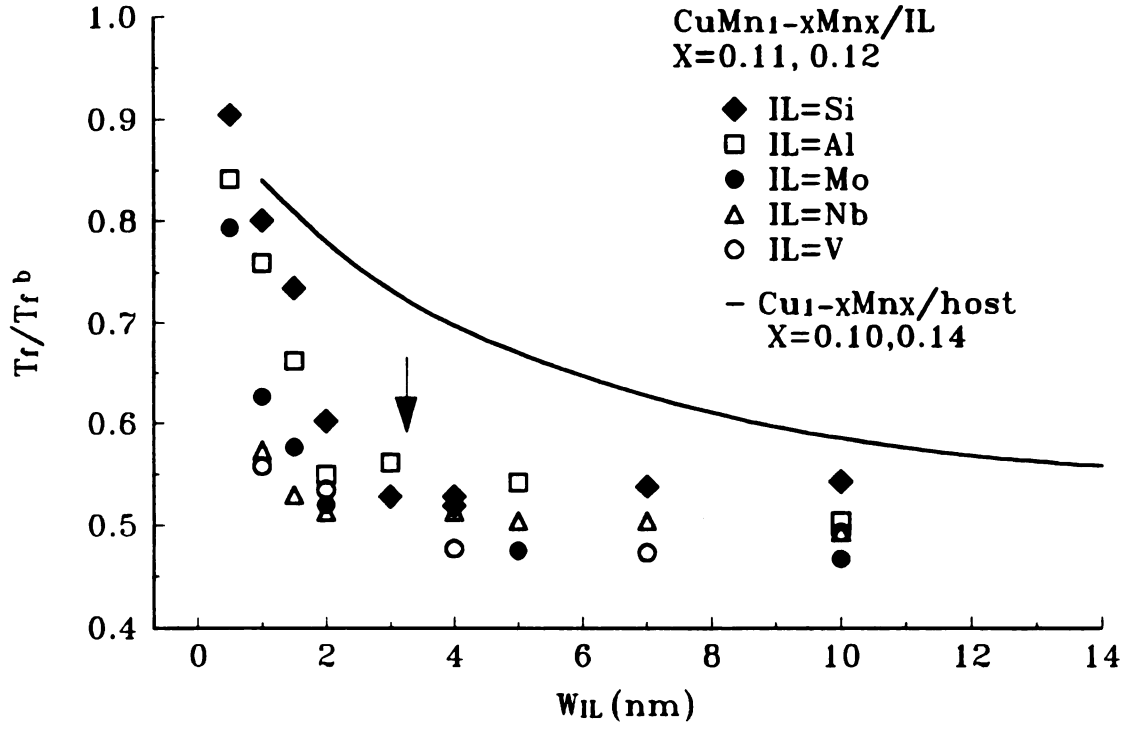

Figure 6.7 CuMn coupling through non-host interlayers

The Al and Si series do exhibit a feature different from the other materials, a sharp rise below $W_{IL} \sim 3$. For Si ILs, this behavior can be expected from the structure analysis of these samples in Section 4.4, where it is argued that a breakdown in layering occurs between $W_{IL} = 3$ nm and $W_{IL} = 2$ nm. This layering deficiency is likely to cause breaches in the Si layer where a CuMn layer can be in physical contact with the neighboring layer, causing the rapid increase in T_f.

The CuMn/Al x-ray diffraction structural analysis did not reveal a breakdown of layering associated with the rapid T_f increase. The finite size effect data from section 6.1.2 do suggest, however, that ~ 0.5 nm of mixing occurs at each CuMn/Al interface, leaving only a couple of ML of pure Al at $W_{IL} = 1.5$ nm, which may contain pinholes through which the CuMn can couple strongly.

6.3 Other SGs

6.3.1 AgMn

A second SG was studied to determine whether the finite size effect behavior described in the preceding section is unique to CuMn. AgMn was chosen as the SG most like CuMn, as they are both long-range RKKY Heisenberg metallic SGs, both using noble metal hosts and the same impurity (Mn). As described in Chapter 1, Stubi et. al.[81] made AgMn/Cu and AgMn/Ag multilayers with 1 nm $\leq W_{SG} \leq =$ 500 nm to compare with the CuMn/Cu data of Kenning et. al..[79] They found little difference between the finite size behavior of the two SGs. As for CuMn, no difference was observed between multilayers using Cu and those using Ag as the interlayer. To test whether the similarity of AgMn to CuMn holds when $W_{SG} < 1$ nm, $Ag_{0.92}Mn_{0.08}$ multilayers with W_{SG} as thin as possible were made to compare to the data in Section 6.1.1. The lower limit was $W_{SG} = 2$ ML,

since the lower T_f^b (24.8 K) for these samples caused the T_f of W_{SG} = 1 ML samples to be below the susceptometer's low temperature limit of 2K.

Figure 6.8 shows the new data for the AgMn/host IL samples, extending the previous data from Stubi et. al. down to W_{SG} = 0.5 nm. The values for T_f/T_f^b of the AgMn system are slightly lower than those for the CuMn system, but the differences are within the total experimental uncertainties.

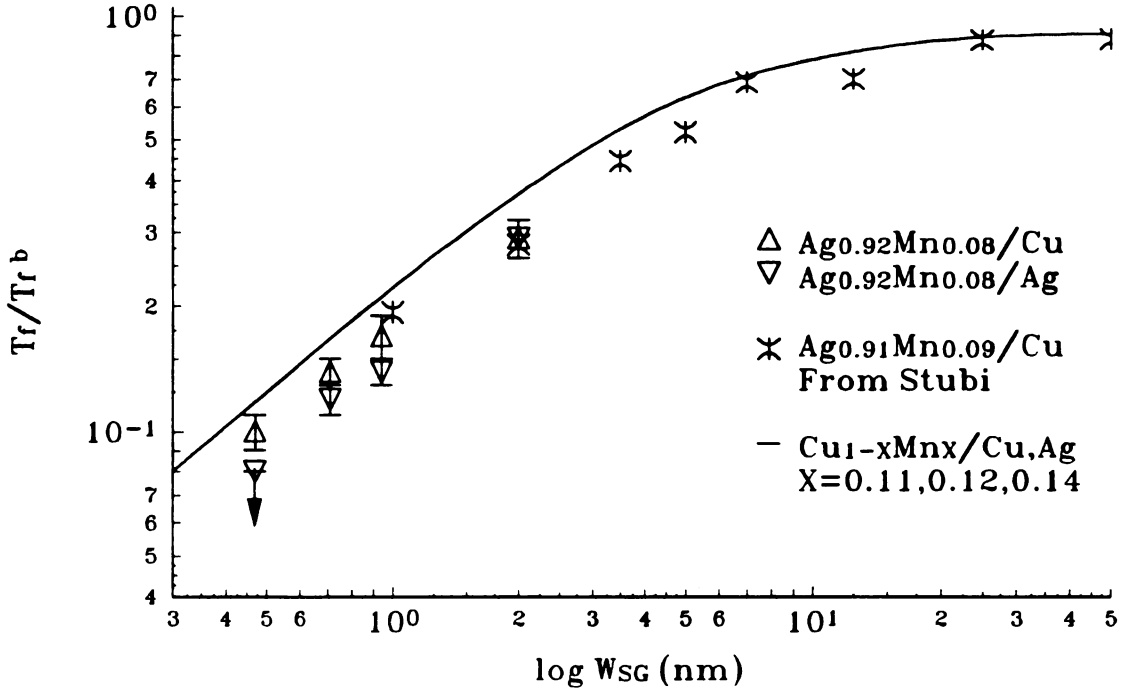

Figure 6.8 Size effect data for AgMn.
The solid line represents the averaged CuMn/host IL data from section 5.2.1 and Figure 6.2 with the concentrations indicated.

6.3.2 High Anisotropy SGs, CuMnAu and AuFe

As described in Section 1.4 , Monte Carlo simulations suggest that the lower critical dimension, d_l, is affected by the amount of anisotropy present in the sample. Adding anisotropic interactions in these simulations can allow d_l to be lowered from above to below 3, and lowering d_l may well affect the rate of T_f depression as W_{SG} decreases. CuMn is believed to be a low anisotropy SG. The anisotropy field (H_A), (see Section 1.3.3) is found to be about 300 G as measured by transverse susceptibility and NMR measurements[58]. Two SGs with higher anisotropy were tested against CuMn. First, $CuMnAu_X$ where $X < 0.03$, which shows a sharp increase of anisotropy with increasing X. Prejean et. al.[25,41] reported that $CuMnAu_X$ with X=0.0015 showed an increase of a factor of 6 in $H_A$over pure CuMn. Second, $Au_{1-X}Fe_X$ where $X < 0.012$, which is widly believed to be an intrisically high anisotropy SG, with $H_A \sim 50$kG, about 100 times the strength of that found for CuMn.[58] Otherwise CuMn, CuMnAu, and AuFe are similar; all are long range RKKY type SGs based on noble metal hosts.

The higher anisotropy in CuMnAu comes from the Dyzaloshinski-Moriya interactions, those caused by the interaction with a third impurity. These interactions are believed to be particularly prominent when the third impurity is a strong spin-orbit coupler like Au (see Section 1.3.3). The $CuMn_{0.04}Au_{0.01}$ samples contain an amount of gold that should produce an anisotropy field ~ 35 times larger than CuMn alone.[25,41]

The strong anisotropy in AuFe arises from two effects: a) the dipolar interaction, the interaction between two impurities, is much stronger in AuFe than in CuMn. The stronger interaction in AuFe arises from an orbital contribution to the Fe moment in Au (due to spin-orbit coupling), whereas Mn is a good S-state ion in Cu. Levy and Fert calculated a "pseudo-dipolar" interaction for AuFe that was 40 times the size of the classical dipolar one.[86] b) Dyzaloshinski-Moriya interactions are much stronger for Fe

atoms than Mn atoms. Levy and Fert calculated a maximum value of $H_A > 50kG$ from a triangle of Fe atoms, which is enough alone to account for the observed values of H_A.[86]

As was the case with AgMn, W_{SG} for CuMnAu and AuFe had a lower limit due to lower transition temperatures of these alloys (T_f^b for $CuMn_{0.4}Au_{0.01}$ was 25.3 K and for $Au_{0.97}Fe_{0.03}$ $T_f^b \sim 16K$). Figure 6.9 shows the data for thin W_{SG} layers of $CuMn_{0.4}Au_{0.01}$ with Cu and Ag ILs, and for $Au_{0.97}Fe_{0.03}$ with Au and Ag ILs. The solid line indicating the CuMn/host IL data from Figure 6.2 is added for comparison. The data for both systems follow almost the same curve to within the total experimental uncertainty. Raising the anisotropy thus did not significantly change the finite size effect behavior.

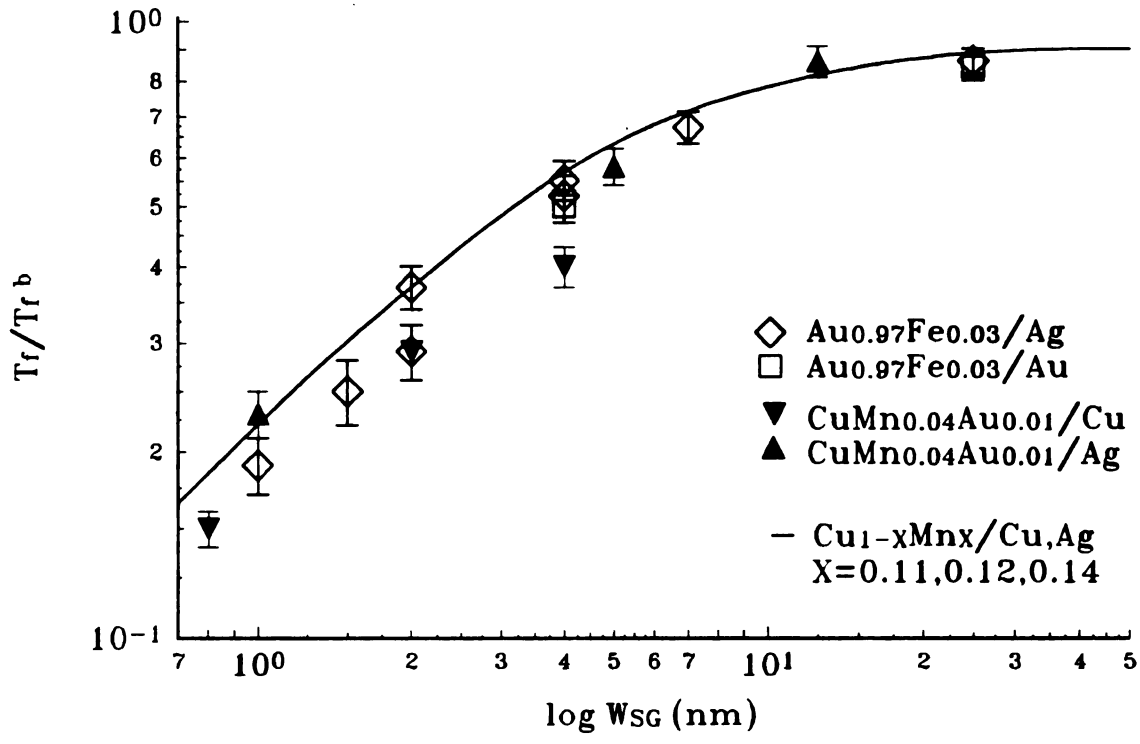

Figure 6.9 Size effect data for AuFe.
The solid line represents the averaged CuMn/host IL data as indicated.

6.4 Finite Size Effects of CuMn, AgMn, and AuFe with Si ILs

The above results for AuFe/host multilayers are clearly quite different from those reported by Vloeberghs et. al. shown in Figure 1.8 for single AuFe films. Their data fall faster than even the cold sputtered CuMn/Si data shown in the same figure. Since their AuFe films were evaporated onto glass with a SiO overlayer, there is a question about whether AuFe differs significantly from CuMn when flanked by an insulator.

To investigate this issue, SG/Si systems were made for SG = CuMn, AgMn, and AuFe with the concentrations described above. The CuMn/Si data reproduced that of Kenning et. al.[75] for cooled samples shown in Figure 1.8, with the addition of a W_{SG} = 1.5 nm point. All samples were sputtered cold, with substrate temperatures between -60 and 0 °C.

The complicated situation of mixing at the boundaries for the SG/Si multilayers is addressed in Section
4.4 Low angle X-ray diffraction analysis, and low resolution TEM imaging of cross sections of samples, show beautiful layering for all three systems. Cu, Ag, and Au are all capable of forming silicides.[61] One difference observed, from electron diffraction analysis, is a difference in crystallinity in thin layers of AuFe, CuMn, and AgMn. AuFe was found to be almost amorphous, with very small crystallites, and AgMn was the most crystalline of the three (see Section
4.4). Since one way Si may diffuse into the SG layer is along grain boundaries, one may expect more Si diffusion in the AuFe layers where there are more grain boundaries present.

Figure 6.10 shows the three SG systems with Si ILs. There appear to be slight differences between AgMn, CuMn, and AuFe. The AuFe curve is depressed the most, and the AgMn curve the least. Since the AuFe layers are believed to encourage Si

diffusion the most, and the AgMn layers the least, the difference in the finite size behavior is most likely due to differences in layer mixing, rather than to magnetic differences between these SG materials. Figure 6.11 shows the data replotted, assuming a fixed value of boundary mixing for each material, as was done in Section 6.1.2.

Table 6.2 Estimated interface mixing for SG/Si multilayers.

SG	$W_{SG} - W_{SG}'$	ML mixing
CuMn	1.6 nm	~ 7
AgMn	1.3 nm	~ 6
AuFe	3.3 nm	~ 10

Notice that the value of W_{SG}' for CuMn/Si is higher than those found for CuMn with any of the metallic interlayers. This result is consistent with the results of the coupling study, which showed a sharp coupling increase through 3 nm of Si, and with the structural analysis in Section

4.4, which suggested a high degree of interfacial mixing.

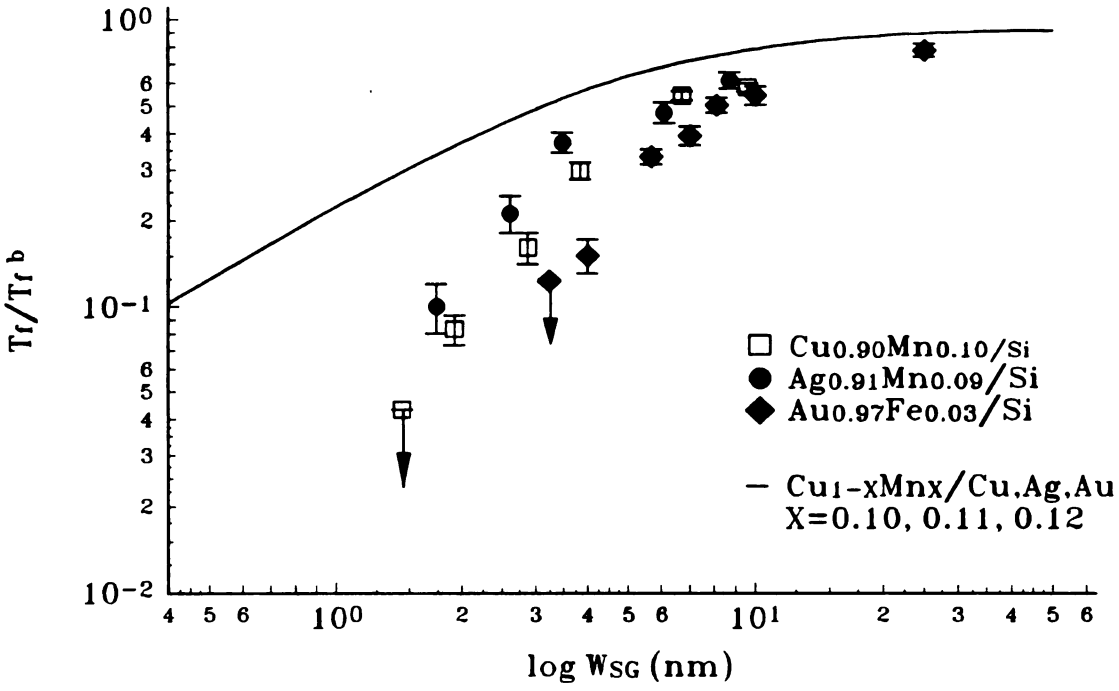

Figure 6.10 Finite size effects of CuMn, AgMn, and AuFe with Si IL.
The solid line represents the averaged CuMn/host IL data as indicated.

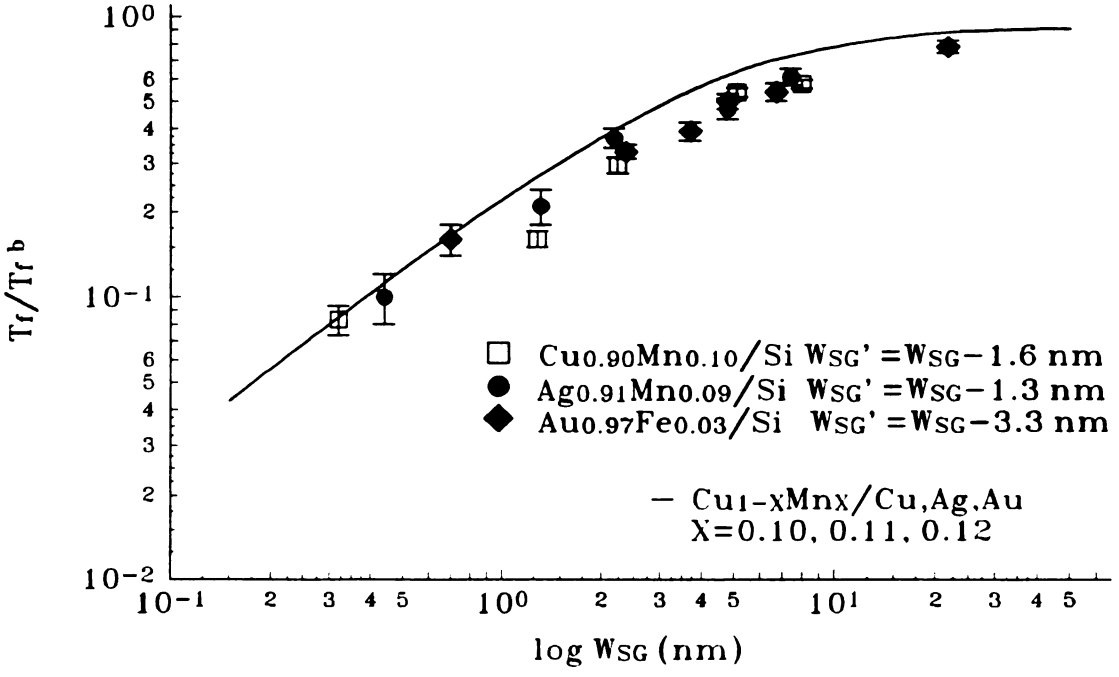

Figure 6.11 Replotted data for Si ILs using effective SG layer thickness (W_{SG}').

6.5 NiMn- Short Range Interaction and Reentrant SG

The NiMn random alloy offers a significantly different system in terms of magnetic interactions. Unlike CuMn, AgMn, and AuFe alloys, where a dilute magnetic element communicates via the RKKY exchange interaction, NiMn contains two magnetic components. All atoms have magnetic neighbors, and the dominating interaction is short range.[49,141] Neutron data indicates competition between ferromagnetic and antiferromagnetic interactions,[50] with ferromagnetic Ni-Ni and Ni-Mn bonds, and antiferromagnetic Mn-Mn bond strengths of the following ratio: 0.25:1.0:4.0.[142] As Mn is added to pure Ni, ferromagnetism persists until enough Mn-Mn interactions occur to disrupt the order. This disruption leads first to a reentrant SG (RSG) regime, where the ferromagnetism surrenders to a mixed SG phase at low temperatures, and then to a regular SG regime, where only paramagnetism and SG exist, as the concentration increases still further (Figure 6.12).

The phase diagram of Figure 6.12 is based on the 1987 work of Abdul-Razzaq and Kouvel.[143] Later Gezalyan and Shul'pekova[144] qualitatively reproduced this picture, but with a slightly higher multicritical concentration (the temperature where T_c and T_{fg} come together) of 25 at.% Mn, and the addition of an antiferromagnetic reentrant region above 30.2 at.% Mn. The Abdul-Razzaq multicritical concentration of 23.9 at. % Mn was supported by Roshko et. al.,[145] who determined a 23.6 at.% Mn sample to be reentrant and a 24 at.% Mn sample to have a single transition to SG. Our study also supports this value, with sputtered samples above 24 at.% Mn behaving as SGs and those below 23 at.% exhibiting reentrant behavior.

The RSG is expected to display a spontaneous ferromagnetic moment, which has been experimentally observed.[146] Although this readily distinguishes the "pure" SG from

the RSG state, some similarities between the two are reported to exist. Magnetic domain structures have been observed to exist in both the RSG and SG phases through hysteresis measurements[146] and neutron depolarization[147]. The neutron data revealed domains of decreasing size as the Mn concentration decreased, with domains of a few hundred nm in the SG phase at 25 at.% Mn and 10-50 μm in the RSG phase at 23 at.% Mn. Evidence of similarity between these two phases also comes from the decay of low field thermoremnant magnetization, where the relaxation isotherms display the same systematics in the RSG and SG phases[148].

The finite size questions then become: a) will the paramagnetic (P) to "pure" SG transition show the same behavior as observed for RKKY-type alloys; b) will the transition in the reentrant regime from the F phase to the RSG phase behave the same as the P-SG transition in the SG regime; and c) will the location of T_c (P to F transition) remain as resistant to change in thickness as observed in regular ferromagnets?

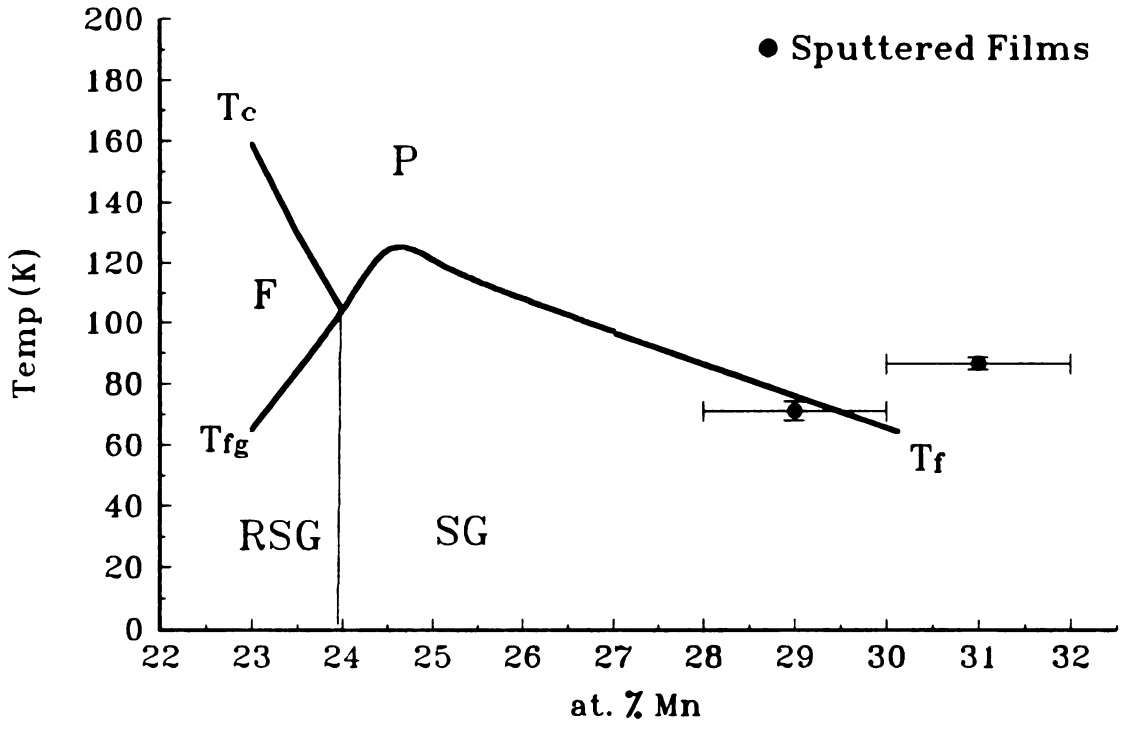

Figure 6.12 NiMn magnetic phase diagram, based on Abdul-Razzaq and Kouvel.

6.5.1 Pure SG Regime

6.5.1.1 T_f^b Values

The data forming the magnetic phase diagram in Figure 6.12 were taken from needle like, bulk samples that were well annealed at a temperature just below the melting point, then quickly quenched in an effort to ensure randomness. The T_f^b values for our sputtered films are also shown in Figure 6.12. The T_f^b value for the samples with 29 at.% Mn agree well with the literature values, but the T_f^b for 31 at.% Mn is higher, indicating T_f^b is rising in this region. We can think of two possibilities for this discrepancy: a) difference in Mn distribution. Since the disorder causing the SG state is dependent on the Mn-Mn nearest neighbor interaction, a different distribution of numbers of nearest neighbors could alter the ordering temperature. For example, if n1 indicates the number of Mn atoms with one Mn nearest neighbor, n2 the number with two nearest neighbors and so on, the annealing-quenching process may produce one distribution of n1,n2,n3,... while the sputtering process may create another distribution of n1',n2',n3',... . Thus our sputtered samples could have a different chemical configuration than the annealed-quenched samples without necessarily containing short or long range order. No ferromagnetism in the magnetic measurements was detected in our NiMn SG sputtered films. b) Difference in atomic spacing. As shown in Chapter 4, sputtered films have a high degree of structural imperfections. For NiMn, this resulted in a 0.6 to 0.8 % smaller lattice parameter than expected for a well annealed alloy of the same concentration[149] in the <111> direction, the growth direction normal to the film surface (in-plane directions were not measured, and might have expanded atomic spacing). It is not unreasonable that small changes in the atomic spacing could affect the ordering temperature of this short range interacting system.

6.5.1.2 NiMn/Cu Multilayers

Cu was chosen as an IL for the NiMn system, since the nominal host, ferromagnetic Ni, was inappropriate for a magnetic study. The previous section showed identical behavior for Cu, Ag, and Au when used as ILs, so Cu was chosen as the cheapest. In hindsight, Ag would have made the x-ray analysis easier, having more contrast in both density and lattice parameter.

The NiMn/Cu system, with its non-host IL, might be expected to display different behavior than a NiMn/host system, such as the faster decreases in T_f seen for the CuMn/non-host systems above. Unlike CuMn, there does not appear to be any published experiment or calculation which indicates the effect of impurities such as Cu on the T_f of NiMn, so it is not known whether mixing Cu into the edges of a NiMn layer would drive T_f up or down. This question might be partly answered by co-depositing some Cu into a NiMn film, and also testing different ILs, such as Al or an insulator.

The coupling behavior was checked only to be sure that the NiMn layers were decoupled by 30 nm of Cu. No change was seen between W_{SG} = 4 nm samples with W_{IL} = 30 and 10 nm, indicating that 30 nm was sufficient for decoupling. Since the interaction between layers must in some way be related to the interaction inside a layer, a detailed coupling study of this material might be a useful comparison to the RKKY systems.

Figure 6.16 shows the normalized T_f data for decoupled NiMn layers. To within experimental error, the finite size behavior of the NiMn/Cu system is not different than the CuMn/host systems. This data should probably be interpreted as a lower bound, since the IL is non-host.

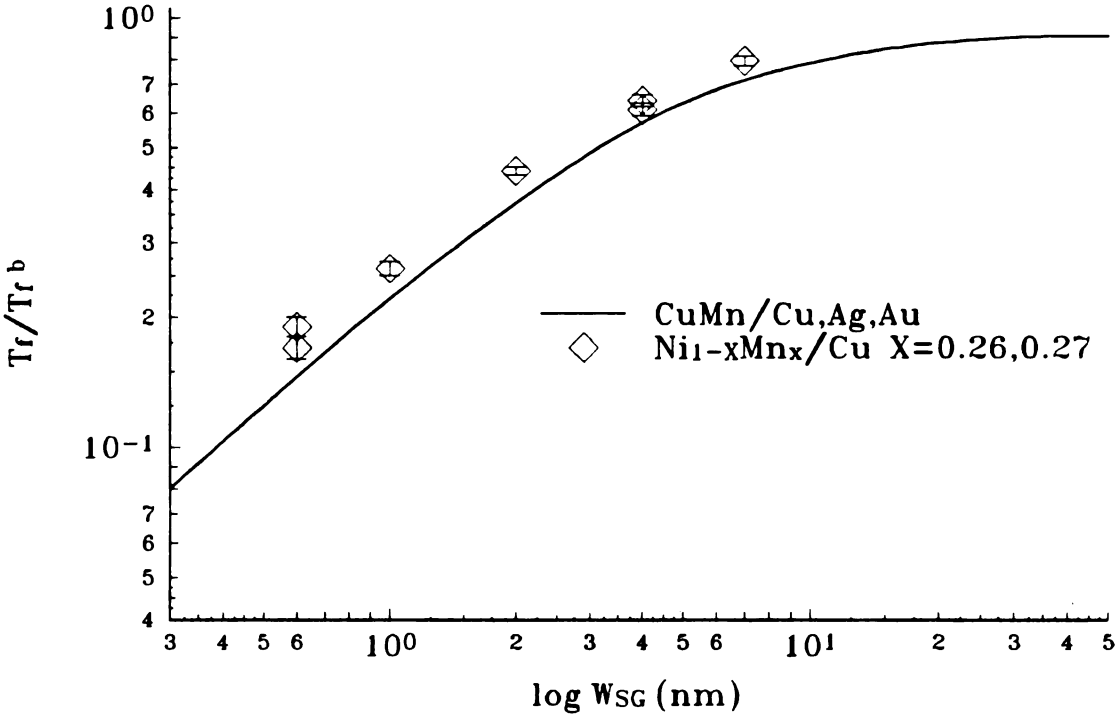

Figure 6.16 Finite size effect behavior of NiMn/Cu SG multilayers.

6.5.2 Reentrant SG Regime

Reentrant behavior was identified through the use of a.c. susceptibility. The characteristic triple peaked curve may be observed with the help of a static biasing field, H_b. Figure 6.17 shows the progression from small H_b = 50 G (very similar to the H_b = 0 scan, not pictured), where the ferromagnetic signal dominates, to a high H_b, where all three peaks are seen. The biasing field in an ac measurement reduces the overall magnitude of the signal, since the signal is dependent on spins following the ac excitation and H_b tends to hold the spins in place. This effect is particularly prominent for a ferromagnetic state, and so the more subtle SG features, hidden by the strong FM signal, are seen through applying H_b. The highest temperature peak, at T3, shifts to higher temperatures as H_b is increased, characteristic of a ferromagnetic peak (an external field aids in the alignment, allowing the FM state to persist to a higher temperature). The two lowest temperature peaks, at T1 and T2, shift to lower temperature as H_b is increased, characteristic of SG phenomenon (an external field disrupts a SG state, which requires spin disorder). A pure SG film should show only one peak in an a.c. χ scan, regardless of the value of H_b. This is the case in Figure 6.15b, where H_b = 400 G is applied to the single peak and no structure is observed.

T1 and T2 indicate two SG transitions, an observation which agrees with the mean field model of Gabay and Toulouse[35]. In this model the reentrant regime has three transitions with decreasing temperature; a) paramagnetic to ferromagnetic (T3), b) ferromagnetic to "mixed" ferro-SG (FSG) state with weak irreversibility (T2) c) crossover to mixed FSG state with strong irreversibility. The FSG state consists of ferromagnetic ordering with spontaneous magnetization, while the transverse component of the spins are frozen into SG ordering. Above T2 the transverse order melts, allowing more conventional ferromagnetism to exist, and above T3 the system is paramagnetic.

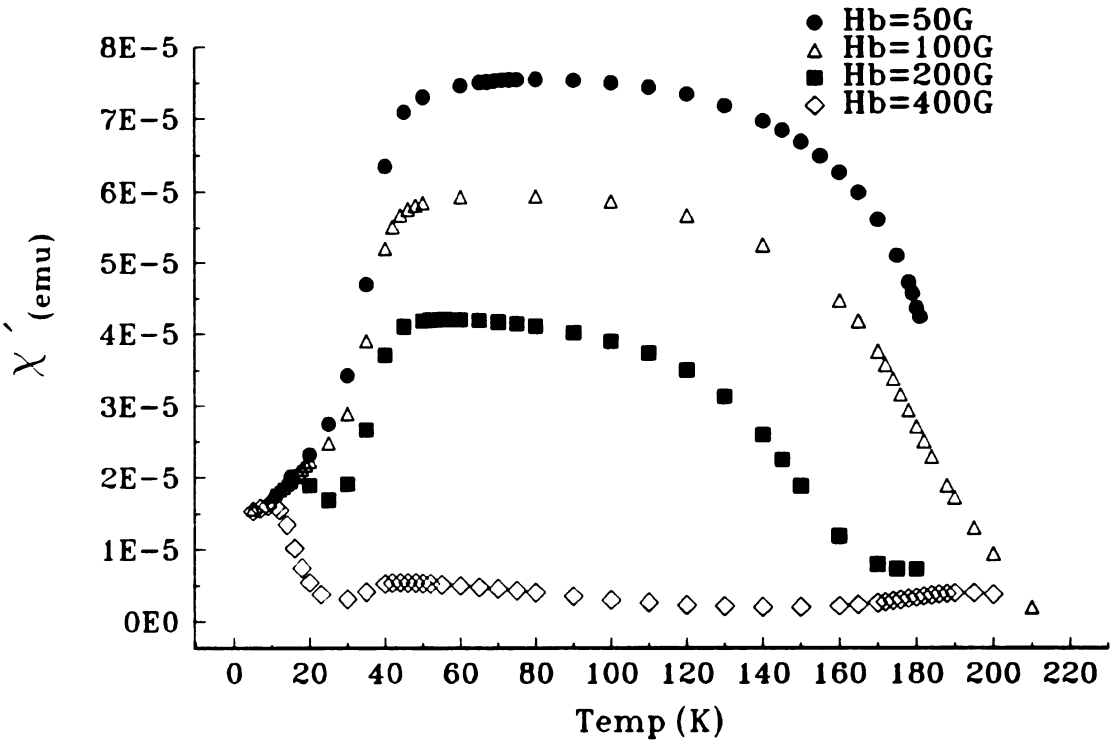

Figure 6.17 Susceptibility of a 500 nm NiMn film the reentrant region (21.5 at.% Mn) with several biasing fields (H_b).

H_b of 200 - 400 G is necessary to observe the triple peaked structure in χ vs. T in our sputtered films, while groups that studied bulk annealed samples have needed only fields of H_b~ 50 G.[141,142,143] Thus, as with the NiMn in the SG region, some significant differences are observed between our sputtered samples and the annealed samples reported in the literature. One possible explanation for the required higher H_b is the presence of stronger ferromagnetism in the sputtered films, thus more external field is required to reduce the FM signal to the desired level. Extrapolating the three peak positions to their values at $H_b = 0$ (as was done by others[143]) proved impossible when the first points were H_b ~ 200 - 400 G and the peaks were entirely extinguished by H_b ~ 1000 G.

Abdul-Razzaq and Kouvel[141] used the low field static magnetization curve to determine values for the phase diagram in Figure 6.12. Tfg was taken from the point of FC-ZFC irreversibility, and T_c was taken from the point of signal drop off. The sputtered NiMn films showed a similar ZFC curve to this measurement, but the FC curve did not rejoin the ZFC curve at the low temperature "corner" (see Figure 6.18). Rather the ZFC curve rejoins suddenly at a higher temperature. We do not know whether this temperature is related to the strong to weak irreversibility crossover, or is merely a result of concentration inhomogeneities in the sample.

The concentration stability was similar in the reentrant NiMn alloys to that found in NiMn SG alloys, but in the reentrant samples the magnetic behavior was inconsistent between samples in the same run, even under the best sputtering temperature control. Thus, continuity could not be guaranteed from one sample to the next, or even from one NiMn layer to the next in the same sample. More work is needed on this problem.

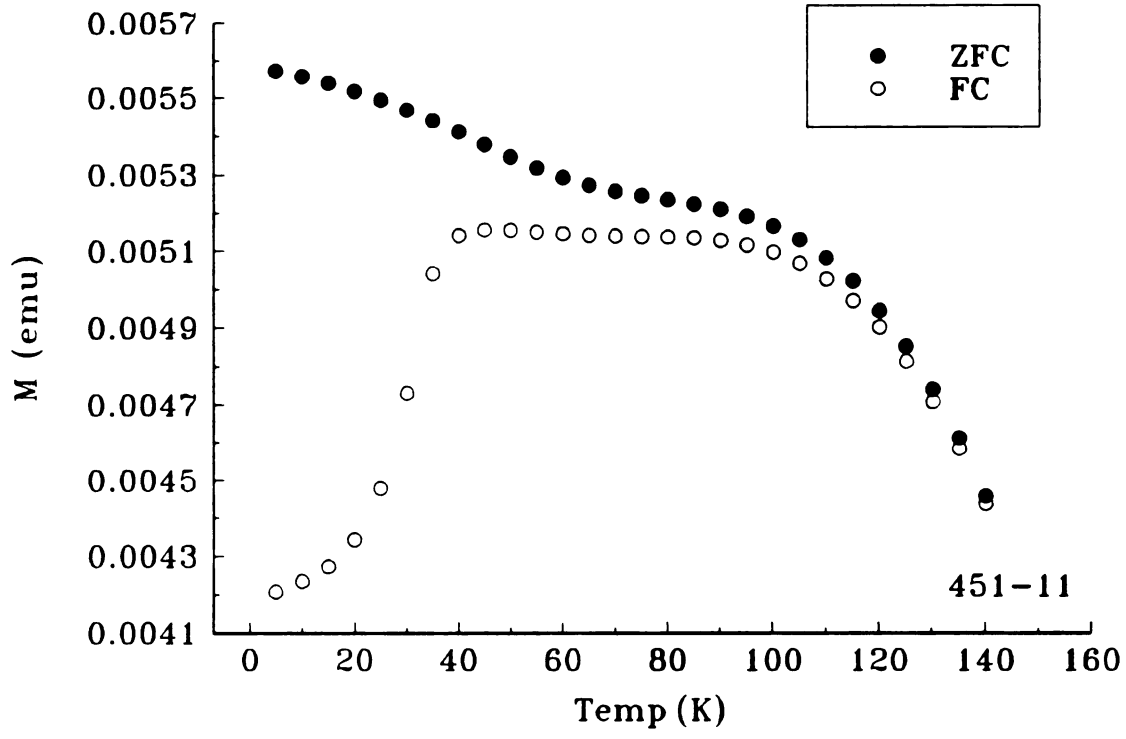

Figure 6.18 Static magnetization for a 300 nm RSG $Ni_{0.77}Mn_{0.23}$ sputtered film.

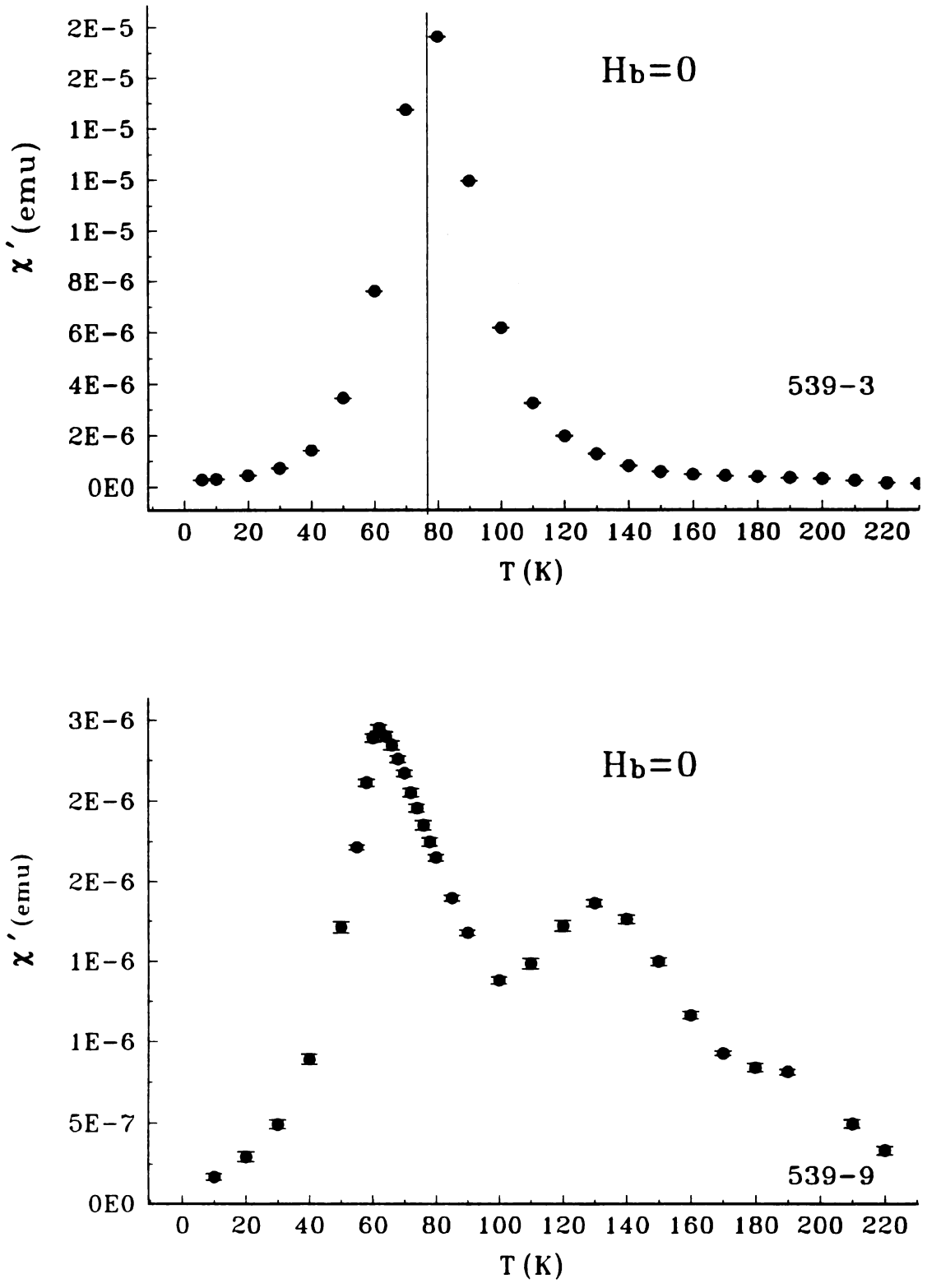

Figure 6.19 Two different χ vs. T (H_b =0) for two RSG NiMn films from the same sputtering run grown under similar well controlled conditions.

One finite size study has been done with sputtered $Ni_{0.88}Mn_{0.22}$/Cu multilayers in the RSG region, by Abdul-Razzaq and Wu[148]. Here T_{fg}/T_{fg}^{b} for thin W_{SG} = 10 nm was 0.88, indicating less of a depression than seen in the CuMn and AgMn systems reviewed in Chapter 1 and the SG systems presented above in this chapter. The triple peak structure was not shown, the static magnetization of the bulk film was not squarish but had a single peak which was defined as Tfg. Reentrant behavior was determined through the thermoremanent magnetization, which persisted until a much higher temperature defined as T_C for the bulk film. The value of T_C for the thin NiMn layer was not reported.

Although the variation in magnetic behavior just described would not allow reliable comparison between our samples, we did make some RSG NiMn/Cu multilayers. Surprisingly, all the multilayers with which showed triple peak structure had T3 much lower than observed in any of the bulk samples (see Figure 6.20). Since T3 is associated with ferromagnetic ordering, it was expected to be the most resistant to changes in layer thickness. This behavior may be an indication that the bulk films contain large ferromagnetic clusters that are unable to form when the multilayer is grown.

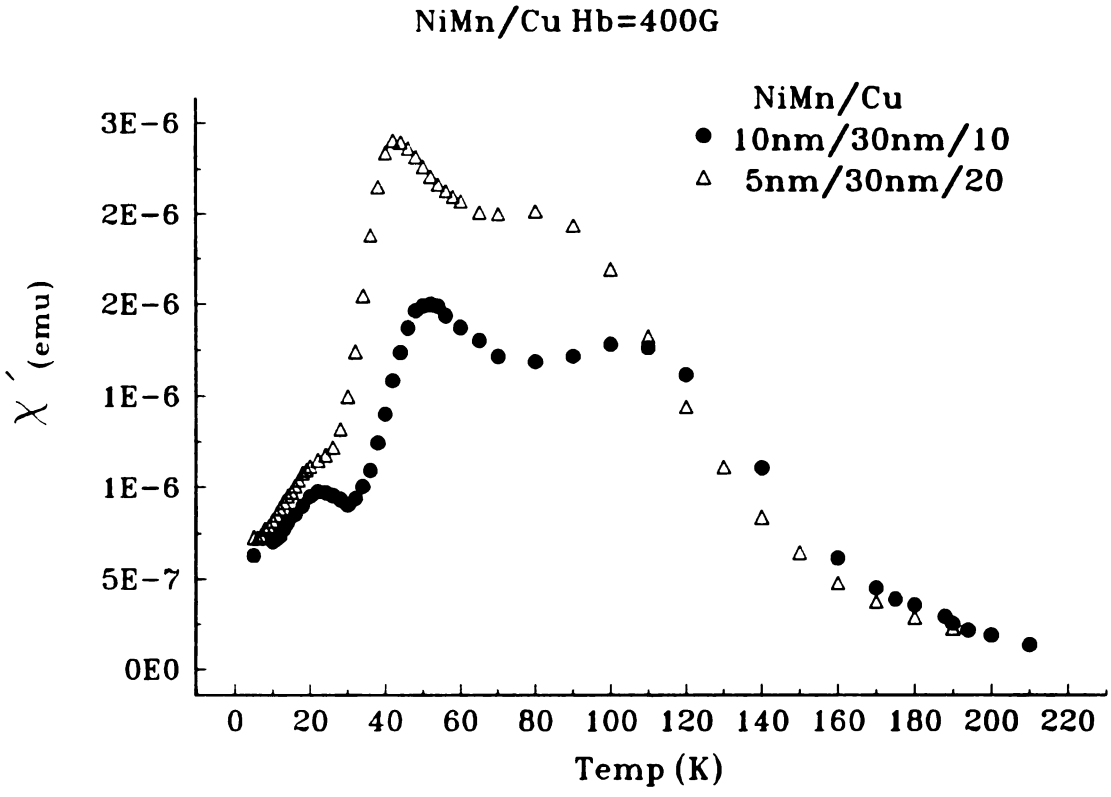

Figure 6.20 χ vs. T with H_b = 400G for RSG NiMn/Cu with 10/30 nm and 5/30 nm.

CHAPTER 7

CONCLUSIONS

7.1 Structure of Multilayers

Using UHV sputtering we have produced a wide variety of multilayers. Five SG alloys and one non-SG alloy were sputtered from home-made targets to produce samples containing $Cu_{1-X}Mn_X$ where X=0.10, 0.11, 0.12, $Ag_{0.91}Mn_{0.09}$, $Au_{0.97}Fe_{0.03}$, $Ni_{1-X}Mn_X$ where X=0.29 and 0.31, $CuMn_{0.04}Au_{0.01}$, and $Cu_{1-X}Ge_X$ where X=0.02 and 0.10. The SGs were layered with the following metals: a) CuMn: Cu, Ag, Au, CuMnAu, CuGe, Al, Mo, Nb, and V; b) AgMn: Cu and Ag; c) AuFe: Au and Ag; d) NiMn: Cu. In addition, CuMn, AgMn, and AuFe were each layered with amorphous Si.

X-ray diffraction analysis was able to confirm layering for all samples. Layering in the SG/Si systems was also confirmed through TEM imaging of cross sections. The layer thicknesses were determined through x-ray diffraction peak analysis and mechanical thickness determination to be ± 5% of the nominal values in almost every case. Crystallites in the metal layers are found to be highly textured, with the <111> plane lying parallel to the sample surface for FCC materials and the <110> plane preferred in the BCC materials. The perpendicular coherence lengths were on the order of ~ hundreds of nms for bulk films of each material. The mixing at the layer interfaces was argued from

magnetic data to be ~ few ML for the SG/metal systems, and 5 to 15 ML in the SG/Si systems.

The Si layer was determined to be amorphous for $W_{SG} \geq 1$ nm through the lack of satellites in large angle x-ray diffraction. Such satellites are seen in CuMn/Si when W_{Si} = 0.5 nm, either because 0.5 nm is the width of a Cu-silicide layer, or 0.5 nm is too thin to create enough of the continuous roughness that is responsible for the satellite destruction. Electron diffraction data for each SG/Si system showed decreasing crystallinity in the SG layer in 3 nm/7 nm samples for AgMn, CuMn, and AuFe respectively.

7.2 Finite Size Effects

To observe finite size effects, SG layers were decoupled by 30 nm of the above metals or 7 nm of Si. T_f was determined through the peak in the low field static ZFC magnetization curve for all samples. The thinnest of the samples, CuMn layers with W_{SG} ~ 1 ML interlayered with Cu or Ag, showed the characteristic FC and ZFC magnetization signature indicating non-zero T_f.

For CuMn/IL where IL = Cu, Ag, or Au, the decreases in T_f with decreasing W_{SG} > 2 nm agreed with the results of Kenning et. al. discussed in Chapter 1. In this W_{SG} range the data fit the generalized scaling law

$$\frac{T_f - T_f^{\,b}}{T_f^{\,b}} \sim W_{SG}^{\,-1/\nu}$$

with $\nu = 1.6$. The generalized scaling expression, however, is incapable of describing data below W_{SG} = 2 nm. The data in the extended range of $0.21 < W_{SG} < 2$ nm show power law behavior, and were fit to the Fisher-Huse Droplet Excitation model for thin W_{SG}:

$$\frac{T_f}{T_f^{\,b}} \sim W^a \quad \text{where} \quad a = \frac{\psi_3 + \psi_2 \nu_2 \theta_3}{1 + \nu_2 \psi_2}.$$

The value obtained for the exponent is $a = 0.8 \pm 0.1$, which is outside the literature estimate of $0.3 < a < 0.65$, but below the rigorous bound of 2.

AgMn was tested as another SG similar to CuMn to determine if its finite size behavior was the same for $W_{SG} < 2$ nm. Within the experimental uncertainty, the finite size effect behavior for AgMn/Cu and AgMn/Ag systems was not different from that observed for CuMn.

Two high anisotropy SGs were studied, inspired by theoretical results indicating that the degree of anisotropy might affect the lower critical dimension d_l (Chapter 1). $CuMn_{0.04}Au_{00.01}$ and AuFe with Ag and Au ILs both show behavior indistinguishable from the equivalent CuMn systems. This suggests that anisotropy does not play a major role in depression of the quasi-static T_f due to finite size effects.

The type of interaction is also theoretically predicted to change d_l (Chapter 1), and so NiMn was chosen as one SG with considerably different interactions than the other SGs studied. The NiMn/Cu system also did not show a significant difference from CuMn behavior, although this data might represent only a lower bound, because the IL used is so different from the SG.

The finite size behavior of CuMn/IL where IL is not a noble metal, was also examined. ILs = Al, Mo, and V (and Si) all induce faster decreases in T_f than that found for the noble metal ILs. This behavior could be attributed largely to mixing at the interfaces.

CuMn, AgMn, and AuFe were each layered with Si, and some differences resulted between the three curves, with AgMn/Si depressed the least and AuFe the most. This

behavior is also explained as an interface mixing effect, using the structural results concerning the crystallinity from x-ray and TEM studies.

7.3 Coupling

The T_f of CuMn with a fixed W_{SG} = 4 nm was studied as a function of decreasing W_{IL}. The same unusually long range coupling (out to W_{IL} ~ 20-30 nm) previously seen for Cu and Ag ILs (Chapter 1) was found for Au and CuGe ILs. Since Au is a strong spin-orbit scatterer, and CuGe has high resistivity, it is concluded that these two effects do not affect the coupling length. All other materials tested- Al, Mo, V, Nb, and Si gave much shorter coupling lengths of ~ 2-5 nm, indicating that the long coupling length is dictated by the electronic structure of the IL.

APPENDIX

Appendix A1

T_f VALUES

All T_f values in this appendix carry an error of ± 0.5 K unless otherwise specified.

Table A1.1 Finite size effect data for CuMn/X and AgMn/X X = Cu, Ag, Au

a. $Cu_{0.88}Mn_{0.12}$/Cu, where W_{II} is fixed at 30 nm. T_f^b = 58.5 from shavings

W_{II} (nm)	T_f	T_f/T_f^b
0.6	8.6	0.15 ± 0.01
1.0	13.1	0.22 ± 0.01
2.0	21.4	0.37 ± 0.01
4.0	34.0	0.58 ± 0.01

b. $Cu_{0.89}Mn_{0.11}$/Cu, where W_{II} is fixed at 30 nm. T_f^b = 49.5 from shavings

W_{SG} (nm)	T_f (K)	T_f/T_f^b
0.21	2.9 ± 0.3	0.059 ± 0.006
0.21	2.6 ± 0.3	0.053 ± 0.006
0.42	4.7	0.095 ± .01
0.42	4.6 ± 0.3	0.093 ± .006
0.42	4.5	0.091 ± .01
0.63	6.4	0.13 ± 0.01
0.63	6.8	0.14 ± 0.01
0.84	8.7	0.18 ± 0.01
1.0	9.3	0.19 ± 0.01
1.0	9.50	0.19 ± 0.01
2.0	18.1	0.37 ± 0.01
2.0	16.7	0.34 ± 0.01
4.0	25.9	0.52 ± 0.01
10.0	36.8	0.74 ± 0.02
0.21/60	2.4 ± 0.3	0.055 ± 0.006

c. $Cu_{0.89}Mn_{0.11}$/Ag, where W_{II} is fixed at 30 nm. T_f^b = 49.5 from shavings

W_{II} (nm)	T_f (K)	T_f/T_f^b
0.21	2.9 ± 0.3	0.059 ± 0.006
0.42	5.1	0.10 ± 0.01
0.63	7.2	0.14 ± 0.01
2.0	16.8	0.34 ± 0.01

d. $Cu_{0.90}Mn_{0.10}$/Au, where W_{II} is fixed at 30 nm. T_f^b = 47.0 from shavings

W_{SG} (nm)	T_f (K)	T_f/T_f^b
0.42	3.5 ± 0.3	0.074 ± 0.007
0.63	6.5 ± 0.3	0.14 ± 0.01
1.0	10.3	0.22 ± 0.01
1.5	14.1	0.30 ± 0.01
2.0	17.8 ± 0.4	0.38 ± 0.01
4.0	24.3 ± 1	0.52 ± 0.02
4.0	27.7	0.59 ± 0.02

e. $Ag_{0.91}Mn_{0.09}$/Ag, where W_{II} is fixed at 30 nm. T_f^b = 24.8

W_{SG} (nm)	T_f (K)	T_f/T_f^b
0.24	< 2	< 0.08
0.42	< 2	< 0.08
0.47	< 2	< 0.08
0.71	2.9 ± 0.3	0.12 ± 0.01
0.94	3.5 ± 0.3	0.14 ± 0.01
2.0	7.3	0.29 ± 1.03

f. $Ag_{0.91}Mn_{0.09}$/Cu, where W_{II} is fixed at 30 nm.T_f^b= 24.8

W_{SG} (nm)	T_f (K)	T_f/T_f^b
0.47	~ 2.5	~0.097
0.71	3.4 ± 0.3	0.14 ± 0.01
0.94	4.2 ± 0.3	0.17 ± 0.02
2.0	7.3	0.29 ± 0.03

Table A1.2 Finite size data for CuMn/X, X= Al, Mo, and V

a. $Cu_{0.88}Mn_{0.12}$/Al, W_{II} fixed at 30 nm T_f^b = 58.5 from shavings

W_{SG} (nm)	T_f(K)	T_f/T_f^b
2.0	13.4	0.23 ± 0.01
4.0	28.7 ± 0.3	0.49 ± 0.01
7.0	39.4	0.67 ± 0.01
50.0	56.4	0.96 ± 0.02

$Cu_{0.90}Mn_{0.10}$/Al, where W_{II} is fixed at 30 nm. T_f^b = 47.0 from shavings

W_{II} (nm)	T_f(K)	T_f/T_f^b
1.0	< 2	< 0.043
1.5	4.8 ± 0.3	0.10 ± 0.01
2.0	10.0 ± 0.3	0.21 ± 0.01

b. $Cu_{0.88}Mn_{0.12}$/Mo, where W_{II} is fixed at 30 nm or 8.0 nm T_f^b = 58.5 from shavings

W_{SG} (nm)	T_f (K)	T_f/T_f^b
0.6/8.0	< 2	< 0.034
1.0/8.0	6.5	0.11 ± 0.01
2.0/80	15.8	0.271 ± 0.01
4.0/30	27.7	0.474 ± 0.01
50.0/30	51.0	0.871 ± 0.02

c. $Cu_{0.89}Mn_{0.11}$/V, where W_{II} is fixed at 30 nm. T_f^b = 49.5 from shavings

W_{SG} (nm)	T_f(K)	T_f/T_f^b
1.0	3.3 ± 0.3	0.067 ± 0.006
1.5	7.5	0.15 ± 0.01
2.0	11.9	0.24 ± 0.01
4.0	24.3	0.49 ± 0.02
10.0	33.9	0.69 ± 0.02
30.0	34.7	0.88 ± 0.02

Table A1.3 Finite size effect data for CuMnAu/X and AuFe/X X = Cu,Ag, and Au

a. $Mn_{0.04}Au_{0.01}/Ag$, where W_{II} is fixed at 30 nm. $T_f^b = 23.5 \pm 1$ from run

W_{SG} (nm)	T_f (K)	T_f/T_f^b
1.0	5.7	0.23 ± 0.02
5.0	14.6	0.58 ± 0.04
12.5	20.2 ± 1	0.86 ± 0.05

b. $CuMn_{0.04}Au_{0.01}/Cu$, where W_{II} is fixed at 30 nm. $T_f^b = 25.3 \pm 1$ from run

W_{SG} (nm)	T_f (K)	T_f/T_f^b
4.0	10.2	0.40 ± 0.03
2.0	7.4	0.29 ± 0.03
0.8	3.7 ± 0.3	0.15 ± 0.01

c. $Au_{0.97}Fe_{0.03}/Ag$, where W_{II} is fixed at 30 nm. $T_f^b = 16.1 \pm 0.6$ from run

W_{SG} (nm)	T_f (K)	T_f/T_f^b
1.0	3.0 ± 0.3	0.19 ± 0.02
1.5	4.0	0.25 ± 0.03
2.0	4.7	0.29 ± 0.03
4.0	8.4	0.52 ± 0.04

d. $Au_{0.97}Fe_{0.03}/Ag$, where W_{II} is fixed at 30 nm. $T_f^b = 17.0 \pm 0.6$ from run

W_{SG} (nm)	T_f (K)	T_f/T_f^b
2.0	6.3	0.37 ± 0.03
4.0	9.4	0.55 ± 0.04
7.0	11.3	0.67 ± 0.04
25.0	14.7	0.86 ± 0.04

e. $Au_{0.97}Fe_{0.03}/Au$, where W_{II} is fixed at 30 nm. $T_f^b = 17.0 \pm 0.6$ from run

W_{SG} (nm)	T_f (K)	T_f/T_f^b
4.0	8.5	0.50 ± 0.03
25.0	14.2	0.84 ± 0.04

Table A1.4 Finite size effect data for NiMn/Cu

a. $Ni_{0.71}Mn_{0.29}/Cu$, where W_{IL} is fixed at 30 nm. $T_f^b = 71 \pm 3$ from run

W_{SG} (nm)	T_f (K)	T_f/T_f^b
0.6	12.4	0.17 ± 0.01
1.0	(19) ac	0.26 ± 0.01
2.0	31.4	0.44 ± 0.0
4.0	43.4	0.61 ± 0.02
7.0	56.3	0.79 ± 0.02

b. $Ni_{0.70}Mn_{0.30}/Cu$, where W_{IL} is fixed at 30 nm. $T_f^b = 86.4 \pm 2$ from run

W_{SG} (nm)	T_f (K)	T_f/T_f^b
0.6	16.1	0.19 ± 0.01
1.0	21.8	0.25 ± 0.01
2.0	37.9	0.44 ± 0.01
4.0	55.0	0.64 ±0.02
7.0	68.0	0.79 ± 0.02

Table A1.5 Coupling data for CuMn/X X = Au, CuGe

a. $Cu_{0.90}Mn_{0.10}/Au$, where W_{SG} is fixed at 4 nm. $T_f^b = 47.0$ from shavings

W_{IL} (nm)	T_f (K)	T_f/T_f^b
1.0	40.3 ± 1	0.86 ± 0.03
2.0	33.5	0.71 ± 0.02
3.0	32.3 ± 0.3	0.69 ± 0.02
4.0	31.3	0.67 ± 0.02
7.0	28.7	0.61 ± 0.02
10.0	28.9 ± 0.3	0.62 ± 0.02
30.0	27.7	0.59 ± 0.02
30.0	24.3 ± 1	0.52 ± 0.02

b. $Cu_{0.90}Mn_{0.10}/Cu_{0.98}Ge_{0.02}$, where W_{SG} is fixed at 4 nm. $T_f^b = 47.0$ from shavings

W_{IL} (nm)	T_f (K)	T_f/T_f^b
3.0	33.0	0.70 ± 0.02
5.0	29.5	0.63 ± 0.01
7.0	28.7	0.61 ± 0.01
10.0	25.1	0.53 ± 0.01
30.0	22.5	0.48 ± 0.01

c. $Cu_{0.90}Mn_{0.10}/Cu_{0.90}Ge_{0.10}$, where W_{SG} is fixed at 4 nm. $T_f^b = 47.0$ from shavings

W_{IL} (nm)	T_f (K)	T_f/T_f^b
1.0	37.2	0.79 ± 0.02
3.0	29.6	0.63 ± 0.01
7.0	24.6	0.52 ± 0.01
5.0	26.8	0.57 ± 0.01
10.0	23.6	0.50 ± 0.01
30.0	22.9	0.49 ± 0.01

Table A1.6 Coupling data for CuMn/X X=Al, Mo, V, and Si

a. $Cu_{0.88}Mn_{0.12}/Al$, where W_{SG} is fixed at 4 nm. $T_f^b = 58.5$ from shavings

W_{IL} (nm)	T_f	T_f/T_f^b
0.5	49.2	0.84 ± 0.02
1.0	44.4	0.76 ± 0.02
1.5	38.7	0.66 ± 0.01
2.0	32.2	0.55 ± 0.01
3.0	32.8	0.56 ± 0.01
5.0	31.7	0.54 ± 0.01
10.0	29.5	0.50 ± 0.01
30.0	28.7 ± 0.3	0.49 ± 0.01

b. $Cu_{0.88}Mn_{0.12}$/Mo, where W_{SG} is fixed at 4 nm. T_f^b = 58.5 from shavings

W_{IL} (nm)	T_f (K)	T_f/T_f^b
0.5	46.4	0.79 ± 0.02
1.5	33.7	0.58 ± 0.01
2.0	30.4	0.52 ± 0.01
4.0	36.6	0.63 ± 0.01
5.0	27.8	0.48 ± 0.01
10.0	27.3	0.47 ± 0.01
30.0	27.7	0.47 ± 0.01

c. $Cu_{0.89}Mn_{0.11}$/V, where W_{SG} is fixed at 4 nm. T_f^b = 49.5 from shavings

W_{IL} (nm)	T_f (K)	T_f/T_f^b
1.0	27.6	0.56 ± 0.01
2.0	26.5	0.54 ± 0.01
4.0	23.6	0.48 ± 0.01
7.0	23.4	0.47 ± 0.01
10.0	24.4	0.49 ± 0.01
30.0	24.3	0.49 ± 0.01

d. $Cu_{0.90}Mn_{0.10}$/Si, where W_{SG} is fixed at 7 nm. T_f^b = 47.0 from shavings

W_{IL} (nm)	T_f (K)	T_f/T_f^b
0.5	42.5	0.90 ± 0.02
1.0	37.6 ± 0.3	0.80 ± 0.02
1.5	34.5	0.73 ± 0.02
2.0	28.3	0.60 ± 0.01
3.0	24.8	0.53 ± 0.01
4.0	24.8 ± 0.3	0.53 ± 0.01
4.0	24.4	0.52 ± 0.01
7.0	25.3 ± 0.3	0.54 ± 0.01
10.0	25.5 ± 0.6	0.54 ± 0.01
10.0	24.7	0.53 ± 0.01

Table A1.7 Coupling data for AuFe/Ag

a. $Au_{0.97}Fe_{0.03}$/Ag, where W_{SG} is fixed at 4 nm. $T_f^b = 15.6 \pm 0.5$ from run

W_{IL} (nm)	T_f(K)	T_f/T_f^b
1.0	12.7	0.81 ± 0.04
2.0	11.5	0.74 ± 0.04
4.0	10.4	0.67 ± 0.04
10.0	8.7 ± 0.3	0.56 ± 0.03
60.0	7.2 o	0.46 ± 0.04

Table A1.8 Finite size effect data for X/Si X= CuMn, AgMn, AuFe

a. CuMn(10)/Si, where W_{IL} is fixed at 7 nm. $T_f^b =$ from shavings

W_{SG} (nm)	T_f(K)	T_f/T_f^b
1.5	< 2	< 0.04
2.0	3.9	0.08 ± 0.01
3.0	7.7 ± 0.3	0.16 ± 0.01
4.0	13.8	0.29 ± 0.02
7.0	25.3 ± 0.3	0.54 ± 0.02
10.0	27.0	0.57 ± 0.02

b. $Cu_{0.85}Mn_{0.15}$/Si, where W_{IL} is fixed at 4 nm. $T_f^b = 65.4 \pm 0.5$ from run

W_{SG} (nm)	T_f(K)	T_f/T_f^b
3.0	14.2	0.217
7.0	37.4 ± 1	0.571

c. $Ag_{0.91}Mn_{0.09}$/Si, where W_{IL} is fixed at 7 nm. $T_f^b = 25 \pm 2$ from run

W_{SG} (nm)	T_f(K)	T_f/T_f^b
2.0	2.4 ± 0.4	0.10 ± 0.02
3.0	5.3 ± 0.3	0.21 ± 0.03
4.0	9.2 ± 0.4	0.37 ± 0.03
7.0	11.8	0.47 ± 0.04
10.0	15.4	0.61

d. $Ag_{0.93}Mn_{0.09}$/Si, where W_{II} is fixed at 7 nm. $T_f^b = 22.7 \pm 0.5$ from run

W_{SG} (nm)	T_f(K)	T_f/T_f^b
7.0	14.4	0.634
3.0	6.7 ± 0.3	0.30

e. $Au_{0.97}Fe_{0.03}$/Si, where W_{II} is fixed at 7 nm. $T_f^b = 16.2, \pm 0.5, 16.1 \pm 0.6$ from run

W_{SG} (nm)	T_f(K)	T_f/T_f^b
4.0	< 2	< 0.123
4.0	2.5 ± 0.03	0.16 ± 0.02
7.0	6.3	0.39 ± 0.03
7.0	5.4 ± 0.03	0.33 ± 0.02
10.0	8.1	0.50 ± 0.03
10.0	8.8	0.55 ± 0.04
25.0	12.5	0.78 ± 0.04

f. $Au_{0.97}Fe_{0.03}$/Si, where W_{II} is fixed at 7 nm. $T_f^b = 15.6 \pm 0.2$ from run

W_{SG} (nm)	T_f(K)	T_f/T_f^b
5.0	3.9 ± 0.3	0.25 ± 0.02
15.0	10.7	0.69 ± 0.03

Table A1.9 T_fs of NiMn films grown under stringent temperature control.

sample	T_f (K)
525-3	66 ± 1
525-5	70 ± 1
525-7	74 ± 1
525-14	73 ± 1

sample	T_f (K)
526-3	84 ± 1
525-5	87 ± 1
525-10	88 ± 1
525-14	87 ± 1

LIST OF REFERENCES

REFERENCES

[1]V. Cannella, J.A. Mydosh, and J.I. Budnick, J. Appl. Phys. **42,** 1689 (1971); V. Cannella and J.A. Mydosh, Phys. Rev. **B6,** 4220 (1972).

[2]J.L. Tholence and R. Tournier, J. Phys. (Paris) **35,** C4-229 (1974); H. Bouchiat and P. Monod, J. Mag. Mag. Mat. **30,** 175 (1983).

[3]K. Binder and A.P. Young, Rev. Mod. Phys. **58,** 801 (1986).

[4]P. Monod, J.J. Prejean, and B. Tissier, J. Appl. Phys. **50,** 7324 (1979).

[5]J.J. Prejean, M.J. Joliere, and P. Monod, J. Phys. (Paris) **41,** 427 (1980).

[6]L.E. Wenger and P.H. Keesom, Phys. Rev. **B11,** 3497 (1975).

[7]C.A.M. Mulder,A.J. van Duyneveldt, and J.A. Mydosh, Phys. Rev. **B23,** 1384 (1981).

[8]D. Sherrington and S. Kirkpatrik, Phys. Rev. Lett. **35,** 1792 (1975).

[9]G. Parisi, Phys. Rev. Lett. **43,** 1754 (1979); ibid, J. Phys. **A13,** L115,1101, and 1887 (1980)

[10]P. Monod and H. Bouchiat, J. Physique Lett. **43,** L45 (1982); R.Omari, J.J. Prejean, and J. Soulitie, J. Physique **44,** 1069 (1986).

[11] L.P. Levy and A.T. Ogielski, Phys. Rev. Lett. **57,** 3288 (1986).

[12]S. Kirkpatrick, Lecture Notes in Physics, Vol. **149,** 280 (1981) Springer, Berlin.

[13]S. Kirkpatrick, C.D. Gelatt, and M.P. Vecci, Science **220,** 671 (1983); S. Kirkpatrick, J. Stat. Phys. **34,** 975 (1984).

[14]J.J. Hopfield, Proc. Natl. Acad. Sci. U.S.A. **79,** 2554 (1982); Ibid, **81,** 3088 (1984); I Guyon and G. Dreyfus, J. Phys. Lett. **46,** L359 (1985).

[15]A. Arrot, J. Appl. Phys. **36,** 1093 (1965).

[16]J.W. Cable, S.A. Werner, G.P. Felcher, and N. Wakabayashi, Phys. Rev. **B29,**1268 (1984).

[17]J.L. Tholence and R. Tournier, J. Phys. (Paris) **35,** C4-229 (1974). H. Bouchiat and P. Monod, JMMM **30,** 175 (1983).

[18]A.P. Malozemoff and Y. Imrg, Phys. Rev. **B24,** 489 (1981).

[19]F. Mezei and A.P. Murani, J. Mag. Mag. Mat. **14,** 211 (1979); F. Mezel, Recent Developments in Condensed Matter Physics, Vol. **1,** Plenum Press, 679 (1981).

[20]G.J. Nieuwenhuys and F.R. Hoekstra, Mag. Resonance Rev. **12,** 137 (1987).

[21]Y.J. Uemura and T. Yamazaki, Physica **109,110B,** 1915 (1982).

[22]R.H. Heffner, M. Leon, and D.E. MacLaughlin, Hyperfine Interactions, **18,** 457 (1984).

[23]P.A. Beck, Prog. Mater. Sci. **23,** 1 (1978)

[24] J.J. Prejean, M.J. joliere, and P. Monod, J. Phys. (Paris) **41,** 427 (1980).

[25]J.S. Kouvel, *Recent Progress in Random Magnets*, ed. D.H. Ryan,World Sci. Press (1992).

[26]L. Sandlund, P. Granberg, L. Lundgren, P. Nordblad, P. Svedlindh, J.A. Cowen and G.G. Kenning, Phys. Rev. **B40,** 869 (1989).
[27]K. Gunnarsson, P. Svedlindh, P. Nordblad, L. Lundgren, H. Aruga, and A. Ito, Phys. Rev. Lett. **61,** 754 (1988); L. Levy, Phys. Rev. **B38,** 4963 (1988).
[28]D. Sherrington, Proc. of Heidolber Col. on Glass Dynamics and Optimization, (1986).
[29]I. Kondor, Science Prog. **71,** 145 (1987).
[30]H. Maletta and W. Felsch, Phys Rev. **B20,** 1245 (1979); H.G. Bohn, W. Zinn, B. Dorner, and A. Kollmar, Phys. REv. **B22,** 5447 (1980).
[31]G.N. Parker and W.M. Saslow, Phys. Rev. **B38,** 11718 (1988).
[32]W. Abdul-Razzaq and J.S. Kouvel, Phys. Rev. **B35,** 1764 (1987).
[33]A.D. Gezalyan nad s. V. Shul'pekova, JETP Lett. **54,** 47 (1991).
[34]M. Gabay and G. Toulouse, Phys. Rev. Lett. **47,** 201 (1981).
[35]M.A. Ruderman and C. Kittel, Phys. Rev. **96,** 99 (1954).
[36]T. Kasuya, Prog. Theoret. Phys. **16,** 45 (1956).
[37]K. Yosida, Phys. Rev. **106,** 893 (1957).
[38]C. Kittel, *Solid State Physics*, Vol 22, ed. F. Seitz, D. Turnbull, an H.Ehrenreich.
[39]J. Souletie and R. Tournier, J. Low Temp. Phys. **1,** 95 (1969).
[40]D.C. Vier and S. Schultz, Phys. Rev. Lett. **54,** 150 (1985).
[41]K. H. Fisher, *Landolt-Börnstien: Numerical Data and Functional Relationships in Science and Technology*, Springer-Verlag Press, **III/15a,** 289 (1982).
[42]L.R. Walker and R.E. Walstedt, Phys. Rev. **B22,** 3816 (1980); U. Larsen, Sol. St. Comm. **22,** 311 (1977); W. Kinzel and K.H. Fisher, J. Phys. **F7,** 2163 (1977).
[43]U. Larsen, Phys. Rev. **B33,** 4803 (1986).
[44]P.G. deGennes, J. Phys. Radium **23,** 28 (1981).
[45]A. Jagannathan, E. Abrahams, and M.J. Stephen, Phys. Rev. **B37,** 436 (1988).
[46]A.Y. Zyuzin and B.Z. Spivak, JETP Lett. **43,** 234 (1986); L.N. Bulaevskii and S.V. Panyukov, JETP Lett. **43,** 240 (1986); U. Larsen, Solid State Commun. **22,** 311 (1977); M. Hitzfeld and P. Ziemann, Phys. Rev. **B32,** 3026 (1985); J.A. Cowen, C.L. Foiles, and J. Shell, J. Mag. Mag. Mater. **31-34,** 1357 (1983).
[47]Q. Zhang and P.M. Levy, Phys. Rev. **B34,** 1884 (1986).
[48]W.J. Carr, Jr., Phys. Rev. **85,** 590 (1952).
[49]J.W. Cable and J.R. Child, Phys. Rev. **B10,** 4607 (1974); T.J. Hicks and O. Moze, J. Phys. **F43,** 2633 (1981).
[50]I.E. Dzyaloshinski, J. Phys. Chem. Sol. **4,** 241 (1958).
[51]T. Moriya, Phys. Rev. Lett. **4,** 51 (1960).
[52]P.M. Levy and A. Fert, Phys. Rev. **B23,** 4667 (1981).
[53]G. Kotliar and H. Somploinsky, Phys. Rev. Lett. **54,** 150 (1985).
[54]S. Schultz, E.M. Gulliksen, D.R. Fredkin, and M. Tovar, Phys. Rev. Lett. **45,** 1508 (1980); K. Okuda and M. Data, J. Phys. Soc. Jpn. **27,** 839 (1969).
[55]P. Monod and Y. Berthier, J. Mag. Mag. Mat. **15-18,** 149 (1980).
[56]A. Fert and P. M. Levy, Phys. Rev. **B44,** 1538 (1980).

[57]H. Alloul, J. Appl. Phys. **50,** 7330 (1979); H. Alloul and F. Hippert, J. Physique Lett. **41,** L-201 (1980).

[58]H. Bouchiat and E. Daryge, J. Physique **43,** 1699 (1982).

[59]Zibold, *Landolt-Börnstien: Numerical Data and Functional Relationships in Science and Technology, New Series,* Springer-Verlag Press, **III/19b,** 111.

[60]M. Hansen, *Constitution of Binary Alloys,* McGraw-Hill Book Co. Inc., (1958).

H. Kunkel, R.M. Roshko, W. Ruan, and G. Williams, Phil. Mag. **B63,** 1213 (1990).

[61]S.A. Werner, Comments Cond. Mat. Phys. **15,** 55 (1990).

[62]J.A. Mydosh JMMM **73,** 247 (1988).

[63] 1960 overhauser, from Fawcett?, A.W. Overhauser, Phys. Rev. **128,** 1437 (1962).

[64]R. Fisch and A.B. Harris, Phys. Rev. Lett. **38,** 785 (1977); R.V. Ditzian and L.P. Kadanoff, Phys. Rev. **B19,** 4631 (1979).

[65]R. Fisch and A.B. Harris, Phys. Rev. Lett. **47,** 520 (1981); R.G. Palmer and F.T. Bantilan Jr., J. Phys. **C18,** 171 (1985).

[66]I. Morgenstern and K. Binder, Phys. Rev. Lett. **43,** 1615 (1979); Ibid, Phys. Rev. **B22,** 288 (1980); Ibid, Z. Phys. **B39,** 227 (1980).

[67]R.N. Bhatt, Phys. Rev. Lett. **54,** 924 (1985); A.T. Ogielski and I. Morgenstern, Phys. Rev. Lett. **54,** 928 (1985); A.T. Ogielski and Nishimori, J. Phys. Soc. (Japan) **56,** 1568 (1987); A.P. Young, Phys. Rev. Lett. **50,** 917 (1983).

[68]W.L. McMillian, Phys Rev. **B31,** 342 (1985); Morris J. Physics **C19,** 1157 (1986); S. Olive, A.P. Young, and D. Sherrington, Phys. Rev. **B34,** 6341 (1986); A.J. Bray and M.A. Moore, J. Phys. **C15,** 3897 (1982); F. Matsubara, T. Iyota, and S. Inawashiro, Phys Rev. Lett. **67,** 1458 (1991).

[69]J.D. Reger and A.P. Young, Phys. Rev. **B37,** 5493 (1988).

[70]A.J. Bray, M.A. Moore, and A.P. Young, Phys Rev. Lett. **56,** 2641 (1986).

[71]see for eg. W. Dürr, M. Tavorell, O. Paul, R. Germar, W. Gudat, D. Pescia, and M. Landolt, Phys. Rev. Lett. **62,** 206 (1989); C.A. Ballentine, R.L. Fink, J. Araya-Pochet, and J.L. Erskine, Phys. Rev. **B41,** 2631 (1990); Yi Li and K. Baberschke, Phys. Rev. Lett. **68,** 1208 (1992); F. Huang, M.T. Kief, G.J. Mankey, and R.F. Williams, Phys. Rev. **B49,** 3962 (1994).

[72]K. Binder and A.P. Young, Rev. Mod. Phys. **58,** 801 (1986).

[73]D.A. Huse and I. Morgenstern, Phys. Rev. **B32,** 3032 (1985).

[74]G.G. Kenning, J.M. Slaugher, and J.A. Cowen, Phys. Rev. Lett. **59,** 2596 (1987).

[75] J.A. Cowen, G.G. Kenning, and J. Bass. J. Appl. Phys. **64,** 5781 (1988);

[76] R. Stubi, J.A. Cowen, d. Leslie-Pelecky, and J. Bass, Physica B **165-166,** 459 (1990).

[77]M.N. Barber, *Phase Transitions and Critical Phenomena,* **8,** ed. C. Domb and J.L. Lebowitz, 145 (1983), Academic Press.

[78]R. Omari, J.J. Prejean, and J. Souletie, J. Physique, **44,** 1069 (1983). The authors actually reported values for critical exponents γ and β, the hyperscaling relation $d\nu = \gamma + 2\beta$ (d=3) was used as in reference [11] to find ν.

[79]G.G. Kenning, J. Bass, W.P. Pratt, Jr., D. Leslie-Pelecky, L. Hoines, W. Leach, M.L. Wilson, R. Stubi, and J.A. Cowen, Phys. Rev. **B42,** 2393 (1990).

[80]G.G. Kenning, thesis (1988).
[81]R. Stubi, J.A. Cowen, L. Hoines, M.L. Wilson, W.A. Fowler, and J. Bass, Phys. Rev. **B44,** 5073 (1991).
[82]A. Gavrin, J.R. Childress, C.L. Chien, B. Martinez, and M.B. Salamon, Phys. Rev. Lett. **64,** 2438 (1990).
[83] D.S. Fisher and D.A. Huse, Phys. Rev. Lett. **56,** 1601 (1986); Ibid, Phys. Rev. **B36,** 8937 (1987)
[84]J. Vranken, C. Van Haesendonck, H. Vloeberghs, and Y. Bruynseraede, Phys. Scr. **T25,** 348 (1989); H Vloeberghs, J. Vranken, C. Van Haesendonck, and Y. Bruynseraede, Euro. Phys. Lett. **12,** 557 (1990).
[85]P.M. Levy and A. Fert, J. Appl. Phys. **52,** 1718 (1981).
[86]D.S. Fisher and D.A. Huse, Phys. Rev. **B36,** 8937 (1987); ibid., **B38,** 386 (1988); ibid, **B38,** 373 (1988).
[87]S. Geschwind, D.A. Huse, and G.E. Devlin, Phys. Rev. **B41,** 2650 (1990).
[88]G. Williams, Can. J. Phys. **65,** 1251 (1987).
[89]J. Mattson, P. Granberg, L. Lundren, P. Nordblad, G. Kenning, and J.A. Cowen, JMMM **104-107,** 1621 (1992).
[90]C. Dekker, A.F.M. Arts, and H.W. de Wijn, J. Appl. Phys. **63,** 4334 (1988); Ibid, Phys. Rev. **B38,** 8985 (1988).
[91]P. Svedlindh, P. Granberg, P. Norblad, L. Lundgren, H.S. Chen, Phys. Rev. **B35,** 268 (1987).
[92]P. Granberg, P. Nordblad, P. Svedlindh, L. Lundgren, R. Stubi, G.G. Kenning, D.L. Leslie-Pelecky, and J.A. Cowen, J. Appl. Phys. **67,** 5252 (1990).
[93]J. Mattsson, P. Granberg, P. Nordblad, L. Lundgren, R. Loloee, R. Stubi, J. Bass, and J.A. Cowen, JMMM **104-107,** 1623 (1992).
[94]J. Mattsson, P. Granberg, P. Nordblad, L. Lundgren, R. Stubi, D.L. Leslie-Pelecky, J. Bass, and J. Cowen, Physica **B165-166,** 461 (1990).
[95]C. Dekker, A.F.M. Arts, H.W. de Wijn, A.J. ban Duyneveldt, and J.A. Mydosh, Phys. Rev. Lett. **61,** 1780 (1988); ibid., Phys. Rev. **B40,** 11243 (1989); J.A. Mysosh, JMMM **90&91,** 318 (1990).
[96]D.D. Awschalom, J.M. Hong, L.L. Chang, and G. Grinstein, Phys. Rev. Lett. **59,** 1733 (1987).
[97]A.G. Schins, A.F.M. Arts, H.W. de Wijn, L. Leylekian, E. Vincent, C. Paulsen and J. Hammann, J. Appl. Phys. **69,** 5237 (1991).
[98]J.A. Cowen, G.G. Kenning, and J.M. Slaughter, J. Appl. Phys. **61,** 4080 (1987).
[99]R. Stubi, D.L. Leslie-Pelecky, and J.A. Cowen, J. Appl. Phys. **67,** 5970 (1990).
[100]R. Stubi, L. Hoines, R. Loloee, I. Kraus, J.A. Cowen, and J. Bass, Europhys. Lett. **19,** 235 (1992). Part of the work in this paper is part of this thesis.
[101]R. Stubi, J. Bass, and J.A. Cowen, J. Appl. Phys. **69,** 5054 (1991).
[102]S.S.P. Parkin, N. More, and K.P. Roche, Phys. Rev. Lett. **64,** 2304 (1990); W.R. Bennet, W. Schwarzacher, and W.F. Egelhoff, Jr., Phys. Rev. Lett. **65,** 3169 (1990); P.

Grünberg, R. Schreiber, Y. Pang, M.B. Brodsky, and J. Sowers, Phys. Rev. Lett. **57,** 2442 (1986).

[103]M.B. Salamon, S. Sinha, J.J. Rhyne, J.E. Cunningham, R.W. Erwin, J. Borchers, and C.P. Flynn, Phys. Rev. Lett. **56,** 259 (1986) and references within.

[104]C.P. Flynn, F. Tsui, M.B. Salamon, R.W. Erwin, an J.J. Rhyne

[105]P. Granberg, J. Mattsson, P. Nordblad, L. Lundgren, R. Stubi, J. Bass, D.L. Leslie-Pelecky, and J.A. Cowen, Phys. Rev. **B44,** 4410 (1991); J. Mattsson, P. Granberg, P. Nordblad, L. Lundgren, R. Stubi, J. Bass, R. Loloee, and J.A. Cowen, JMMM **104-107,** 1619 (1992).

[106]S.F. Edwards and P.W. Anderson, J. Phys. **F6,** 1923 (1976); Ibid, **F5,** 965 (1975).

[107]D. Sherrington and S. Kirkpatrick, Phys. Rev. Lett. **62,** 1972 (1975).

[108]K. Binder and A.P. Young, Rev. Mod. Phys. **58,** 801 (1986).

[109]L.R. Walker and R.E. Walstead, JMMM **31-34,** 1289 (1983).

[110]A. Chakrabarti and C. Dasgupta. Phys. Rev. Lett. **56,** 1404 (1986).

[111]M.E. Fisher, *Advanced Courseon Critical Phenomena,* (1982).

[112]M.E. Fisher, in "Critical Phenomena", Proceedings of the 51st Enrico Fermi Summer School, Varenna, Italy (M.S. Green, ed.), Academic Press, New York.

[113]B. Widom, "Fundamental Problems in Statistical Mechanics", Vol. III, Ed. E.V.G. Cohen, North Holland (1975).

[114]A.E. Ferdinand and M.E. Fisher, Phys. Rev. **185,** 832 (1969).

[115]W. Kinzel and K. Binder, Phys. Rev. **B29,** 1300 (1984); A.P. Young, Phys. Rev. Lett. **50,** 917 (1983).

[116]L. Sandlund, P. Granberg, L. Lundgren, P. Nordblad, P. Svendlindh, J.A. Cowen, and G.G. Kenning, Phys. Rev. **B40,** 869 (1989); P. Granberg, P. Nordblad, P. Svendlindh, L. Lundgren, R. Stubi, G.G. Kenning, D.L. Leslie-Pelecky, J. Bass, and J.A. Cowen, J. Appl. Phys. **67,** (1990).

[117]C. Dekker, A.F.M. Arts, H.W. deWijn, A.J. van Duyneveldt, and J.A. Mydosh, Phys. Rev. Lett. **61,** 1789 (1988); J.A. Mydosh, JMMM **90&91,** 318 (1990).

[118] J.M. Slaughter, W.P. Pratt, Jr. and P.A. Schroeder, Rev. Sci. Instrum. **60,** 127 (1989).
J.M. Slaughter, Ph.D. Thesis

[119] Angstrom Sciences, P.O. Box 18116, Pittsburgh, PA 15236.

[120] Tosoh SMD Inc. 3515 Grove City Rd, Grove City OH 43123-3099 (Formerly Varian)

[121] Demetron Inc. 235 Tenant Ave. Morgan Hill, CA 95037 (old address)

[122] Johnson-Mathey Electronics E. Euclid Ave, Spokane WA 99216 (Formerly Cominco)

[123] Signum Cohn Corp. 121 S. Columbus Ave. Mount Vernon, NY 10553

[124] Silicon Quest International, 2904 Scott Blvd., Santa Clara, CA 95054

[125] Martin Mastovich, Noran Instruments, private communication, (608) 831-6511

[126]See E.W. Nuffield, *X-ray Diffraction Methods,* John Wiley and Sons Inc, NY pg. 148 (1966).

[127]W.B. Pearson, *A Handbook of Lattice Spacing and Structures of Metals and Alloys* Pergamon Press Inc. (1958).

[128]P.F. Miceli, D.A. Neumann, and H. Zabel, Appl. Phys. Lett. **48,** 24 (1986).

[129]A. Segmuller and A.E. Blakeslee, J. Appl. Cryst. **6,** 19 (1973).
[130]D. Neerinck, H. Vanderstaeten, L. Stockman, J.P. Locquet, Y. Bruynseraede, and Ivan K. Schuller, J. Phys.: Cond. Mat. **2,** 4111 (1990).
[131]C.V. Thompson, L.A. Clevenger, r. DeAbillea, E. Ma, and H. Miura, Mat. Res. Soc. Symp. Proc. **187,** 61 (1990).
[132]D.G. Stearns, M.B. Stearns and Y. Cheng, J.H. Stith, and N.M. Ceglio, J. Appl. Phys. **67,** 2415 (1990); R. Pretorius, Vacuum, **41,** 1038 (1990).
[133]L. Slaughter, P.A. Kearney, D.W. Schulze, C.M. Falco, C.R. Hills, E.B. Soloman, and R.N. Watts, Proc. SPIE **73,** 1343 (1990); E. Fullerton, J.E. Mattson, S.R. Lee, C.H. Sowers, Y.Y. Huang, G. Felcher, S.D. Bader, and F.T. Parker, JMMM **117,** L301 (1992).
[134]D.A. Howell, L. Hoines, M.A. Crimp, J. Bass, and J.W. Heckman, Proc. **51st** Annual Meeting of the Microscopy Society of America, eds. G.W. Bailey and C.L. Rieder, 1098 (1993).
[135]J. Liu et. al., Ultramicropscopy, **40,** 352 (1992); P. Donovan et. al., J. Appl. Phys. **69,** 1371 (1991).
[136]see e.g. L. Lundgren, P. Svedlindh, and O. Beckman, JMMM **25**, 33 (1981);
[137]*Handbook of Chemistry and Physics*, ed. R.C. Weast, CRC Press Inc. (1986-7).
[138]J. Bass, *Landolt-Börnstien: Numerical Data and Functional Relationships in Science and Technology*, Springer-Verlag Press, **III/15a,** (1982)
[139]J.S. Kouvel, C.D. Graham, and I.S. Jacobs, J. Phys. Radium **20**, 198 (1952).
[140]G.N. Parker and W.M. Saslow, Phys. Rev. **B38,** 11718 (1988).
[141]W. Abdul-Razzaq and J.S. Kouvel, Phys. Rev. **B35,** 1764 (1987).
[142]A.D. Gezalyan and S.V. Shul'pekova, JETP Lett., **54,** 47 (1991).
[143]R.M. Roshko and W. Ruan, J. Phys. I France, **1,** 1809 (1991). H. Kunkel, R.M. Roshko, W. Ruan, and G. Williams, Phil. Mag. **B63,** 1213 (1991).
[144]J.S. Kouvel, W. Abdul-Razzaq, and Kh. Ziq, Phys. Rev. **B35,** 1768 (1987).
[145] I. Mirebeau, S. Itoh, S. Mitsuda, T. Watanabe, Y. Endoh, M. Hennion, and P. Calmettes, Phys. Rev. **B44,** 5120 (1991).
[146]R.M. Roshko and W. Ruan, J. Phys.: Condensed Matter, **4,** 6451 (1992).
[147]W. Köster and W. Rauscher, Z. Metallik. **39,** 178 (1948).
[148]W. Abdul-Razzaq and M. Wu, J. Appl. Phys. **69,** 5078 (1991).